Generation and Application of Coherent Extreme Ultraviolet Radiation

A thesis submitted for the degree of

Doctor of Philosophy

by

Hoang Vu Le

Centre for Quantum and Optical Science

Faculty of Science, Engineering and Technology

Swinburne University of Technology

Melbourne, Australia

February 2015

Abstract

High harmonic generation featuring ultrashort pulses, short wavelengths and highly coherent radiation in a table-top setup has become one of the most versatile and affordable tools for nano-scale coherent diffractive imaging as well as for studies of atomic dynamics. In this dissertation, the generation and enhancement of a high harmonic source down to the water window region (2.3 - 4.4 nm) is demonstrated, where the source is specifically tailored and developed for imaging applications.

In coherent diffractive imaging, a high resolution image of the sample can only be reconstructed from a diffraction pattern with high dynamic range, high signal-to-noise and sufficient detail at high diffraction angles produced by a bright, stable, highly coherent and narrow bandwidth light source. By controlling and stabilizing the phase-matching condition in a gas cell, an extreme ultra-violet (XUV) source which satisfies these requirements has been generated. Using a harmonic source with wavelengths around 30 nm, a resolution of 45 nm for a micrometer-size transmission sample has been successfully demonstrated. With the use of XUV reflective and focusing mirrors, a single harmonic can be selected to illuminate the sample with a higher photon flux and shorter acquisition time. Furthermore, a phase retrieval algorithm with a phase-curvature correction is developed to take advantage of the higher photon flux when placing the sample near the focus point. The nano-scale images of biological-like absorption samples are also successfully reconstructed with a light source having wavelengths around 30 nm. For a sample with a large transmission area, which quickly leads to saturation of the detector, a beam stop is used to block the low angle region and a stitching algorithm is implemented to create a high dynamic range diffraction

pattern from multiple diffraction data. By implementing the phase retrieval algorithm in a Graphical Processing Unit, the post-processing stage is performed at least 15 times faster than for a conventional system and the reconstruction time is dramatically reduced. This has the potential for live coherent diffractive imaging.

Acknowledgements

Firstly, I wish to thank my principal supervisor, Prof. Lap Van Dao, for his generous supervision, support, encouragement and advice throughout my research. I always value his perspective and recommendations for solving the problem and expanding the possibilities. I deeply thank my associate supervisor, Prof. Peter Hannaford, for his continuous support and assistance, especially his careful and meticulous reviewing scientific papers and this thesis. I also greatly appreciate Dr. Jeff Davis for his kindness and assistance during my study. I wish to acknowledge and thank former CQOS PhD students, Dr. Khuong Dinh and Dr. Chris Hall, who worked closely and kindly supported me in the HHG laboratory. My appreciation also goes to other people in the HHG group, including Dr. Michael Pullen and Naylyn Gaffney, who shared the experiences and made the experiments more exciting. I wish to thank my friends in the Centre, including Gethin Richards, Jonathan Tollerud, Evelyn Cannon, Yuri Mordovin and many more for their friendship and support. I wish to extend my gratitude to Tatiana Tchernova, who sorted out and solved my paper work problems and Mark Kivinen for his skillful work in the mechanical workshop. I also thank people in the Swinburne Nanofabrication Lab, Prof. Saulius Juodkazis and Pierrette Michaux, for fabricating the samples for the CDI experiments. I would like to thank A/Prof. Trevor Smith and Dr. Clare Henderson at The University of Melbourne for their support and discussions regarding the CDI reconstruction algorithm. Lastly, I wish to express my gratefulness to my family, who constantly supported and encouraged me throughout my study, especially my wife, Anh Lam, this thesis would not have been possible without her love, sacrifice and dedication.

Declaration

I, Hoang Vu Le, declare that this thesis entitled:

"Generation and Application of Coherent Extreme Ultraviolet Radiation"

- contains no material which has been accepted for the award to a candidate of any other degree or diploma, except where due reference is made in the text of the examinable outcome;
- to the best of my knowledge contains no material previously published or written by another person except where due reference is made in the text of the examinable outcome; and
- where the work is based on joint research or publications, discloses the relative contributions of the respective workers or authors.

Hoang Vu Le

Centre for Quantum and Optical Science

Faculty of Science, Engineering and Technology

Swinburne University of Technology

Melbourne, Australia

February 10, 2015

Contents

Chapter 1

Introduction

Microscopy has become a crucial tool for studying and understanding the "unseen world", where the objects are beyond the vision of the naked eye. Since the first demonstration of an optical microscope in the 17^{th} century [1][2], the development of microscopy has led to a revolution in biology, physics and nanotechnology.

As the oldest and most popular technique, optical microscopy uses visible light and a lens system to magnify the images of small objects. Due to light diffraction, the resolution is typically limited to $\lambda/2NA$, where λ is the wavelength of the light source and NA is the numerical aperture [3]. With the highest practical NA of 0.95 in air and an average wavelength of white light of 500 nm, the best resolution of optical microscopes is only around 200 nm. This resolution barrier can be overcome by using 'super resolution' microscopy techniques, such as stimulated emission depletion microscopy [4] where a small volume of fluorescent molecules are stimulated by laser beams, and single molecule microscopy [5], where an individual fluorescent molecule can be selected to glow, which yields an image at the nanometre level. However, such optical setups are far more complex and expensive than an ordinary optical microscopy system.

To achieve higher resolution, a shorter wavelength light source and higher resolution lenses are required. Using an electron beam as a source and electromagnetic lenses to focus the beam, the first electron microscope was built by Ernst Ruska in 1931, which was awarded the Nobel Prize in Physics in 1986,

and became one of the most essential tools in nanotechnology [6]. By accelerating the electrons using high voltage, an extremely short wavelength is produced, and hence the resolution can be pushed to the atomic level. The scanning electron microscope (SEM) and the transmission electron microscope (TEM) are two major types of electron microscopes. In an SEM, an electron beam is focused and raster-scanned across the surface of the sample [7]. As the electron penetrates the surface of the sample, electrons and photons that are emitted or scattered are recorded to reveal the details of the sample. Although an SEM is able to image any sample, coating with conducting material (commonly gold) is usually needed to avoid image artifacts due to electrostatic charging and to increase the contrast of the sample's image [8]. On the other hand, TEM obtains an image of the sample by measuring the transmitted electron intensity through the sample. Therefore, TEM can detect defects inside the sample and provide a higher resolution image compared to SEM. Using a 300 kV electron gun TEM, a resolution of ~50 pm (0.5 Å) has been demonstrated [9]. However, sample preparation for TEM is a time consuming process and requires an extensive effort since the sample must be thinner than 50 nm. Furthermore, thin samples can be easily ionized and damaged by the high energy electron beam [10][11].

The development of x-ray microscopes provides an alternative to overcome the limitations of an electron microscope, since x-ray radiation can penetrate thicker samples and the coating process is not required. With a wavelength range from 1 nm to 30 nm, extreme ultraviolet (XUV) and soft x-ray microscopes are useful for imaging biological specimens, nano-crystals and semiconductor materials with nanometre-scale resolution [12]. Especially in the water window region (wavelength: 2.3 – 4.4 nm, energy: 540 - 280 eV), high contrast images of biological samples can be obtained from the different absorption edges of carbon (main element of cells) and oxygen (main element of water) [13]. In this region,

carbon-based objects, such as membrane proteins, absorb the radiation strongly while the water appears transparent and therefore the structure of these samples can be revealed. Studying the details of the structures of proteins and understanding their behaviour are crucial factors in the development of new antibiotics and medication treatments. Compared to optical and electron microscopes, the extreme ultraviolet and soft x-ray microscope has greater potential for biological applications. However, the development of x-ray microscopy still faces two main challenges. Firstly, the optics elements for an x-ray microscopy system are more difficult to produce and less effective since x-ray radiation is strongly absorbed by matter. Therefore, focusing x-ray radiation is harder than focusing electrons and this problem limits the achieved resolution of the sample's image, so that the highest resolution currently achieved by an x-ray microscope is around 10 nm [14]. Secondly, bright XUV and soft x-ray sources for microscopy applications are only available in multi-million-dollar large scale facilities such as synchrotrons and free electron lasers, which provide a capability for only a limited number of research groups [15][16]. Furthermore, the high demand for using these facilities for imaging applications incurs a high cost and requires scientists to maximize access in a tight schedule for their "beam time".

The first problem can be overcome by the development of a new imaging method, coherent diffractive imaging (CDI) or "lensless imaging", in which the optics lens used to reconstruct the sample's image is replaced by a computer-based reconstruction algorithm [17 − 21]. When an object is exposed to light from a coherent source, a diffraction pattern of the object is created and based on diffraction and propagation theory the complex electric field of the light diffraction can be considered as a Fourier transform of the object. The object's image can then be reconstructed by performing an inverse Fourier transform. Because only the intensity of the diffraction pattern is recorded, a Fourier-based

iterative phase retrieval algorithm combined with an over-sampling method is used to recover the phase for reconstruction of the image [22][23]. Conventionally, the sample can be illuminated by a planar wave field (Fraunhofer CDI), but a curved wave field (Fresnel CDI) can also be used, where the source is focussed by a zone-plate [18][24]. Using knowledge of the curvature of the wave field on the sample, a unique solution and convergence of the phase retrieval process is guaranteed; however, the geometrical parameters must be precisely determined. In theory, the resolution of the image reconstructed from its diffraction pattern is only limited by the wavelength of the source and the amount of collected high frequency data. Furthermore, a high degree of spatial and temporal coherence of the source is one of the crucial requirements, and the spectral bandwidth must be very narrow to achieve higher resolution. To obtain narrow bandwidth sources, wavelength-selective mirrors or monochromators are usually required, which reduces the efficiency of the source due to wasted photon flux. Recent modifications to the phase retrieval algorithm have relaxed the coherence requirement, such as multiple wavelength CDI [25] and broadband x-ray source [26], where the diffraction pattern is considered as a combination of the intensity distribution produced by each individual wavelength.

Since their first demonstration in 1987 [27], high harmonic generation (HHG) sources, which are generally produced by focusing a high intensity laser into a nonlinear medium, provide a new solution for XUV and soft x-ray imaging, with their ultra-short pulses, excellent coherence properties and high degree of tunability. High harmonic radiation nowadays can be extended to the soft x-ray region with photon energies > 1 keV using a mid-infrared driving laser [28]. Furthermore, the experimental setup of HHG only requires a compact table-top setup, which makes it an affordable tool for studying nanoscale systems. By controlling the microscopic phase-matching conditions, the generated harmonics

can be confined to a few orders [29], which increases the efficiency of the source for CDI experiments.

The theoretical and experimental work presented in this thesis was performed in the Centre for Quantum and Optical Science (CQOS) at Swinburne University of Technology, as part of the Short Wavelength Laser Source Program of the Australian Research Council Centre of Excellence for Coherent X-Ray Science (CXS). The project includes the development of a HHG system to produce bright, narrow bandwidth XUV radiation around 30 nm and the use of this source for CDI experiments. Chapter 2 presents the history and background of HHG, and the theory and the experimental setup to produce narrow bandwidth XUV radiation in a gas cell. This includes the analysis of various experimental parameters to optimize the phase-matching process and to enhance the quality of the high harmonic source. In addition, the generation of high harmonic radiation in the water window region is demonstrated. In chapter 3, the principles and requirements of CDI are reviewed, including diffraction and sampling theory, experimental considerations, the phase retrieval algorithm and the resolution limit of coherent x-ray imaging. In previous experiments in our laboratory, a resolution of 100 nm for a periodic sample was successfully demonstrated using a 30 nm wavelength source [30]. In chapter 4, a CDI experiment to image a transmission sample with a resolution of 45 nm using high harmonic sources around 30 nm is presented. Using narrow bandwidth reflective and focusing mirrors, a single harmonic is selected and focused into the sample, thus increasing the effective photon flux and reducing the required exposure time. Experiments to characterise the focused high harmonic beam are also presented, including measurements of the beam profile and the frequency spectrum of the source. A novel experimental scheme to measure the source's spectrum is proposed and demonstrated, in which the detailed spectrum is directly obtained from the diffraction pattern of an array

of pinholes. Because of the use of a focusing mirror, the effect of the curvature field on the diffraction pattern and reconstruction process is also investigated. Simulations and experiments suggest the beam diameter should be at least four times larger than the sample size in order to reconstruct the image using a conventional phase retrieval algorithm. In this chapter, a new phase retrieval algorithm with phase correction is also introduced, which takes the curvature of the fields of the focused beam into account if the sample is placed close to the focus point. By applying this new algorithm, the sample can be placed closer to the focus point to take advantage of the higher photon flux without compromising the achieved resolution. Chapter 5 presents a CDI experiment to obtain images of biological-like samples, where the XUV radiation is absorbed by the objects. To capture high resolution images, beam stops are implemented to prevent saturation in the diffraction pattern. However, another challenge is faced by using a beam stop: missing data in the low frequency region. A new technique of combining diffraction patterns to solve the missing data problem and reconstruct the image is discussed and demonstrated. Finally, chapter 6 presents a summary of the thesis, as well as the outlook for the development of higher resolution CDI using table-top high harmonic generation.

Chapter 2

Extreme Ultraviolet Source by High Harmonic Generation

2.1. Introduction to High Harmonic Generation

Since the first high harmonic signal was observed by McPherson et al. in 1987 [27], many theoretical and experimental approaches have been developed with advances in technology pushing the limit of the harmonic wavelength and energy [31]. With the ability to generate wavelengths down to the water window region (2.3 – 4.4 nm) [32][33], and even the 1 nm [34] range, the table-top high harmonic source has proven to be an effective and affordable source to study molecular dynamics [35]–[38] as well as the coherent diffractive imaging application [39][25][40]. Although the principle of high harmonic generation (HHG) is quite simple - one focuses an ultrashort, intense laser pulse (intensity $> 10^{14}$ W/cm^2) into a gas medium to produce the harmonic signal - the low conversion efficiency is the main drawback of this source. The main reason is the phase mismatch between the harmonic signals and the fundamental laser and the absorption of the medium. To enhance the efficiency of the HHG source, a technique called "phase matching" has been developed [41][42][43]. Several experimental approaches have been developed to implement a phase-matching scheme, including a hollow waveguide [42], a self-guide laser [44], a gas jet [45] and a gas cell [46].

In this chapter, the theoretical background of the HHG and phase-matching techniques is presented. Then the experimental setup to generate a bright, stable, coherent and narrow bandwidth XUV source around 30 nm is described.

Furthermore, an experimental scheme to generate high harmonic radiation in the water window region using an infrared driving laser is demonstrated. In addition, the use of high harmonic generation to study atom and molecule dynamics is reported based on the observation of a Cooper minimum with two-colour laser fields.

2.2. Theory of High Harmonic Generation

2.2.1. The three-step model

The high harmonic generation (HHG) process is a phenomenon in which a high electric field created by an intense laser field (typically 1014 – 1015 W/cm2) is comparable to the binding atomic Coulomb field of the atoms used in the generating medium, so that an outer-shell electron can tunnel into the continuum. The process is well described by a semi-classical approach called the "three-step model", where the electrons undergo tunneling ionization, acceleration and recombination processes [47][48].

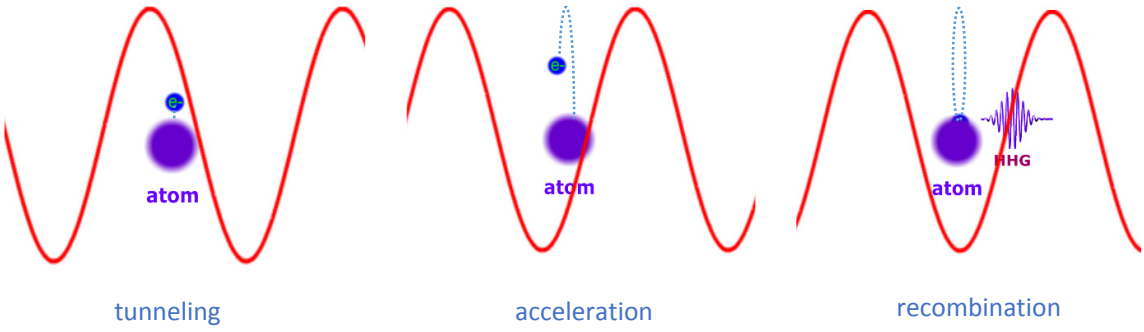

Figure 2.1: The three-step model of high harmonic generation.

In the first step, the electron under the influence of the driving laser's large electric field tunnels out of the parent atom, due to distortion of the Coulomb potential. The rate of the tunneling process (the so-called ionization rate), which can be calculated by the Ammosov, Delone and Krainov (ADK) model [49], is critical for the efficiency of the harmonic generation process. During the second step, the electron is accelerated in the electric field of the laser, and initially moves away from the parent atom and then returns when the electric field changes sign, and eventually re-collides with the parent ion in the final step to release the high harmonic radiation. The kinetic energy which the electron gains during the accelerating phase is known as the ponderomotive energy, which is defined as [50]:

$$U_p = \frac{e^2 E^2}{4\, m_e\, \omega_0^2} \propto I\lambda^2 \qquad (2.1)$$

where e and m_e are the charge and mass of the electron, E is the electric field and ω_0 is the angular frequency of the driving laser. The ponderomotive energy is also proportional to the intensity I and the square of wavelength λ^2 of the driving laser. The maximum energy of the generated high harmonic radiation is given by [50]:

$$\mathcal{E}_{max} = \hbar\omega_o q_{max} = I_p + 3.17\, U_p \qquad (2.2)$$

where $\hbar$ is the reduced Planck's constant, q_{max} is the maximum harmonic order and I_p is the ionization potential of the atom. The maximum harmonic energy is achieved when the atom is ionized at a phase ~0.3 radians (17^0) of the electric field. Additionally, the cutoff energy of the HHG is dependent on the ionization potential of the atom, which varies for different generating media. Table 2.1 shows the ionization potentials of the noble gases and their typical cutoff harmonic orders when using a 800 nm driving laser with a peak intensity 5×10^{14} W/cm^2.

Medium	I_p (eV)	Cutoff order
Xe	12.1	27
Kr	14	41
Ar	15.8	61
Ne	21.6	155
He	24.6	221

Table 2.1: Ionization potential and cutoff harmonic order of the noble gases.

According to equation 2.2, the cutoff energy of the high harmonic generation can also be increased by raising the intensity of the driving laser intensity if plasma effects such as defocusing and dephasing are controlled and not all atoms are ionized. However, too high a laser intensity also leads to a larger contribution of the magnetic force (Lorentz force) on the electrons, preventing them from recombining with their parent ions and hence reducing the efficiency of the HHG process [51][52].

In the three-step model, there are two major electron trajectories that contribute to the high harmonic generation process, the short and long trajectories, according to the time they spend in the continuum. The short trajectory is defined where the electron escapes the atom after 17^0 of the laser cycle and returns before 255^0, whereas for the long trajectory the electron escapes the atom before 17^0 and returns. Figure 2.2 illustrates the difference between the two quantum paths within the driving laser cycle. In the short trajectory (shown by the blue curve), the electrons encounter one laser field zero crossing, and as time increases, the electrons gain more kinetic energy to recombine with the parent ion, and hence emit more photon flux. On the other hand, the electrons that follow the long trajectory (red curve) decrease energy with recombination time. The emitted

energy is shown by the green curve, where the peak energy (cutoff energy) corresponds to the cutoff trajectory (orange curve).

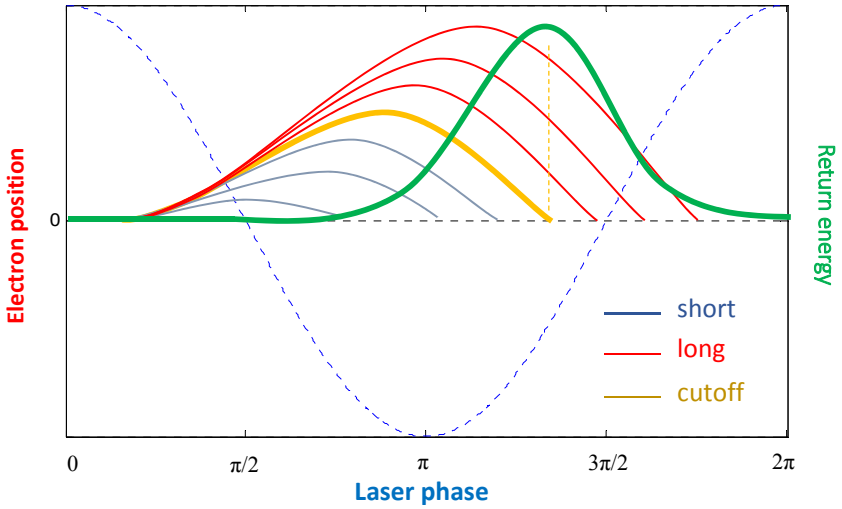

Figure 2.2: Short (blue) and long (red) electron trajectories are shown with the driving laser field (dashed curve). The generated high harmonic energy is shown (green), where the peak (cutoff energy) corresponds to the cutoff trajectory (orange).

The harmonic radiation produced by the short trajectories has a long coherence time, since their phases do not vary much with the laser intensity; furthermore, it is a highly collimated beam and spectrally narrow, which is desirable for the CDI application. On the other hand, the phases of the long trajectories change rapidly with the laser intensity; hence they create strongly angular divergent emission due to the strong curvature of the phase front, and they tend to increase the spectral bandwidth and reduce the coherence time [53][54]. In other words, the short trajectories are less sensitive to the change of the driving laser intensity compared to the long trajectories, and hence this is one of the parameters to optimize the HHG beam in order to produce a bright, collimated and coherent source for CDI experiments.

2.2.2. The high harmonic spectrum

A typical HHG spectrum consists of three regions: perturbative, plateau and cutoff regions. In the low harmonic order regime, also called below-threshold harmonics, perturbation theory can be used to describe the generation of harmonics in which the intensities decrease exponentially for higher orders [55]. In the long plateau regime, in which the harmonic intensities are almost constant, the perturbative theory is no longer valid but the spectrum can be explained by the three-step model, which is generated by both short and long electron trajectories. The cutoff region is mainly dominated by the short trajectories and the maximum frequency of the HHG radiation follows the cutoff rule in equation 2.2.

Since the high harmonic burst is repeated every half cycle of the laser field, a typical harmonic spectrum consists of only odd harmonics, which are separated by $2\omega_0$ [56]. This property can also be explained by the Fourier transform of a periodic signal, where the constructive interference of odd harmonics and the destructive interference of the even harmonics occur.

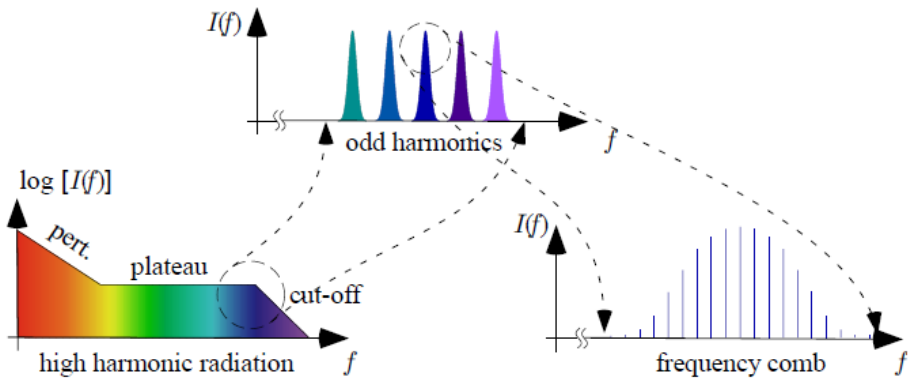

Figure 2.3: Typical HHG frequency spectrum; figure taken from [57].

2.2.3. Phase matching

Phase matching is a critical requirement to generate bright and highly efficient HHG radiation, in which the phase velocity of the driving laser field (v_f) must be ideally matched to the phase velocity of the harmonic (v_q) so that the total intensity of the harmonic radiation builds up coherently. This requirement can be represented as [58]:

$$v_f = \frac{\omega_f}{k_f} = v_q = \frac{\omega_q}{k_q} = \frac{q\,\omega_f}{k_q} \tag{2.3}$$

where ω_f and ω_q are the angular frequencies, k_f and k_q are the magnitudes of the wave vector of the driving laser and the q harmonic. Hence the HHG efficiency is maximum when the phase mismatch (Δk) between the fundamental laser field and the harmonic field is zero, i.e.,

$$\Delta k = q\,k_f - k_q = 0 \tag{2.4}$$

The coherence length, which is the distance over which the harmonic interferences build up constructively, is then defined as [42]:

$$L_{coh} = \frac{\pi}{\Delta k} \tag{2.5}$$

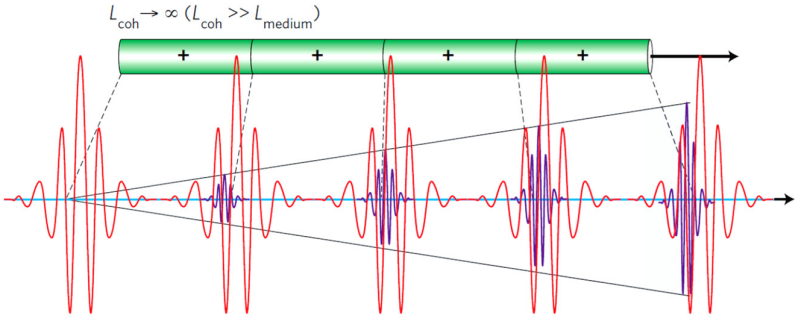

Figure 2.4: The high harmonic signals build up coherently when $\Delta k = 0$, as the amplitude (and quadratic intensity) of the HHG signal increase linearly with the interaction length [59].

In the ideal situation when the coherence length is large ($L_{coh} \rightarrow \infty$), the high harmonic intensity increases quadratically with the interaction length as shown in Figure 2.4. However, in the presence of absorption, the high harmonic intensity will be limited, and is given by [42]:

$$I_q \sim \rho^2 A_q^2 \frac{4L_{abs}^2}{1 + 4\pi^2 \left(\frac{L_{abs}}{L_{coh}}\right)^2} \left[1 + \exp\left(-\frac{L_{med}}{L_{abs}}\right) - 2\cos\left(\frac{\pi L_{med}}{L_{coh}}\right)\exp\left(-\frac{L_{med}}{2L_{abs}}\right)\right] \quad (2.6)$$

where L_{abs}, L_{med} are the absorption length (over which the intensity falls to 1/e, $L_{abs} = 1/(\sigma\rho)$) and medium (interaction) length, ρ is the gas density, σ is the ionization cross section and A_q is the amplitude of the atomic response which is proportional to the laser intensity. The relationship between the coherence length and the absorption length with the high harmonic intensity is shown in Figure 2.5:

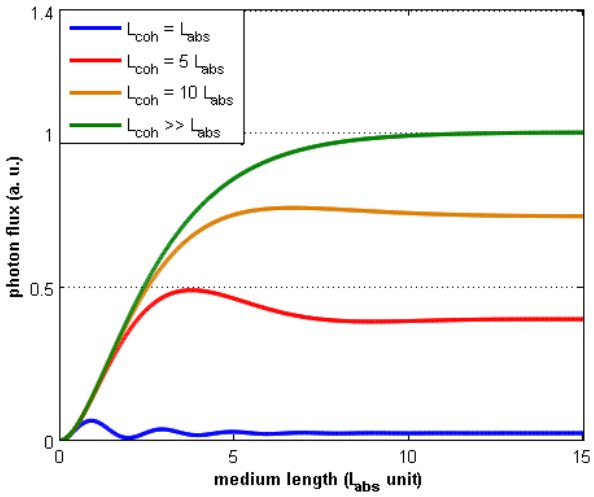

Figure 2.5: High harmonic photon flux in a medium with different coherence lengths compared to the absorption length [42].

As can be seen, in order to maximize the efficiency of the HHG signal, the coherence length and the interaction length must be much longer than the absorption length. If the coherence length is long enough ($L_{coh} \to \infty$), the harmonic intensity will be limited to:

$$I_q \sim L_{abs}^2 \left[1 + \exp\left(-\frac{L_{med}}{L_{abs}}\right) - 2\exp\left(-\frac{L_{med}}{2L_{abs}}\right)\right] \tag{2.7}$$

With a reasonably long interaction length ($L_{med} \gg L_{abs}$), the high harmonic intensity is now simply $I_q \sim L_{abs}^2$, which is proportional to the square of the absorption length. In an ideal case where there is no absorption ($L_{abs} \to \infty$), the high harmonic intensity reduces to:

$$I_q \sim \left[\frac{L_{coh}}{\pi}\sin\left(\frac{\pi L_{med}}{2L_{coh}}\right)\right]^2 \tag{2.8}$$

in which the harmonic intensity oscillates as the signal propagates through the interaction medium, and for which the maximum value is proportional to the

square of the coherence length. In fact, understanding and controlling the phase mismatch is a crucial requirement to increase the coherence length and to optimize the high harmonic flux. The phase mismatch is given by [60][61]:

$$\Delta k = \Delta k_{neutral\ atom\ dispersion} + \Delta k_{plasma\ dispersion} + \Delta k_{geometric} + \Delta k_{dipole\ phase} \quad (2.9)$$

The details of each term are described below:

a) Neutral atom dispersion phase mismatch:

The neutral atom dispersion originates from the difference in the refraction indices of the fundamental and harmonic frequencies, and is given by:

$$\Delta k_{neutral} = \frac{2\pi q}{\lambda} P(1-\eta)\,\Delta_n \quad (2.10)$$

where q is the harmonic number, λ is the fundamental wavelength of the laser, P is the pressure of the gas, η is ionization fraction and $\Delta_n = n(\lambda) - n(\lambda/q)$ is the difference between the refractive indices at the fundamental and harmonic frequencies of the gas at 1 atm. Furthermore, the refractive index consists of a linear and a nonlinear component which is dependent on the laser intensity, i.e., $n = n_0 + n_2 I$. Normally, the refractive index of the gas is larger than one in the range of the fundamental laser's wavelength but smaller than one for the XUV range; hence usually $\Delta k_{neutral} > 0$.

b) Plasma dispersion phase mismatch:

Under the action of the strong electric field of the driving laser, the atoms are quickly ionized, but only a small fraction of the free electrons re-collide with their parent atoms to generate high harmonic radiation. The remaining free electrons miss the atom and cause dispersion and absorption of the high harmonic signal, which oscillates rapidly, and their resonance frequency is given by:

$$\omega_p = \sqrt{\frac{e^2 N_e}{\varepsilon_0 m_e}} \tag{2.11}$$

where N_e is the free electron density, ε_0 is the permittivity constant and m_e is the mass of the electron. This oscillation leads to a change of the refractive index of the plasma, which is given by:

$$n_{plasma} = \sqrt{1 - \left(\frac{\omega_p}{\omega}\right)^2} \tag{2.12}$$

Since the plasma resonance frequency is much smaller than the fundamental frequency, equation 2.12 can be simplified to:

$$n_{plasma} \approx 1 - \frac{1}{2}\left(\frac{\omega_p}{\omega}\right)^2 \tag{2.13}$$

The wave vector of the plasma becomes:

$$k_{plasma}(\omega) = \frac{\left(n_{plasma}(\omega) - 1\right)\omega}{c} = -\frac{\omega_p^2}{2c\omega} \tag{2.14}$$

and hence the plasma phase mismatch is calculated as:

$$\Delta k_{plasma} = qk(\omega) - k(q\omega) = \frac{\omega_p^2(1 - q^2)}{2qc\omega} \tag{2.15}$$

Substituting equation 2.11 and the electron density ($N_e = \eta P N_{atm}$) into equation (2.15), the simplified plasma dispersion phase mismatch is given by:

$$\begin{aligned} \Delta k_{plasma} &= \frac{e^2 N_e}{2\varepsilon_0 m_e c\omega}\frac{(1 - q^2)}{q} \\ &= \eta P N_{atm} r_e \lambda \frac{(1 - q^2)}{q} \end{aligned} \tag{2.16}$$

where $r_e = \frac{e^2}{4\pi\varepsilon_0 m_e c^2}$ is the classical electron radius, η is the ionization fraction, P is the gas pressure and N_{atm} is the gas density at 1 atm. Clearly, the plasma phase

mismatch is negative; hence it is useful to balance this with the neutral atom dispersion, where both terms are dependent on the gas pressure and the ionization fraction. Therefore, there is an upper limit to the ionization fraction, called the critical ionization rate, which allows phase matching to be achieved, and is given by [60][41]:

$$\eta_c = \left(1 + \frac{N_{atm} r_e \lambda^2}{2\pi \Delta n}\right)^{-1} \tag{2.17}$$

The critical ionization rate varies with different gases; typically this value is 5% for Ar, 1% for Ne and 0.5% for He to achieve phase matching [41]. Since the ionization fraction is very sensitive to the laser intensity, this parameter is an important "knob" to optimize the phase-matching process.

c) Geometric phase mismatch:

Since the HHG process requires the laser beam to be focused and confined into a small region, the Gouy phase shift should be taken into account [62]. The Gouy phase shift is given as:

$$\eta(z) = \arctan\left(\frac{z}{z_r}\right) = \arctan\left(\frac{2z}{b}\right) \tag{2.18}$$

where z_r is the Rayleigh length, z is the propagation distance, and $b = 2z_r$ is the confocal parameter.

For short distances from the focus point ($z \ll z_r$), the geometric wave vector is given as:

$$k_{geometric} = \frac{d\eta(z)}{dz} \approx \frac{2}{b} \tag{2.19}$$

Because the harmonics have the same confocal parameter and the fundamental laser and the wave vector are independent of the frequency, the geometric phase mismatch near the focus point is given by:

$$\Delta k_{geometric} = qk(\omega) - k(q\omega) = (q-1)\frac{2}{b} \qquad (2.20)$$

As can be seen, the contribution of the geometric phase mismatch is positive and this value can be changed by varying the laser's focus position inside the interaction medium [43].

d) Atomic dipole phase mismatch:

The dipole phase (also called trajectory) mismatch term is the phase of the atomic or molecular dipole which is the action acquired by the electron leading to the emission of the q^{th} harmonic in the continuum state and varies with the laser intensity. Since the laser intensity can vary spatially in both the longitudinal and radial directions, the atom dipole phase also varies axially as well as radially. This leads to reduced harmonic emission as well as strong spatial distortion [43][63]. The dipole phase mismatch is given by:

$$\Delta k_{dipole} = \alpha_q \frac{\partial I}{\partial z} = \alpha_q \frac{8z}{b^2} \frac{I_0}{\left(1 + \left(\frac{2z}{b}\right)^2\right)^2} \qquad (2.21)$$

where α_q are the electron trajectory coefficients (also referred to as the phase coefficients), around 1×10^{-14} cm^2/W for the short trajectory and 24×10^{-14} cm^2/W for the long trajectory [64], and I_0 is the peak laser intensity. The electron trajectory coefficients are closely related to the excursion time, i.e., the time electrons spend in the continuum. Hence the long trajectory has a larger coefficient, and as a result its emission has a larger phase mismatch and shorter coherence time compared to the short trajectory [65].

As a summary, the total terms of the phase mismatch in equation 2.9 for a focusing geometry HHG can be expressed as:

$$\Delta k = \frac{2\pi q}{\lambda} P(1-\eta)\,\Delta n - \eta P N_{atm} r_e \lambda \frac{(q^2-1)}{q} + (q-1)\frac{2}{b} + \alpha_q \frac{8z}{b^2} \frac{I_0}{\left(1+\left(\frac{2z}{b}\right)^2\right)^2} \quad (2.22)$$

As can be seen, the phase mismatch of the plasma dispersion can be balanced by the total of the neutral atom dispersion, the geometric and the dipole phase mismatch to keep $\Delta k = 0$.

2.2.4. Experimental control of the HHG phase matching

As expressed in equation 2.22, there are some experimental parameters that can be controlled to optimize the HHG process. The first two terms in the equation are the neutral atom dispersion and plasma dispersion, which have opposite signs and both are pressure dependent. Therefore, balancing their phase contributions by varying the pressure at a low degree of ionization can result in better phase matching. On the other hand, the laser intensity should be fixed at the optimum value around the ionization threshold to prevent the free electron dispersion that destroys the phase matching. Therefore, to generate HHG with a higher cutoff energy, it is possible to keep the laser intensity at a low level but to increase the driving wavelength [66][67][68].

When the phase-matching condition $\Delta k \approx 0$ is not practical, quasi-phase-matching (QPM) schemes can be invoked. In QPM, a phase mismatch is periodically fixed, with a periodicity corresponding to twice the coherence length. In this regard a weak counter-propagating IR field [69], weak static fields [70], modulated wave guides [71] or multiple gas jets [72][73] can be employed.

As crucial requirements for the CDI experiment, a table-top HHG source which is bright, narrow band, highly spatially coherent and temporally coherent should be implemented and developed. A high photon flux is desirable, since the required exposure time can be reduced and effects of the laser's instability are minimized. In addition, a shorter capture time also reduces the noise in the detecting device and hence increases the signal to noise of the diffraction pattern. On the other hand, a high spatial coherence ensures that the sample is uniformly illuminated and the diffraction is properly generated. In addition, the sample should be illuminated by a narrow bandwidth source and the diffraction pattern can be considered as the magnitude of the Fourier transform of the sample, where a few orders of harmonics and high temporal coherence of each harmonic are required.

Nowadays, HHG is generated mainly from three experimental geometries: gas jet, gas-filled fibre and gas cell. Since the first HHG experiment by McPherson [27], the gas jet-based experiment has become the most popular, and has successfully generated harmonics in the water window region [32] and has even extended to the 400 eV range using a helium jet [33]. In the gas jet configuration, the gas is passed through a nozzle into a vacuum chamber and the laser is focused into the gas stream. Although it is simple to set up, there are several limitations, such as short interaction length, non-uniform gas density along the path of interaction and lack of a laser guiding mechanism. These limitations can be overcome by using an alternative solution, the gas filled hollow core fibre, which typically has ~100 µm internal diameter, is 1-10 cm long and is filled with a low pressure of gas [41]. A higher conversion efficiency is achieved, thanks to the uniform gas density and the quasi-phase matching by modulating the diameter of the fibre, in which the resultant modulated laser intensity can improve the phase-matching condition and hence increase the HHG efficiency [71][74]. However, the complicated manufacturing and alignment process of the hollow core fibre is still a

disadvantage. An excellent alternative to generate high harmonic generation is the gas cell, which provides a uniform gas density and long interaction length, as well as a self-guiding mechanism. The gas cell is basically a sealed container, which has a glass entrance and a 1 mm thick aluminium plate at the exit, where a hole about 100 µm diameter is drilled by the driving laser as an exit aperture for the gas and the laser; thus the alignment process is simpler compared to other geometries. The interaction length can be changed by varying the length of the gas cell, or by shifting the focus position of the laser around the exit hole. The solid structure of the gas cell also allows the generation of high harmonic radiation with a high gas pressure, as will be reported later in this chapter. The gas cell configuration also has some limitations. When the field propagates through a long interaction medium, nonlinear effects such as self-defocusing, wave-front distortion, and Gouy phase shift may affect the phase matching condition. However, the effect of the Gouy phase shift and other phase mismatch terms can be balanced by adjusting the focus position of the laser inside of the gas cell and varying the laser intensity using an aperture before the lens. With these outstanding features, the gas cell geometry was chosen and developed at the CQOS laboratory and will be described in the following section.

2.3. Table-top HHG experimental setup

2.3.1. Femtosecond laser system

The high power femtosecond laser system consists of 3 modules: a seeding laser and 2 amplifier stages as shown in Figure 2.6. The output laser is carrier-envelope phase (CEP) stabilized with a 30 fs pulse duration at 1 kHz repetition rate. Using the first amplifier stage alone, laser pulses around 810 nm with an energy of 2 mJ per pulse can be generated, mainly to produce harmonics around 30 nm with

argon gas. With the second amplifier module, the pulse energy can be raised to 10 mJ and is able to generate high harmonics with wavelengths down to 4 nm with helium gas.

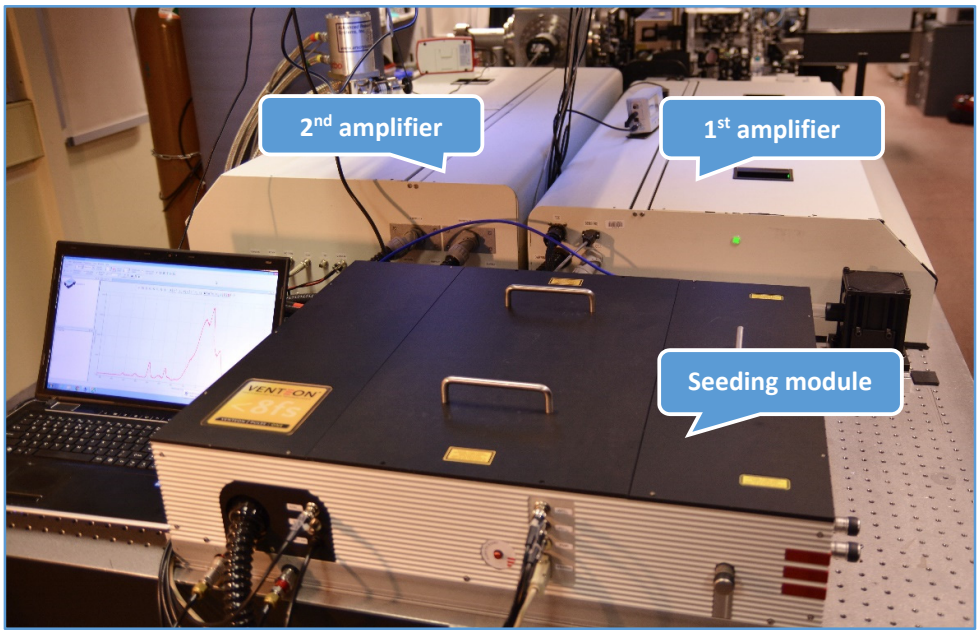

Figure 2.6: The high power femtosecond laser system, showing a seeding module and two amplifier stages.

a) Seeding laser:

The laser system uses a Ti:Sapphire Venteon Pulse One with CEP stabilization as the seeding module [75]. The laser is pumped by a low noise 5 W diode-pumped solid state (DPSS) laser and the CEP stabilization system is based on a *f* - *2f* interferometer [76], which only consumes 10% of the total laser power. The output of the laser for experiments is not affected by any temporal and spatial dispersion of the stabilization process. In addition, the locking electronics is based on a Menlo Systems (XPS800 Syncro), which provides a touch screen interface for easy monitoring and controlling the system. Typical characteristics of the seeding module are shown below:

Pulse duration	< 8 fs
Repetition rate	80 MHz
Output power (average)	> 600 mW
Spectral bandwidth (FWHM)	> 200 nm

Table 2.2: Specifications of the Venteon Pulse One seeding laser system.

The mode-locked output laser has a FWHM bandwidth > 200 nm centred at 810 nm, and is seeded to the amplifier stages to produce higher energy laser pulses.

b) Amplifier modules:

The laser energy is amplified by the first amplifier stage (Quantronix Odin-II HE), which is a multi-pass Ti:Sapphire system, to an energy > 2 mJ based on the chirped-pulse amplification method [77]. This amplifier is pumped by a Quantronix Darwin-527 pump laser. The principle of the amplifier system is as follows: the laser pulse is stretched by a negative chirp grating, the pulse energy is amplified by multi-passing the gain medium and the resultant pulses are compressed by a positive chirp grating. The output pulses are selected by a Pockels cell with a repetition rate of 1 kHz. After leaving the first amplifier stage, the characteristics of the beam are as shown in Table 2.3:

Pulse duration (FWHM)	30 fs
Repetition rate	1 kHz
Pulse energy	> 2 mJ
Centre wavelength	810 nm

Table 2.3: Characteristics of the laser after the first amplifier stage.

If higher pulse energy is required (up to 10 mJ), the laser pulse are diverted to the second amplifier stage before going to the compressor. This amplifier stage is a Quantronix Cryo Add-on, which is pumped by the same Quantronix Darwin-

527 pump laser similar to the first stage. The main component is the Cryo-crystal cell, which is cooled to 100 K in a vacuum chamber to maintain stability and output power. The amplified laser pulses are compressed again to produce ultrashort pulses by a pair of gratings before leaving the amplifier.

c) Optical parametric amplifier:

To generate the infrared laser field, an optical parametric amplifier (Quantronix Palitra OPA) is installed after the second amplifier stage. Parametric amplification is a three-wave mixing process involving the exchange of energy from a powerful optical wave with high frequency (called the "pump" ω_p) to two lower energy waves with lower frequencies (the "seed" ω_s and the "idler" ω_i), respectively. These signals satisfy the energy conservation criterion: $\omega_p = \omega_s + \omega_i$, where the wavelength of the resultant signals depends on the phase-matching condition, the temporal overlapping and the nonlinear crystal properties. The power of the seed signal is amplified by the pump signal while propagating (collinearly or non-collinearly) through the crystal. The Palitra module uses a white light continuum source as the seed of the OPA, which is produced by focusing the ultra-short input beam in a sapphire crystal. A Bismuth Triborate (BiB_3O_6 or BIBO) crystal is used as the nonlinear medium for the amplification process, which has a higher conversion efficiency, wider wavelength tuning range and easier maintenance compared to a typical Beta Barium Borate (β-BaB_2O_4 or BBO) crystal [78]. The OPA is fitted in a one-box module, which includes a white light continuum generator, a signal pre-amplification stage (first stage) and a power amplification stage (second stage). At each stage, the delay between the pump and signal waves can be adjusted to achieve temporal overlap, and the angle of the crystal can be tuned to optimize phase matching.

2.3.2. HHG experimental arrangement

The HHG experimental apparatus is arranged in four modules: generation, filtering, application and detection modules. The main components of the experiment are shown in Figure 2.7. The high energy laser is focused into a gas cell to generate the high harmonic radiation, and then the output beam is filtered by a series of pinholes and spatial filters to block the fundamental laser and to select the harmonic wavelengths of interest. The experimental chamber consists of various motorized stages and a set of samples for source characterization and imaging applications. The detection module consists of a grazing incidence spectrometer and a CCD camera, which can be replaced by a camera to capture the diffraction pattern in the case of performing coherent diffractive imaging.

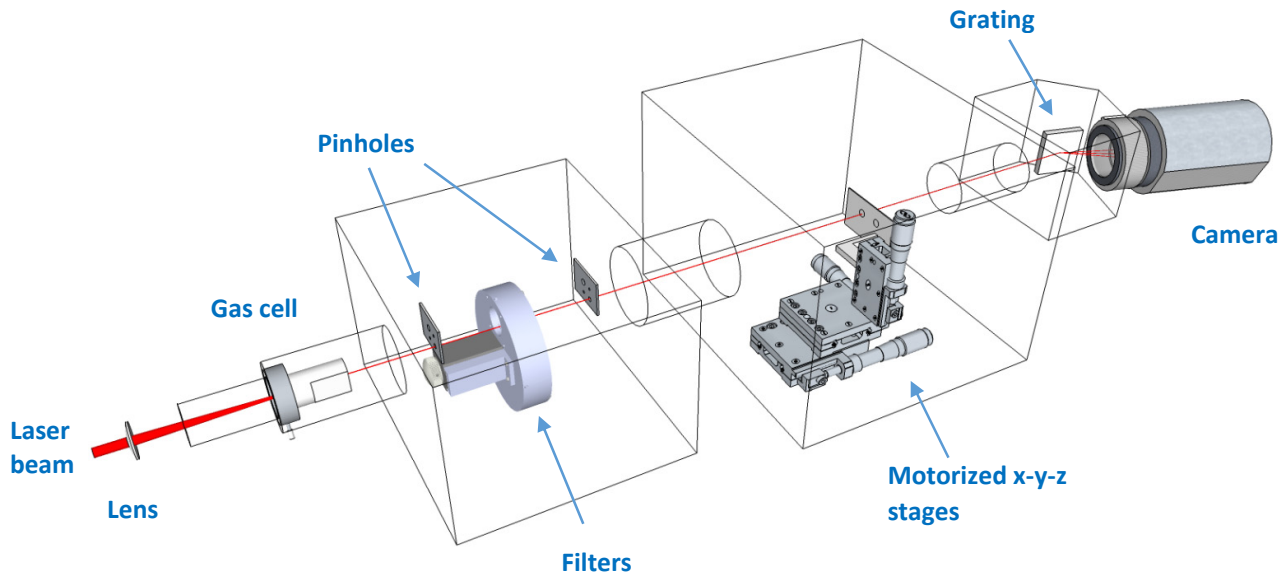

Figure 2.7: Simplified HHG experimental arrangement which shows only the important apparatus in two vacuum chambers and an attached spectrometer.

2.3.2.1. *Generation module:*

The generation module consists of a lens and a gas cell, as shown in Figure 2.8. After passing the aperture the laser beam is focused into the gas cell by a 1 inch diameter, 40 cm focal length fused silica lens. The dispersion due to the lens is negligible, where the change of focal length (Δf) is about 500 µm and the pulse is lengthen by 5 fs [126]. The effect due to the lens dispersion is more severe for few-cycle laser pulses than many-cycle laser pulses; in this case with 30 fs pulses this dispersion can be neglected. This lens is mounted on an x-y holder, which is placed on a motorized translation stage in the z direction (laser propagation direction). The x-y position is carefully adjusted to align the laser beam at the centre of the lens, since a small misalignment of the focus position in the x-y direction decreases the high harmonic photon flux dramatically. The z-direction translation stage allows the focus position of the fundamental laser inside the gas cell to be precisely controlled manually by a micrometer screw or electronically by a Zaber T-LA28A linear motor. On the other hand, the interaction length in the HHG process can be scanned and the optimum length selected to generate as much photon flux as possible.

The interacting gas is contained in a 30 cm long, 1 inch diameter gas cell, which is divided into two sections: the outer atmosphere and the inner vacuum sections. The outer section has a glass entrance for the laser and an inlet to supply the gas to the cell. The inner section is placed inside a small vacuum chamber, in which the pressure is kept around 10^{-2} Torr. At the end of this gas cell is a laser-drilled pinhole, which allows the laser beam and the gas to exit the gas cell. The gas cell also has a flat glass window for observation of the generated plasma inside the cell near the focus point, which allows the focus position of the fundamental laser to be accurately selected. Depending on the wavelength of interest for the experiment, various gases at different pressures are supplied to the gas cell via a

pressure stabilization system. Since the phase-matching optimization process relies heavily on the optimum pressure of the gas cell, this pressure must be kept stable with an error less than 1 Torr. Furthermore, to investigate the dependence of the high harmonic intensity on changing the gas cell pressure, the pressure must respond quickly to the set point to keep up with the spectrum acquisition process.

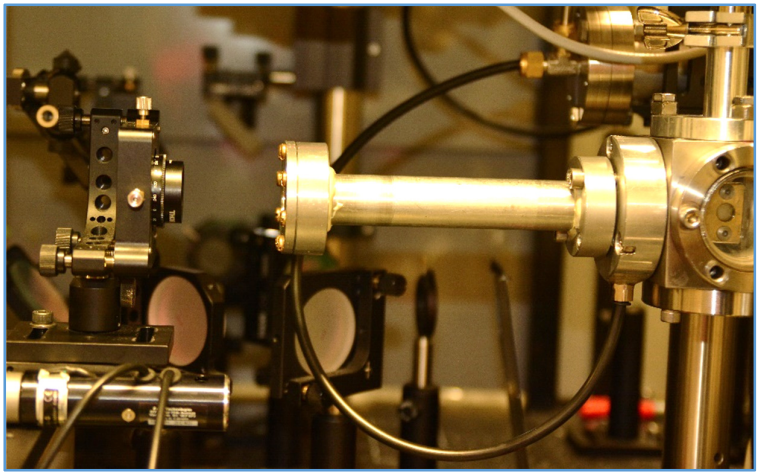

Figure 2.8: Lens on a translation stage and a long gas cell setup. The gas is supplied by a black tube as shown.

This challenge is solved by employing a pressure stabilization system, which consists of an Alicat single valve pressure regulator, a Pfeiffer CMR 361 pressure gauge, a TPG 256A MaxiGauge controller and a LabView program on a computer. The pressure gauge is connected near the gas inlet of the gas cell which measures the pressure of the gas cell in the range 0.1 – 825 Torr. The pressure value is read by a MaxiGauge controller and sent to the computer which runs the stabilization program. Once a set point is selected in the software, a valve opening value is calculated by a PID algorithm and sent to the Alicat valve, which is placed between the gas bottle and the gas reservoir of the cell. The PID parameters are carefully optimized to minimize fluctuations of the gas pressure with any set point with a sampling rate of 25 Hz. The interface of the pressure

stabilization is shown in Figure 2.9, where a graph of the gas cell's pressure when a set point of 200 Torr is shown. The system has been proven to have a long term stability of the pressure stabilization, with an error less than ±0.5 Torr for any set point within the range of the gauge.

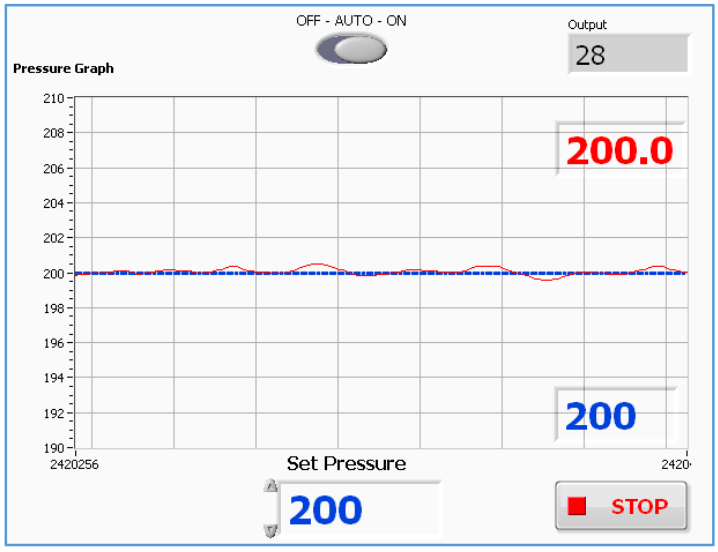

Figure 2.9: Pressure stabilization software interface, showing a set point of 200 Torr (dashed blue) and an actual pressure response (solid red) with an error < 0.5 Torr.

2.3.2.2. *Filtering module:*

The filtering module consists of several pinholes and metal spatial filters, in order to block the fundamental laser and to avoid scattering of the light inside the vacuum chamber. The pinholes whose diameters range from 200 µm to 2 mm are placed precisely along the beam path and their positions are controlled by piezo linear motors. To block the fundamental laser beam that may cause damage to the downstream detector, thin metal filters such as aluminum or zirconium are installed on a Thorlabs FW103H Filter wheel, in which the filter can be selected

by an accompanying software. Furthermore, the spatial filters also select the wavelength range of interest. For the coherent diffractive imaging described in this thesis, harmonics around 30 nm are chosen by a 200 nm thick Al filter. The transmission characteristics of this filter are shown in Figure 2.10, which exhibits a sharp cutoff near 17 nm and ~ 60% transmission at wavelengths around 30 nm.

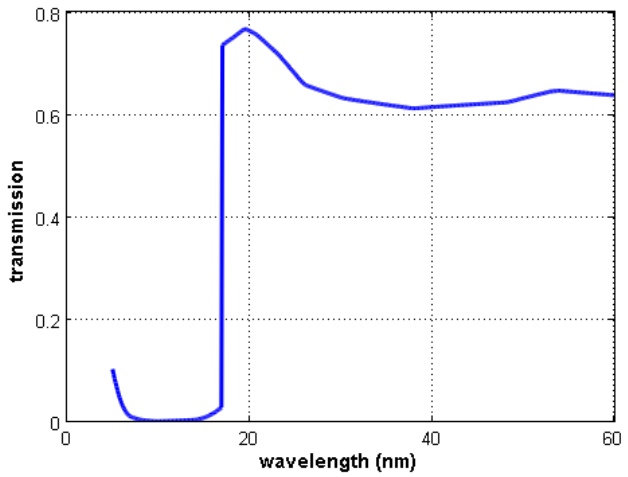

Figure 2.10: Transmission characteristics of a 200 nm thick Al filter. Data is taken from [79].

The resultant harmonic beam is passed through another pinhole to block scattering and to re-shape the beam profile before entering the application chamber. This chamber is kept at a pressure of less than 10^{-3} Torr by a Pfeiffer HiPace 700 turbo pump, backed by a membrane pump.

2.3.2.3. *Application module:*

The application module is installed inside a large vacuum chamber, which consists of apparatus and samples to characterize the high harmonic beam and to perform the coherent diffractive imaging experiment. The samples are mounted on an x-

y-z motorized translation stage, which allows the position of the sample to be precisely controlled. These motors (Zaber T-LA60A linear motor) are monitored and controlled by a LabView program on a computer, in which the step size is as small as 100 nm. For the coherent diffractive imaging experiment, another x-z translation stage with similar motors is installed to support the wavelength-selecting reflective and focusing mirrors. The harmonic radiation with wavelength around 30 nm is selected and focused into the sample by the mirrors, which effectively increases the photon flux and reduces the exposure time. The details of this experiment are described in chapter 4.

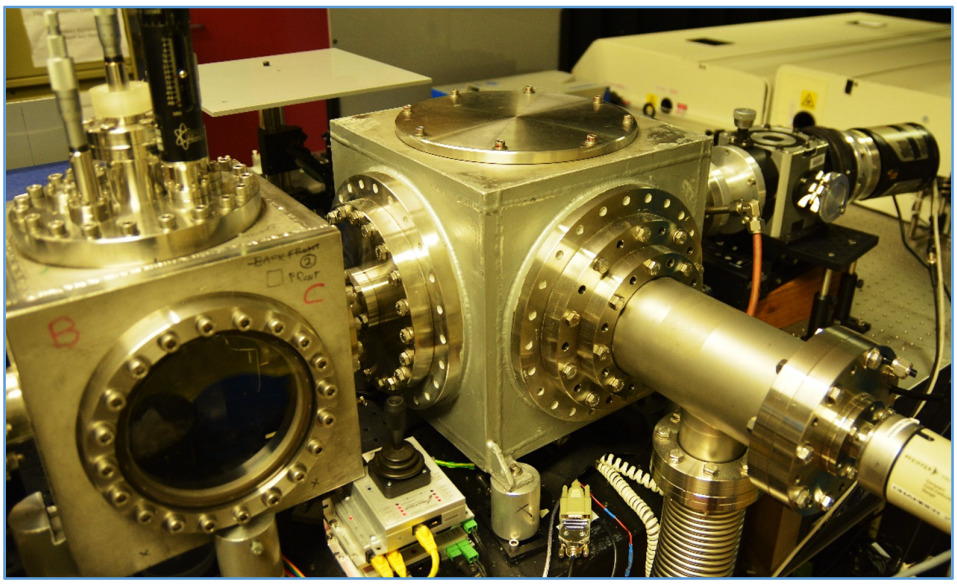

Figure 2.11: Filtering and applications chamber with the spectrometer and attached camera downstream.

The whole chamber is kept at a pressure less than 10^{-5} Torr by an Agilent TV 701 turbo pump system while the actual pressure is monitored by Pfeiffer IKR 270 vacuum gauges.

2.3.2.4. *Detection module:*

When measurement of the spectrum is required, a spectrometer (Setpoint GIMS#4) is installed downstream from the applications chamber. The gratings used in the spectrometer can be rotated by a micrometer, which allows the region of the wavelength of interest to be selected. Four different gratings with different groove spacings can be fitted to the spectrometer to cover the wavelength range from 4.4 to 85 nm, where finer spacings are used for shorter wavelengths and higher resolution, as shown in Table 2.4. In the experiment described in this thesis, a grating with 300 grooves/mm is used since it is the most effective for wavelengths around 30 nm.

Grating (grooves/mm)	Wavelength range (nm)	Resolution (Å)
150	35.4 – 85.0	4.0
300	17.7 - 42.5	2.0
600	8.9 – 21.3	1.0
1200	4.4 – 10.6	0.5

Table 2.4: Specifications of the gratings used in the spectrometer.

The detector attached to the spectrometer is a Princeton Instruments Pixis-1024B CCD camera, which has a resolution of 1024×1024 pixels and a pixel size of 13.5 µm. A spectrum with a dynamic range up to 16-bit (65535 levels) can be captured with a high speed mode (2 MHz) or low noise mode (100 kHz) ADC. The camera is fully controlled by a WinView program via an USB connection, and the camera's shutter signal is used to drive a motorized shutter and synchronize with the motors of the translation stages.

For the coherent diffractive imaging experiment, the spectrometer is replaced by another camera, a Pixis-2048B, which has a larger sensor dimension of 2048×2048 pixels. Larger sensor area allows high angle diffraction data to be collected and hence increases the resolution of the reconstructed image. This camera is attached directly to the experimental chamber to keep the distance between the sample and the detector within the acceptable distance (3 -6 centimeters, see chapters 4 and 5). At room temperature, the CCD suffers an inhomogeneous background noise and it is difficult to clean up using background subtraction and averaging. At lower temperature, the noise is more homogenous and diffraction data with higher signal to noise is obtained, which is crucial for reconstructing a high resolution image. To achieve the best diffraction pattern, the camera is cooled to -40°C when taking data, otherwise it is left at room temperature since the sensor becomes dirty quickly at the low temperature.

2.3.3. Laser beam pointing stabilization system

2.3.3.1. *Introduction:*

Fluctuations of the laser pointing is a common problem in laser experiments; they cause a temporal variation of the laser energy, as well as reducing the coupling efficiency between the amplifier states. In the current HHG system at the CQOS laboratory, beam pointing jitter can be observed clearly at the output of the second amplifier while the output beam of the first amplifier is quite stable. The drift is likely due to thermal expansion of the optical elements and the vibration of the benches and support structures. In addition, it is likely due to the coupling mirrors between amplifier states which are not steady enough and are easily displaced. The fluctuations can be classified as short-term and long-term drifts; the short-term variation can be seen as high frequency noise (10Hz – 1 kHz), while the long-term drift varies from a few seconds up to 10 minutes. These fluctuations

can be minimized by using a closed loop feedback with a detector and steering mirror to compensate the drifting of the optical system.

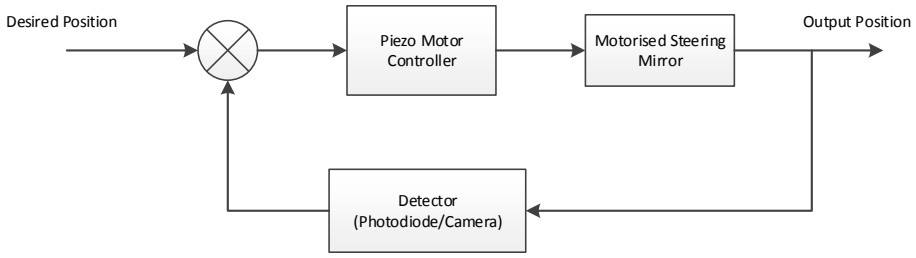

Figure 2.12: Block diagram of the beam pointing stabilization system.

In recent years, many approaches have been developed to solve this problem, mainly using a position sensitive detector (PSD, including quadrant photodiode) and a CCD camera to detect the shift of the beam position. The experiment is set up as in Figure 2.12, where a piezo-driven mirror is used to stabilize the pointing of the beam which comes from the second amplifier.

2.3.3.2. *The stabilization system background:*

With high sensitivity and fast frequency response (10 – 100 kHz), position sensitive detectors (PSD) are widely used with PID (proportional-integral-derivative) controllers to adjust the steering mirrors to stabilize the beam pointing. An early stabilization system, which was built by Breitling et al, used a 2 cm-diameter quadrant photodiode and a computer to reduce the fluctuations by 50% at a 20 Hz sampling rate [80]. In recent systems, Kanai has stabilized a 1 kHz pulse laser from 40 µm fluctuation to within 1 µm to feed a hollow fibre compressor [81]. The system used a two-dimensional PSD (Hamamatsu S1880) with an active area 12×12 mm with a signal processing circuit (including sample

and hold functions) and a PID controller to detect and stabilize the beam at a 100 Hz sampling rate. Although the experiment showed that long-term as well as short-term drifts could be minimized significantly, it is only suitable for a laser system with a small beam profile.

The other automatic alignment system which was built by Kral used two steering mirrors with two 3 mm quadrant photodiodes and a PC to stabilize the beam position of a 10 Hz pulse laser system [82]. The maximum error is 10% (0.5 mm) of the beam diameter (5 mm) which is too large. Furthermore, the system is relatively slow since it takes 3 seconds to sample and average 30 shots of laser pulses to calculate the beam position.

Newport also produces a beam position sensing detector which can operate as fast as 60 kHz, together with a fast steering mirror (FSM) controller, and this system can be used as a beam tracker and stabilizer [83]. However, the cost is relatively high (~$3000 for the detector and $7000 for the controller), and also the sensing area of the detector is only 9×9 mm which is too small for the laser system with large beam diameter in the CQOS laboratory.

Although laser beam position detectors that use position sensitive detectors and quadrant photodiodes have the advantage of high sampling rate and simple data processing, these detectors are suitable for a laser system with small beam diameter (less than 5 mm), or a focus lens is required (which introduces more error) due to the limiting size of the sensing area. Furthermore, the large beam profile and its high power causes the photodiode to saturate easily, making it difficult to track the position. In addition, the filter which converts the pulse signal to a DC signal introduces some noise to the stabilization process, and this problem is clearly seen in the previous controllers that were built.

On the other hand, with the development of the image capturing and processing system, CCD cameras are widely used to track and stabilize the laser beam pointing. Stalmashonak has developed a laser stabilization system using two lenses to create two separate images on a single CCD camera to control two piezoelectric mirrors [84]. The system operates at 1 Hz which only solves the long-term drift problem while the high frequency noise is still present. To process the image, a National Instruments (NI) Vision Toolkit provides intensive functions to calculate the centre of the laser beam precisely [85]. Combining with a NI Fuzzy Controller toolkit, Singh developed a laser stabilization system that operates at 30 Hz to reduce the fluctuations from ±60 µrad (±20 pixel) to ±5 µrad (±1 pixel) [86]. However, the fluctuations are still noticeable because the picomotors (New Focus, 8302) used for steering the mirrors, which are based on a turning screw and have uneven steps, cause an error to the feedback loop.

By integrating a high frame rate CCD camera with a new, powerful software algorithm, the beam pointing stabilization system for the HHG experiment has been proven to stabilize the laser pointing to less than 0.5 pixels, where the short-term and long-term drifts have been corrected with a sampling rate of 100 Hz.

2.3.3.3. *The stabilization system setup:*

The stabilization system consists of a steering mirror, a piezo motor driver, a camera and a computer that runs the program. The steering mirror (Thorlabs KC1-PZ piezoelectric mirror) is placed at the exit port of the first amplifier, which is controlled by the motor driver (Thorlabs MDT693). The laser beam after the second amplifier is sampled to illuminate on a screen, where the intensity is recorded by the camera (Basler scA640-120gc) and then sent to the computer which runs a LabView based stabilization program.

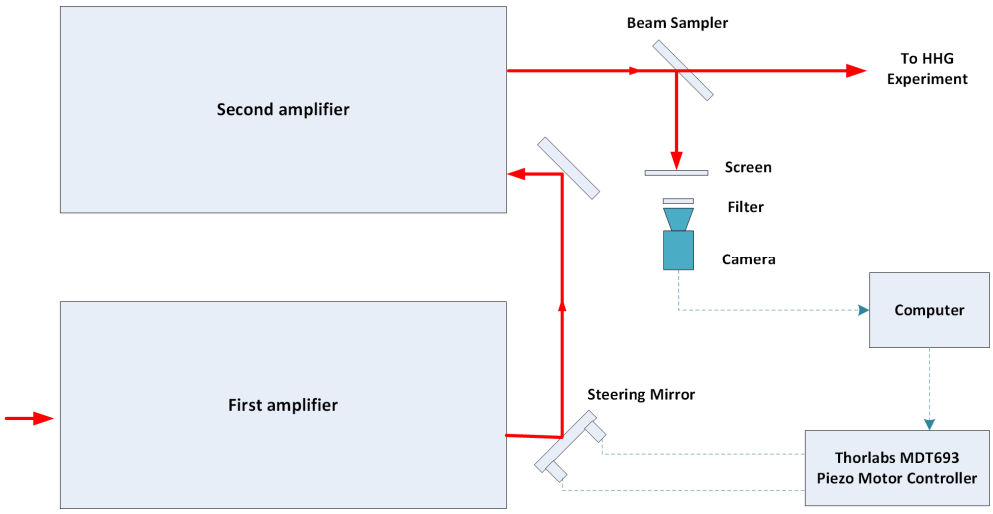

Figure 2.13: The laser pointing stabilization system setup.

The laser spot on the screen captured by the camera is processed by the National Instruments Vision software package, in which the intensity profiles along the x and y directions are integrated and fitted with a Gaussian function to determine the beam's centre with a frame rate up to 100 Hz. Then these centroids are compared with the expected values (in the middle of the camera) and the piezo motor's steering angles are calculated by a PID algorithm. In addition to correcting the beam's centre error to zero, the PID parameters are carefully optimized to minimize overshoot while maintaining a fast response of the piezoelectric mirror.

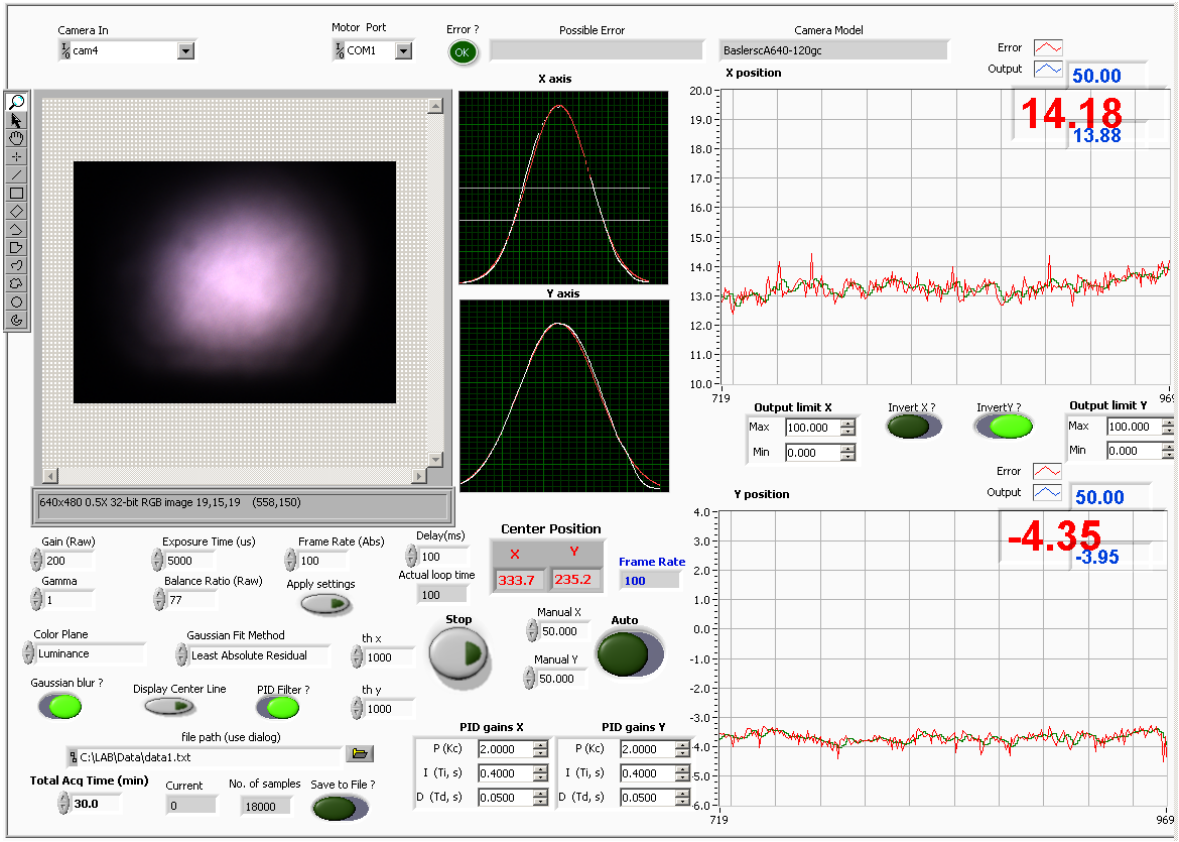

Figure 2.14: The interface of the beam pointing stabilization system.

2.3.3.4. *The stabilization performance:*

The performance of the beam pointing stabilization is shown in Figure 2.15, where data is recorded with and without the auto stabilization by the Basler camera for a period of 1.5 hours. As can be seen, without the stabilization, the beam's centre has drifted about 6 pixels (corresponding to 300 μm or 2.5% of the beam FWHM diameter) in both the x and y directions. This beam continuously shifts throughout the day and without any adjustment, the drift can be as large as 30 pixels. However, the beam centre is locked to zero with an error of less than 0.5 pixels when the auto stabilization is turned on. For a long day operation, the

system is able to lock the beam centre as long as the steering mirror is still within the operating limit.

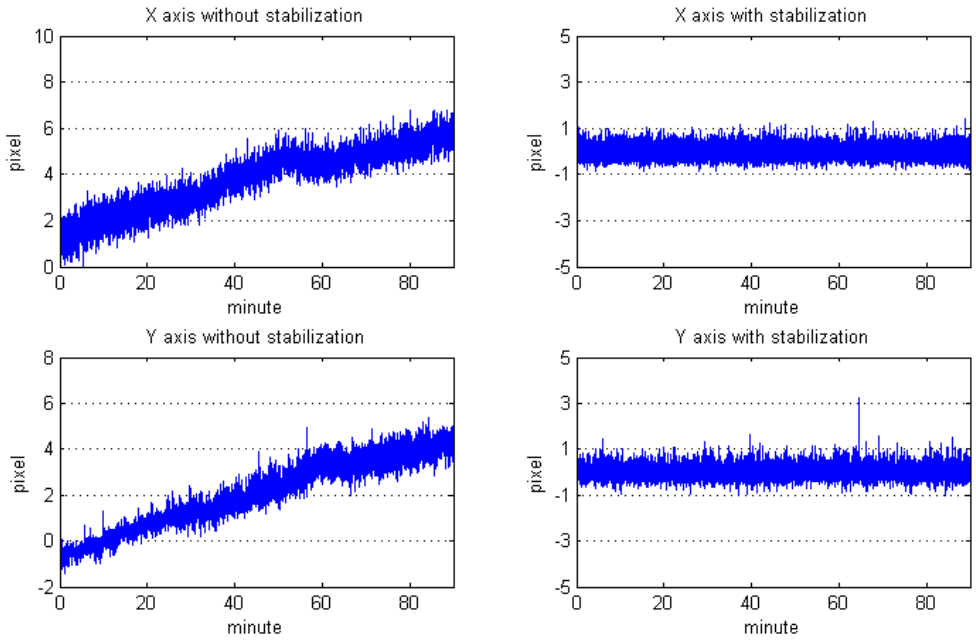

Figure 2.15: The beam centre recorded by the stabilization camera without and with the stabilization over 90 minutes.

The performance of the beam pointing stabilization system is also confirmed by the stability of the high harmonic beam which is recorded by the CCD camera attached to the experimental chamber. In this stability experiment, a high harmonic beam is generated by the 810 nm driving laser with argon and then filtered by a 200 nm thick aluminum film. The beam profile of the high harmonic beam is shown in Figure 2.16, which is fitted to a Gaussian function and the peak (beam centre) coordinates are calculated. The data is recorded by the camera every 45 seconds at the same time as the data shown in Figure 2.15, and then the high harmonic beam centres are plotted in Figure 2.17.

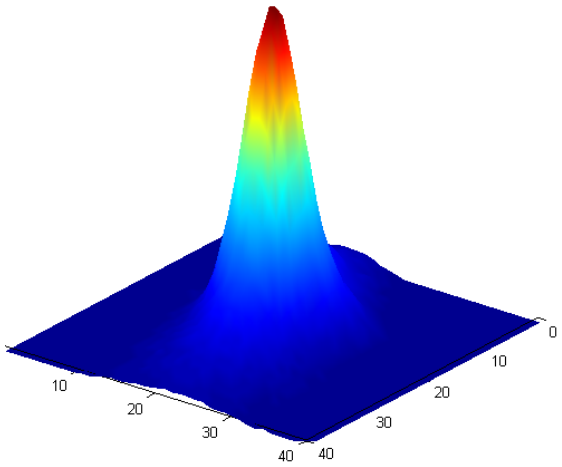

Figure 2.16: The high harmonic beam profile captured by the Pixis CCD camera (cropped to 40×40 pixels), which is a good fit of a Gaussian function.

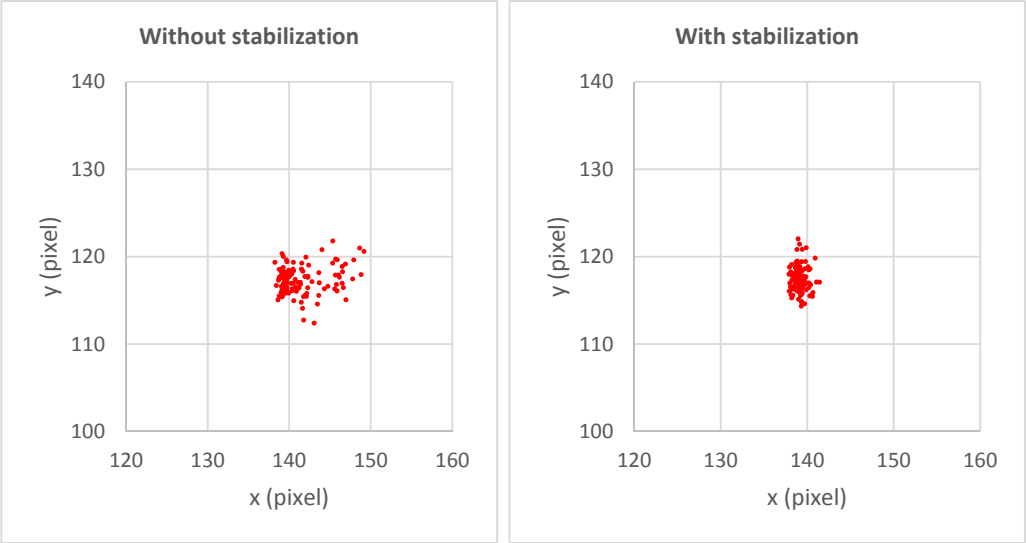

Figure 2.17: The high harmonic beam centre without (left) and with (right) the stabilization over 90 minutes.

Without the stabilization system, a drifting of the high harmonic beam in both x and y directions is clearly observed. Over 90 minutes, the beam centre has shifted about 10 pixels in both directions, which corresponds to ~135 µm movement, and will be worse for a longer experiment time. This shifting is significantly reduced by the stabilization system, which is only 7 pixels (95 µm) in the y direction and

3 pixels (40 µm) in the x direction. The beam centre will be locked at a predefined position as long as the piezo steering mirror is within the limit.

2.4. Generation of coherent, few harmonics XUV source

For the coherent diffractive imaging application, a narrow bandwidth source is desirable, which affects the achieved resolution of the reconstructed image. A single harmonic can be selected by a spectrometer or band pass mirror, but the transmission of the optics in the XUV range is low and hence limits the usable photon flux. Therefore, the generation of a bright few harmonic source, or even a single harmonic source, is a crucial requirement to increase the efficiency of the source.

High harmonic generation is a highly nonlinear process and is very sensitive to the experimental conditions. The conversion efficiency is influenced by many parameters that are linked together. Therefore, simply increasing the laser intensity or gas pressure does not result in increasing the high harmonic photon flux. In fact, the experimental parameters have to balance the phase matching condition, as well as other effects such as absorption [87], defocusing [88][89] and dephasing [41]. In order to generate a bright harmonic source around 30 nm, which is described in this dissertation, the influence of the harmonic intensity on the pressure and the interaction length is investigated to calculate an optimum value.

Following the Constant model, the intensity of the q^{th} harmonic is given by [42][60]:

$$I_q \sim N_a^2 A_q^2 \frac{1 + \exp(-2\alpha_q L) - 2\exp(-\alpha_q L)\cos(\Delta k_q L)}{\alpha_q^2 + \Delta k_q^2} \qquad (2.23)$$

where α_q is the absorption coefficient, Δk_q is the phase mismatch, L is the interaction length, A_q is the atomic response of the qth harmonic and N_a is the atomic number density. The phase mismatch can be simplified to two terms: one dependent (dispersion) and one independent (geometric) of the pressure [90]:

$$\Delta k_q = \Delta k_g + P\Delta k_d \tag{2.24}$$

where the geometry phase mismatch is positive and the combined dispersion phase mismatch (atom + plasma) is negative. Hence the dependence of the harmonic intensity on the pressure, interaction length and absorption coefficient can now be calculated.

2.4.1. Dependence of the harmonic intensity on pressure

To investigate the response of the harmonic intensity versus the change of the gas cell pressure, a high harmonic beam is generated with a 810 nm driving laser with argon in which the pressure is varied from 20 to 210 Torr. The driving laser intensity is adjusted by an aperture and the focus position is optimized near the exit hole inside the gas cell for maximum harmonic flux.

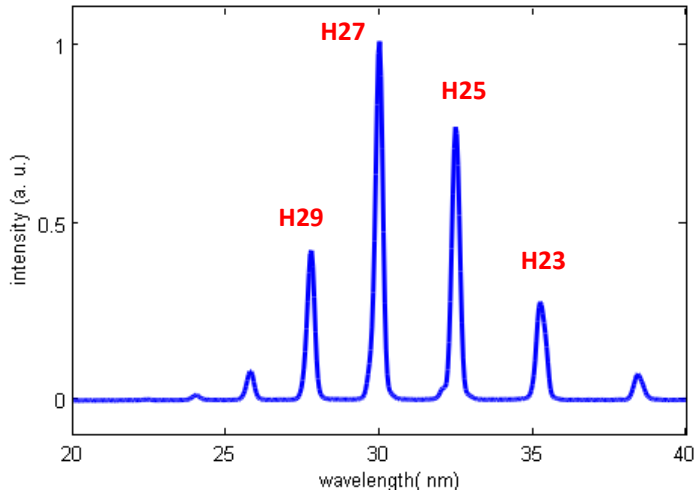

Figure 2.18: Spectrum of the HHG signal using argon at 70 Torr and a 810 nm laser, in which the harmonic orders are indicated.

A spectrometer and a camera are installed downstream from the experimental chamber to capture the spectrum of the HHG signal. A typical optimized spectrum is shown in Figure 2.18. With the pressure stabilization system, the gas cell pressure, which can be stabilized with an error < 1 Torr, is slowly increased and the change of the spectrum is recorded. This change is shown in Figure 2.19:

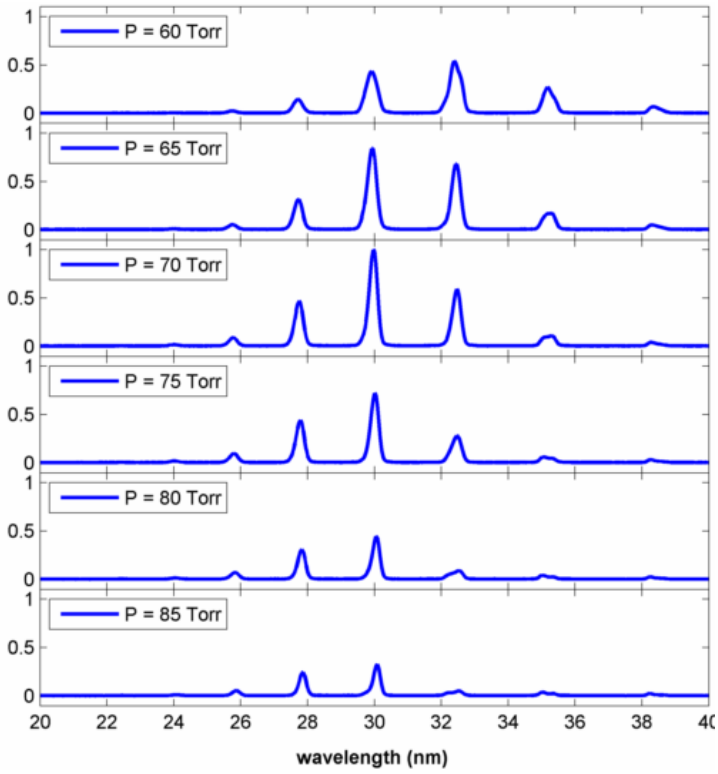

Figure 2.19: Change of the HHG spectrum as the pressure is increased.

As seen in the figure, the highest intensities of the harmonics are generated with a pressure around 70 Torr, at which 3 major harmonics are generated around 30 nm (27^{th} harmonic). To investigate the response of a single harmonic of interest, the response of the 27^{th} harmonic versus pressure is shown in Figure 2.20. By using equation 2.23, this response is fitted as a function of the pressure, where the interaction length L, the absorption coefficient α_q, and the phase mismatch

coefficients Δk_g and Δk_d are constants. The fitting equation with the pressure P is defined as:

$$F = \frac{1 + \exp(-2\alpha_q L) - 2\exp(-\alpha_q L)\cos((\Delta k_g + P\Delta k_d)L)}{\alpha_q^2 + (\Delta k_g + P\Delta k_d)^2} \quad (2.25)$$

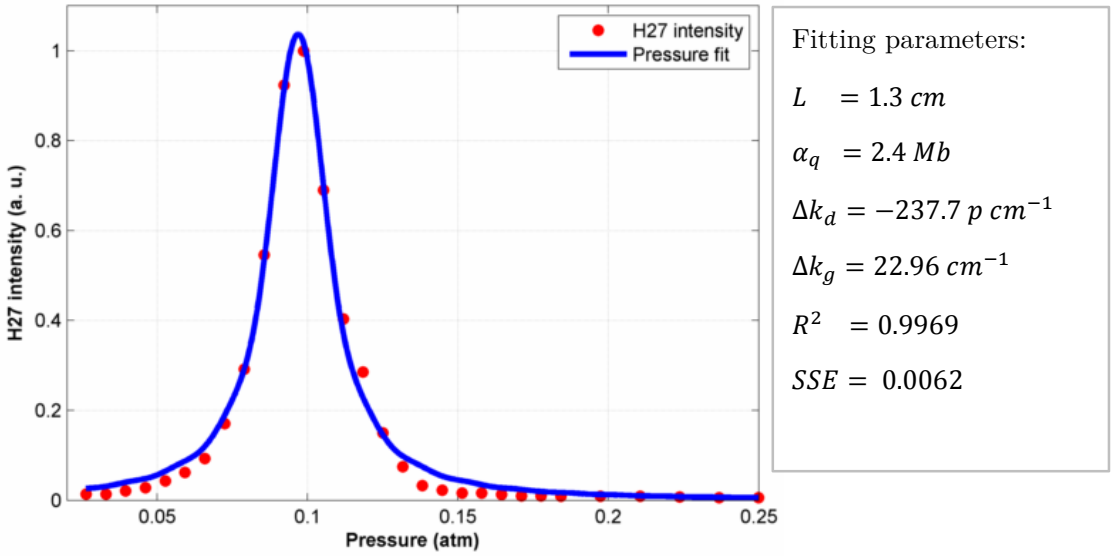

Figure 2.20: Dependence of the H27 intensity on pressure (red dots) and the fitted curved (blue line) with the shown fitting parameters.

Each data point represents the integrated intensity over a short exposure time (0.01 s) and it has been averaged over the area that fully covers the harmonic spectrum on the CCD to minimize the noise and reduce the error in the fitting. The excellent fitting of the dependence of the harmonic intensity on pressure suggests equation 2.25 is a reasonable approximation of the harmonic intensity. Furthermore, from the fitting, experimental parameters can be determined. The atom absorption cross section of argon at 30 nm is 2.4 megabarns (Mb), which is consistent with the data given by Samson [91]. As can be seen, the H27 intensity increases as the HHG is phase-matched with the increase of pressurezz and reaches a maximum at a pressure around 70 Torr. At higher pressures, the absorption of the harmonic signal becomes dominant, and hence the harmonic intensity decays and no harmonic can be seen for pressures > 200 Torr. From the fitting (Figure

2.20), the interaction length is calculated as 1.3 cm and the geometric phase mismatch is positive, while the dispersion phase mismatch is negative as expected.

2.4.2. Dependence of the harmonic intensity on the medium length

A similar experiment is performed to investigate the dependence of the harmonic intensity on the medium length, where the pressure is fixed at 70 Torr and the laser intensity is optimized for maximum photon flux available. The focus position of the laser inside the gas cell is scanned by the motorized translation stage with a step size of 200 µm over a distance of 20 mm. Figure 2.21 shows the change of the HHG spectrum versus the increase of the medium length.

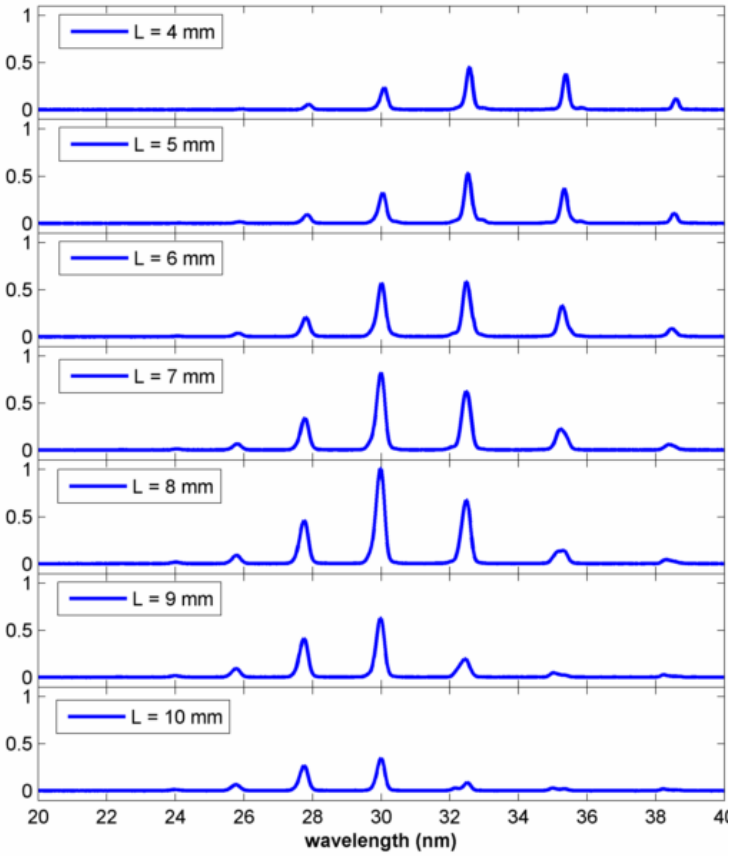

Figure 2.21: Change of the HHG spectrum when the medium length is increased.

As can be seen, the contribution of different harmonics to the spectrum can be changed by adjusting the medium length, in this case the focus position of the laser inside the gas cell. In addition, a narrow bandwidth source (3 harmonics) can be generated and a harmonic beam with wavelength around 30 nm (27^{th} harmonic) can be enhanced by choosing an interaction length around 8 mm.

The response of a single harmonic can be further investigated by considering the phase-matching condition. From equation 2.23, the response of the harmonic intensity versus interaction length can be fitted to the following equation:

$$F = \frac{1 + \exp(-2\alpha_q L) - 2\exp(-\alpha_q L)\cos(\Delta k_q L)}{\alpha_q^2 + \Delta k_q^2} \tag{2.26}$$

Recall that Δk_q is the total phase mismatch, where the geometrical phase mismatch depends on the interaction length. Therefore, the total phase mismatch can be written as:

$$\Delta k_q = L\Delta k_g + \Delta k_d \tag{2.27}$$

where Δk_g is the geometric phase mismatch constant (positive) and Δk_d is the dispersion phase mismatch constant (negative).

The dependence of the H27 intensity on the interaction length is shown in Figure 2.22, where the experimental data is shown as red dots and the fitted equation is shown as a blue line. As the interaction length increases, the harmonic intensity increases correspondingly in the phase-matched region. If the medium length is increased further, the harmonic intensity decreases because of the re-absorption effect. The fitted absorption coefficient $\alpha_q = 2.5\, Mb$ is well matched with the value taken from the pressure dependence fit and the data in [91].

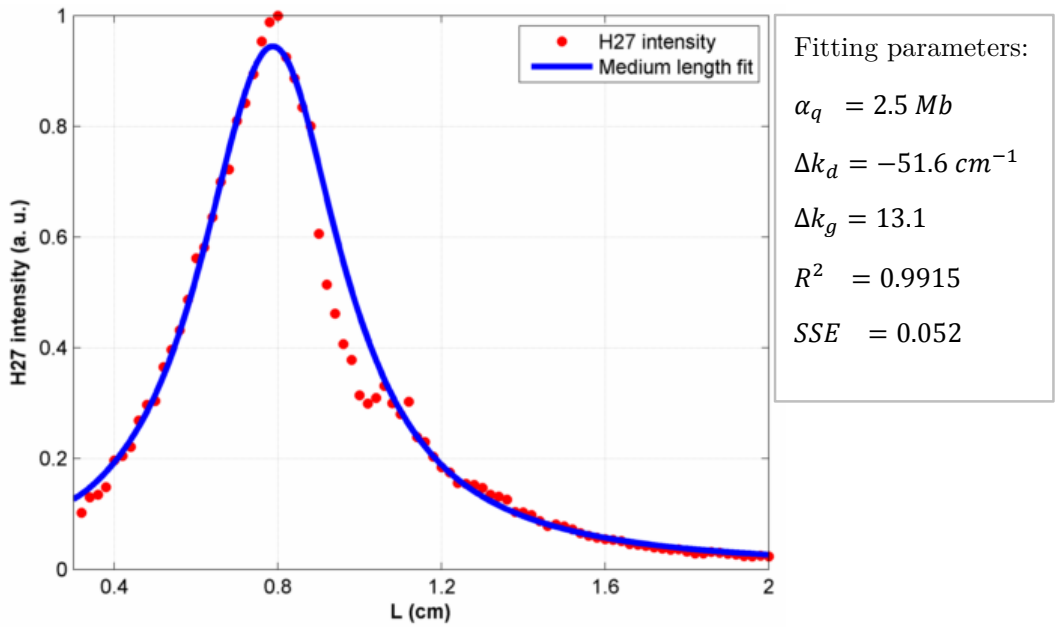

Figure 2.22: The dependence of the H27 intensity on the medium length (red dots) and the fitted curved (blue line) with the shown fitting parameters.

As a conclusion, the effective spectral range and the relative weight of single harmonic orders of the harmonic beam can be controlled by the phase-matching parameters. By an appropriate choice of species of gas, gas pressure, interaction geometry and position of the laser focus, the harmonic emission can be phase-matched and confined to just a few harmonic orders. Thus, the harmonic orders of the harmonic beam can be tailored according to the experimental requirements.

2.4.3. Spatial coherence property

The degree of spatial coherence is determined by performing a Young's double slit experiment, in which the coherence property of the source is given by the visibility of the fringes on the interferogram recorded by the CCD:

$$v = \frac{I_{max} - I_{min}}{I_{max} + I_{min}} \tag{2.28}$$

where I_{max} is the maximum intensity at the centre and I_{min} is the intensity of the first minimum of the interference pattern. The source is perfectly coherent when $v = 1$. If the source consists of a few harmonics, then the degree of coherence is calculated by an average of all harmonics in the spectrum which contribute to the interference pattern.

The Young's double slit (YDS) consists of two parallel 4 µm-width, 100 µm-height slits spaced by 20 µm. The YDS is placed before the spectrometer and the interference pattern is recorded by the CCD, in which the fringes are displayed in the y-direction while the harmonic orders are displayed in the x-direction. The YDS is illuminated by a few harmonic source, which is optimized around the 27th order (30 nm). Its interferogram is shown in Figure 2.23.

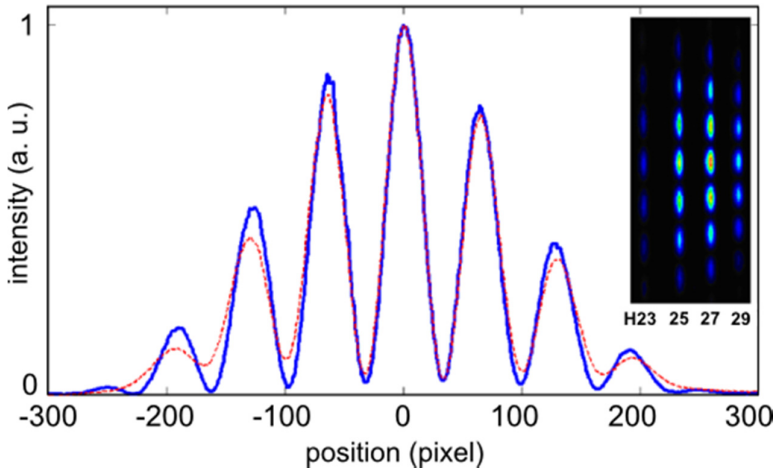

Figure 2.23: Interference fringes of H27 (blue) and of all harmonics (red). The interferogram with the harmonic orders is shown in the inset.

As can be seen, the high contrast of the fringes indicates a high degree of spatial coherence of the source. At the 27th harmonic, the degree of coherence is calculated to be 0.97. This degree of spatial coherence is sufficiently high for use in the

coherent diffractive imaging experiment. In practice, it is impossible to reconstruct an image with a degree of coherence lower than 0.5 [118], typically a good image can only be reconstructed with a coherent degree higher than 0.9.

2.5. Cut-off extension of high harmonic generation using infrared driving laser

2.5.1. Introduction

As mentioned in section 2.2, the maximum HHG energy of a single atom that can be achieved is given by: $\mathcal{E}_{max} = I_p + 3.17\, U_p$, where the ponderomotive energy $U_p \propto I\lambda^2$, i.e., the cut-off depends on the laser intensity and the square of the laser wavelength. To effectively generate high harmonic radiation, the ionization fraction must be kept lower than a critical level, which is sensitive to the laser intensity. Therefore, simply increasing the laser intensity will not increase the HHG efficiency, since the phase-matching condition is broken when the ionization rate exceeds the critical value. On the other hand, the λ^2 dependence of the cut-off energy has motivated the development of HHG systems using an infrared driving laser [66][68][92]. The dependence of the photon energy on the driving laser wavelength is shown in Figure 2.23, which indicates a significant increase of the HHG energy with longer wavelengths [93]. As can be seen, the water window region (280 – 540 eV) can be generated in helium using a wavelength around 1400 nm, and even 1 keV is possible with longer wavelengths [28]. In this section, the generation of high harmonics in the water window region using a 1300 nm wavelength driving laser with helium is reported.

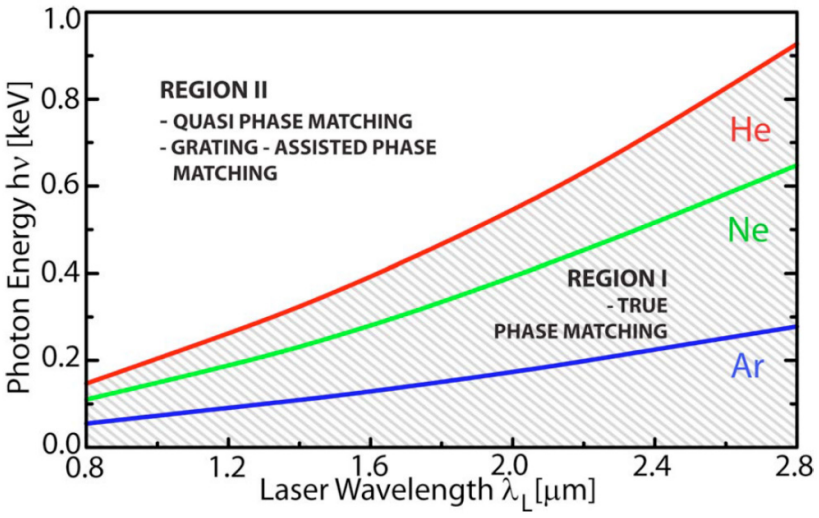

Figure 2.23: Dependence of the cutoff energy with the driving laser wavelength; figure taken from [93].

2.5.2. Experimental setup

To generate a laser in the infrared range, an optical parametric amplification (OPA) system using Bismuth Triborate (BIBO) crystal is employed, as shown in Figure 2.24:

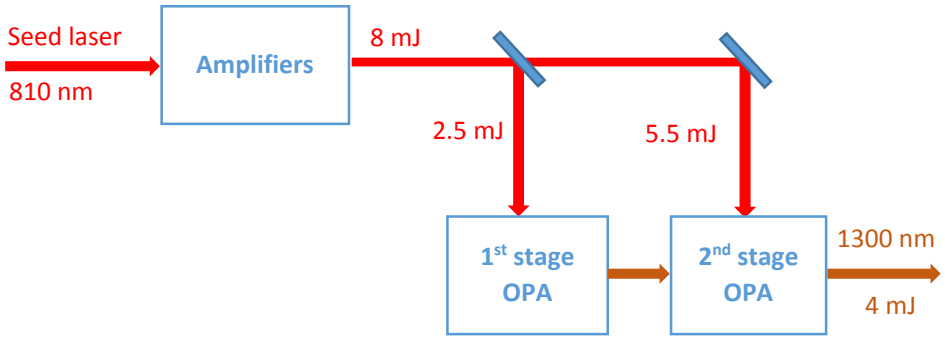

Figure 2.24: Experimental setup of the generation of infrared laser using OPA.

In this experiment, the output of the two-stage amplified laser system (8 mJ pulse energy, 810 nm wavelength and 1 kHz repetition rate) is split to power the OPA and the power amplifier stage. Only 2.5 mJ of the 810 nm laser is fed to the OPA, which is a two-stage configuration and seeded by a white light continuum. The remaining 5.5 mJ is used to pump the amplifier stage, in which a 2 mm thick type II crystal with $\theta = 42^0$ in the x-z principal plane is used and seeded by the commercial OPA output. The resulting output is a 1300 nm laser with 4 mJ energy and the pulse duration is about 40 fs.

The same HHG experimental setup as described in section 2.3 is used, and helium with a pressure up to 5000 Torr is the gas target. The HHG beam is filtered by 300 nm thick aluminum and 300 nm thick silver foils to block the fundamental laser beam. The resultant beam is recorded by the spectrometer with a 1200 groves/mm grating, which is placed downstream from the vacuum chamber.

2.5.3. The XUV radiation in the water window region

The HHG spectra generated with different gas cell pressures are shown in Figure 2.25, in which a 20 s exposure time is used for each spectrum. At low pressures ($<$ 2 atm), the HHG intensity is very weak and the beam is strongly diverged. The intensity is significantly increased around 5 nm and the beam profile is improved when the pressure is increased above 3 atm. The highest photon flux is observed with the pressure at 5 atm, at which a spectrum in the water window region ($<$4.4 nm) is clearly seen.

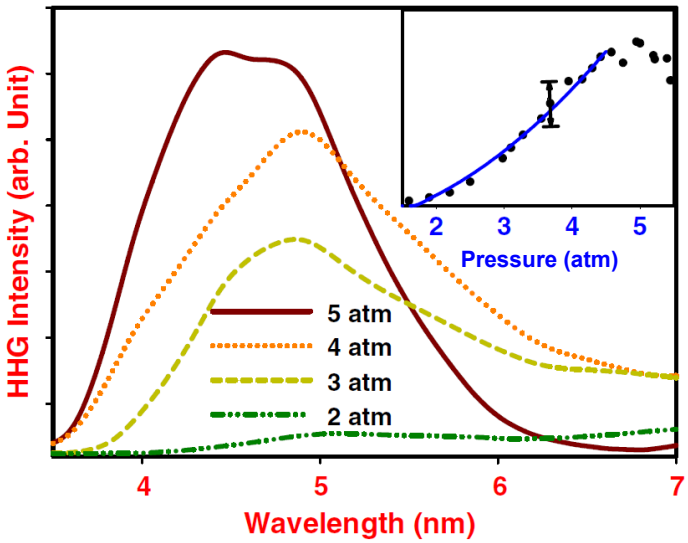

Figure 2.25: HHG spectrum with different gas cell pressures. Inset: experimental data (dots) and P^2 fit (blue line) of the HHG intensities.

To verify the phase matching condition in the experiment, the dependence of the total HHG intensity on pressure is investigated. The inset shows the response of the high harmonic intensity versus increasing pressure, which can be well fitted with a quadratic function. We recall that in the equation for the harmonic intensity (2.6), when the phase is matched $\Delta k = 0$ ($L_{coh} \rightarrow \infty$), the harmonic intensity $I_q \propto P^2$, where P is the pressure, can be proven in this case. With a higher pressure ($>$ 5 atm), the harmonic intensity decreases due to the strong absorption of the medium.

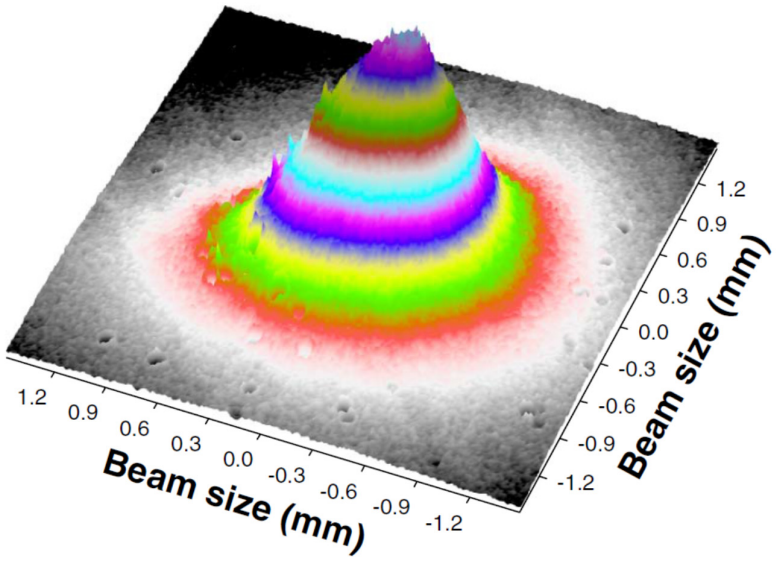

Figure 2.26: XUV HHG beam profile generated in helium at 5 atm.

The highly collimated and good spatial profile characteristics of the HHG radiation is confirmed by a beam profile, as shown in Figure 2.26, which is recorded at a distance 1.8 m from the gas cell. The beam diameter is measured as 0.8 mm (FWHM) and the good Gaussian shape indicates that the short trajectories dominate in the HHG process. The phase-matched high harmonic radiation in the water window region by using the infrared laser generated by the high power OPA system with BIBO crystal is successfully demonstrated.

2.6. Studying the Cooper minimum with two-colour laser fields

2.6.1. Introduction

The theory of high harmonic generation consists of macroscopic and microscopic aspects. The macroscopic aspect includes the phase-matching condition of the harmonics with the driving field and the dependence of the harmonic spectrum and degree of coherence on the experimental parameters, which have been discussed already. On the other hand, the microscopic aspect is the single-atom response, where the high harmonic generation process can be described by the three-step model, in which the tunneling and recombination processes of the electrons can be analyzed to study the atomic and molecular dynamics [94][95].

High harmonic generation has been widely favoured as a tool for studying the structure of atoms and molecules, because of the ability to produce short wavelength light with ultrashort pulse duration [36][38]. One interesting phenomenon is the Cooper minimum, which is the minimum intensity of the high harmonic spectrum and remains independent of the driving laser intensity and wavelength [96][97][98]. In fact, this minimum relies solely on the internal structure of the atoms and molecules; hence the information of the electrons' orbitals and dynamics can be studied by analyzing the Cooper minimum in the HHG spectrum. The Cooper minimum of argon has been found to be around 50 eV [97] and krypton is 90 eV [99]. This minimum occurs in the photoionization when one transition dipole moment changes sign when the others are small. Thus the minimum in the spectrum originates from the zero matrix element between the d and s continuum waves and the $3p$ ground state. Since photoionization is the inverse of the recombination matrix element, which is one stage of the three-step model of the HHG process, the Cooper minimum is also related to the high

harmonic emission of a single atom. However, to fully understand the HHG process, propagation and absorption effects need to be taken into account, which is the phase-matching condition described in section 2.2. Therefore, the appearance of the Cooper minimum is also affected by the phase-matching condition [100]. In this section, the phase-matching condition is modified by adding a weak 800 nm field to the 1400 nm driving laser field. By delaying the 800 nm field, the temporal overlapping between the two fields and thus the atomic dipole phase can be controlled in the HHG process, so that the visibility of the Cooper minimum can be enhanced.

2.6.2. Experimental setup and results

The experimental setup for the two-colour laser field high harmonic generation is shown in Figure 2.27. A 1.6 mJ, 1400 nm laser beam from the OPA, which was described in section 2.5.2, is used to generate the harmonic, whereas the weaker 0.4 mJ, 800 nm laser beam is used as the control field as the intensity is too weak to ionize the gas. Two laser fields are collinearly focused into an argon gas cell, in which the focus position is placed near the exit hole of the gas cell. In addition, the 800 nm laser beam is guided through a motorized delay stage with a step resolution of 25 nm.

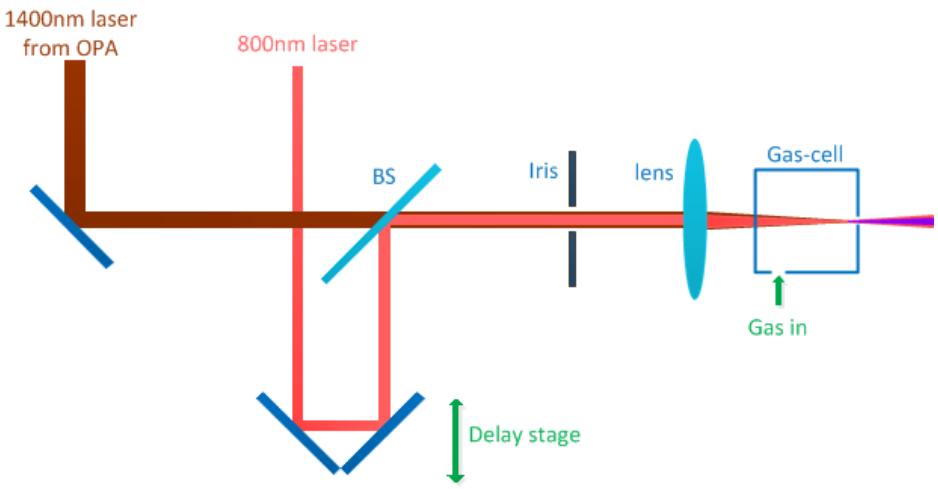

Figure 2.27: The two-colour laser field experiment setup.

At first, the delay is set to -350 fs, where the 800 nm field is completely in front of the IR field to ensure there is no contribution of the 800 nm field to the high harmonic generation process. The harmonic beam is optimized at a pressure of 250 Torr; in addition, spectra of the harmonic signal are also recorded at 150 Torr and 350 Torr, as shown in Figure 2.28. As clearly seen, in the phase-matched spectrum at 250 Torr, the Cooper minimum is visible at around 52 eV, which is consistent with previous studies. The excellent Gaussian-fitted beam profile of the harmonic beam indicates that a high spatial coherence is achieved, which originates from the dominance of the short electron trajectory in the generation process. At the other pressures, the shape of the spectrum is dramatically changed and the Cooper minimum is very hard to observe. Therefore, the visibility of the Cooper minimum is strongly dependent on the phase-matching condition of the harmonic generation process.

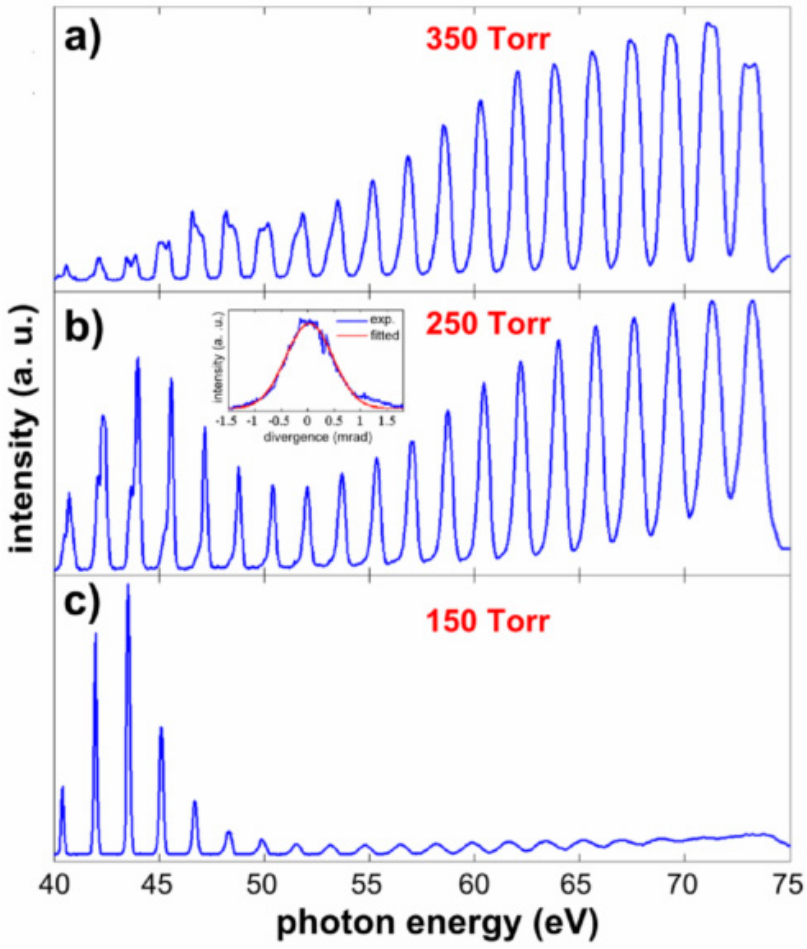

Figure 2.28: HHG spectrum with different gas cell pressures at 350, 250 and 150 Torr. The beam profile and its fitting of the harmonic beam is shown in the inset at 250 Torr.

The phase-matching condition is now modified by adding the 800 nm field, which results in a change of the dipole phase-matching term. The delay stage is set to -30, 0 and +30 fs relative delay between the two fields, where a positive delay means the IR field precedes the 800 nm field and zero delay means the two pulses are temporally overlapped. The weak field cannot generate harmonics by itself, but in fact modifies the electron trajectories excited by the IR field. Therefore, different harmonic spectra and harmonic beam profiles are observed, as shown in Figure 2.29.

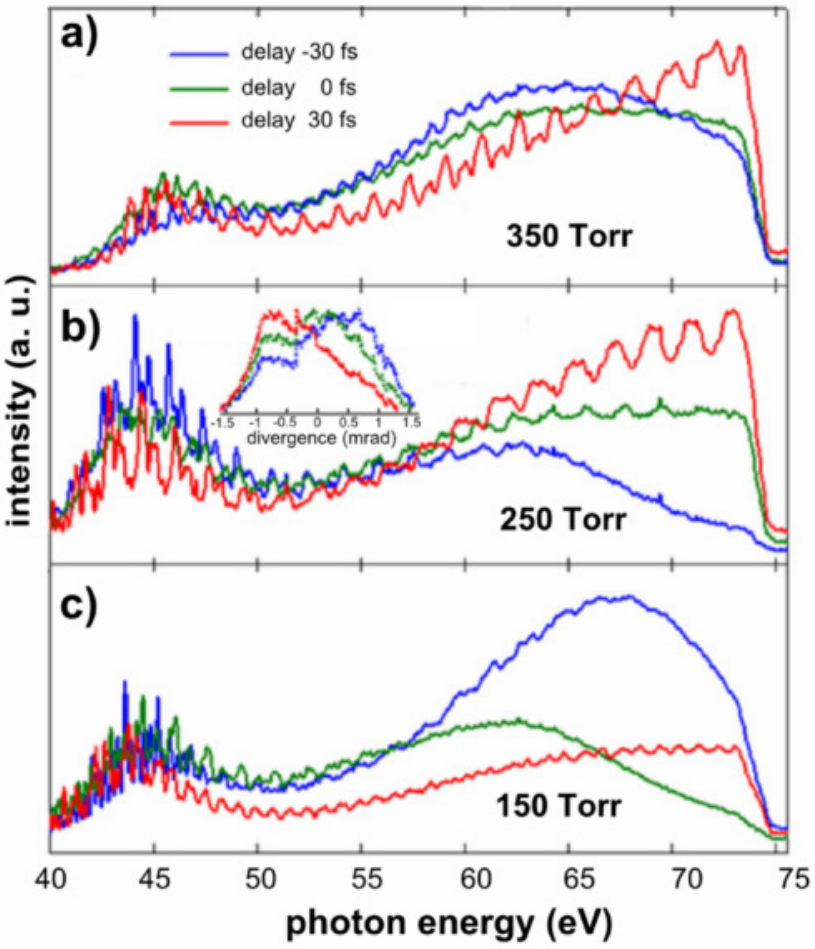

Figure 2.29: HHG spectrum with two-colour laser fields at different delay and different gas cell pressures at 350, 250 and 150 Torr. The beam profile of the harmonic beam is shown in the inset at 250 Torr.

By adding the weak 800 nm field, the shapes of the spectra are completely changed (compared to the IR field alone), in which even harmonics and a continuum spectrum are observed. This is due to the fact that the symmetry of the driving laser field is broken and the electron trajectories are highly modified by the external field. In addition, the Cooper minimum is easier to observe in all cases. As expected, although the spectrum shapes are changed with various delay and pressure values, the Cooper minimum almost remains at the same value, around

52 eV as in previously found, which indicates the minimum value is independent of the phase-matching condition. The beam profile of the harmonic beam is also shown in the inset of Figure 2.28 b), where distortion of the beam profile is observed. This is due to interference of the electron trajectories by the modification of the driving electric field. By changing the time delay between the two laser fields, the electric field of the driving laser is modified differently, which results in different dipole phase mismatches as well as the high harmonic spectrum.

As a conclusion, by adding a weak 800 nm field to the 1400 nm driving laser field, the appearance of the Cooper minimum in the generated harmonic spectrum can be enhanced. By changing the phase-matching condition with different gas pressure and delay between the two fields, the harmonic intensities on both sides of the Cooper minimum can be changed to improve the visibility, which is desirable for studying atomic structures.

Chapter 3

Theory of Coherent Diffractive Imaging

3.1. Introduction

Since the first demonstration by J. Miao in 1999 [17], Coherent Diffractive Imaging (CDI) has been widely developed to study nanostructures, such as nanocrystals and biological samples. With the ability to provide a high resolution image on the nanometre scale without the need for an optical lens, CDI has found vast potential in many disciplines since this method overcomes the manufacturing limit of x-ray optics. Recently, CDI experiments have been successfully demonstrated using synchrotron sources [19][21][101][26], x-ray free electron lasers [20][102][103], soft x-ray lasers [104][105][106] and high harmonic generation [39][40][25]. A general CDI experiment is shown in Figure 3.1, where the sample is illuminated by a coherent light source and the diffracted intensities are recorded by a far-field detector. Based on diffraction theory, the image of the sample can be reconstructed from the diffraction data by a phase retrieval algorithm.

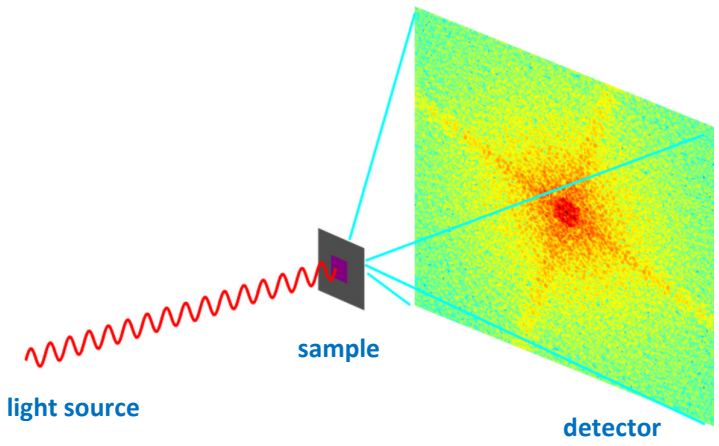

Figure 3.1: The general CDI experiment geometry.

The CDI technique is extremely useful for imaging the internal structures of biological samples, compared to electron microscopy, since x-rays have a much greater penetration depth than electrons. Especially in the "water window" region (280 – 540 eV), CDI has the great advantage of obtaining high contrast images of a sample from the different K-absorption edges of carbon and oxygen atoms, as shown in Figure 3.2. Furthermore, a biological sample can be imaged under wet conditions rather than in the dried form, which opens the possibility of live-cell imaging.

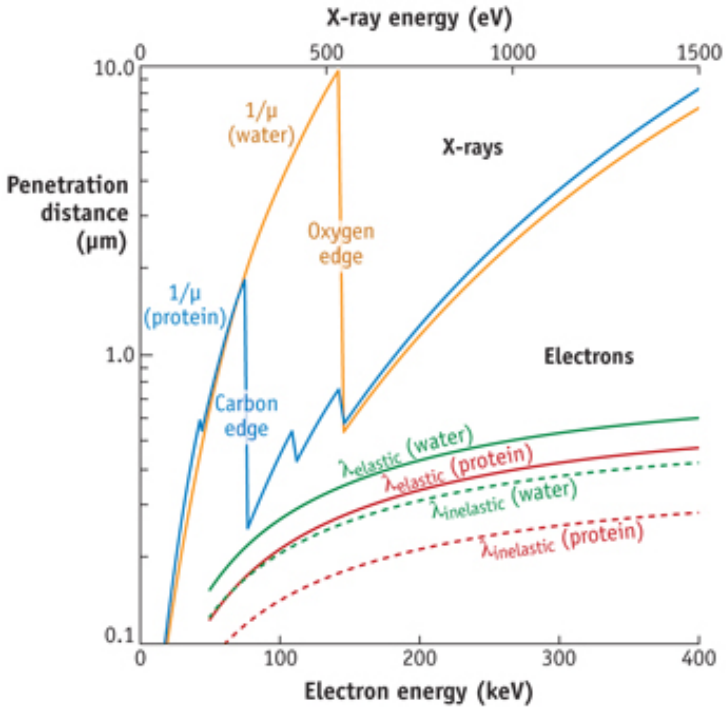

Figure 3.2: Penetration depth of x-rays and electrons in protein and water molecules. The "water window" is formed by the different absorption edges of carbon (mainly in protein) and oxygen (mainly in water)[107].

In this chapter, some background and theory of CDI is described, including the diffraction theory, the oversampling technique, the phase retrieval algorithm and the experimental requirements. The limitations and some strategies to increase the resolution are also discussed.

3.2. Diffraction theory

Diffraction is one of the most interesting phenomena of light and has been intensively studied using the wave theory by scientists since the 17th century [108][109], and a more definitive study was described by Fresnel in 1815 [110]. In this theory, the diffracted electric field of a sample illuminated by a coherent plane wave at a distance screen is approximated by:

$$E_i(x,y,z) = \frac{\exp(ikz)}{i\lambda z} \iint_{-\infty}^{\infty} E_0 \exp\left(\frac{ik}{2z}[(x_i - x_0)^2 + (y_i - y_0)^2]\right) dx_0 dy_0 \quad (3.1)$$

where E_0, x_0, y_0 and E_i, x_i, y_i are the electric fields and coordinates in the sample plane and detector plane, z is the propagation coordinate (z = 0 at the sample plane) and $k = 2\pi/\lambda$ is the wave vector. As E_0 is the electric field after propagating through the sample, it can be also referred to as the "exit surface wave field", which contains information on the structure of the sample.

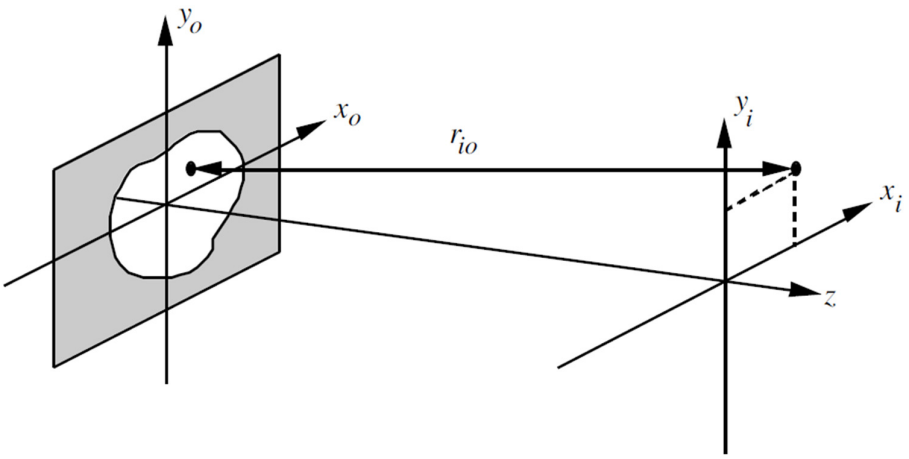

Figure 3.3: General CDI geometry, where $(x_0,\ y_0)$ represents the sample plane and $(x_i,\ y_i)$ represents the detector plane. The illuminating source propagates in the positive z direction.

This approximation is valid as long as the size of the sample (D) and the distance between the sample and detector (d) are much larger than the wavelength of the light (D, d $\gg \lambda$).

The exponential term in equation (3.1) can be expressed as:

$$\exp\left(\frac{ik}{2z}[(x_i - x_0)^2 + (y_i - y_0)^2]\right) = \exp\left[\frac{ik}{2z}(x_i^2 + y_i^2)\right]\exp\left[\frac{ik}{2z}(x_0^2 + y_0^2)\right]\exp\left[-\frac{ik}{2z}(x_i x_0 + y_i y_0)\right] \quad (3.2)$$

and hence equation (3.1) is re-written as:

$$E_i(x,y,z) = \frac{\exp(ikz)}{i\lambda z}\exp\left[\frac{ik}{2z}\left(x_i^2 + y_i^2\right)\right]\iint_{-\infty}^{\infty} E_0 \exp\left[\frac{ik}{2z}\left(x_0^2 + y_0^2\right)\right]\exp\left[-\frac{i2\pi}{\lambda z}\left(x_i x_0 + y_i y_0\right)\right]dx_0 dy_0 \quad (3.3)$$

As can be seen, the integration is similar to a Fourier transform operation, and the equation can be expressed in terms of the Fourier transform operator $\mathcal{F}$:

$$E_i(x,y,z) = \frac{\exp(ikz)}{i\lambda z}\exp\left[\frac{ik}{2z}\left(x_i^2 + y_i^2\right)\right]\mathcal{F}\left\{E_0 \exp\left[\frac{ik}{2z}(x_0^2 + y_0^2)\right]\right\} \quad (3.4)$$

If the distance z is much larger than the size of the sample ($z \gg k(x_{0max}^2 + y_{0max}^2)/2$), and hence $exp\left[\frac{ik}{2z}\left(x_0^2 + y_0^2\right)\right] \approx 1$, the diffraction equation can be simplified to a far-field Fraunhofer approximation:

$$E_i(x,y,z) \simeq \frac{\exp(ikz)}{i\lambda z}\exp\left[\frac{ik}{2z}\left(x_i^2 + y_i^2\right)\right]\mathcal{F}\{E_0\} \quad (3.5)$$

As a result, the diffracted field at the detector can be approximated as a two dimensional Fourier transform of the exit surface wave field at the sample plane. This is the principle of coherent diffractive imaging, where the simulation and reconstruction processes can be implemented using a Fast Fourier Transform

(FFT) operator. The spatial frequencies of the diffraction at the detector are given by [111]:

$$\Delta k_x = \frac{x_i}{\lambda z} \qquad \text{and} \qquad \Delta k_y = \frac{y_i}{\lambda z} \tag{3.6}$$

As long as the Fraunhofer approximation is valid, increasing the distance z will result in scaling-up the diffraction without changing the patterns. A similar observation can be seen when varying the wavelength of the source, as the shorter wavelength tends to compress and the longer one tends to expand the diffraction pattern.

3.3. Oversampling requirement

As stated in equation (3.5), the diffraction field at the detector plane is the Fourier transform of the exit surface wave at the sample plane. Therefore, one can use the inverse Fourier transform to obtain a "shadow" (and hence the structure) of the sample if the diffraction field is measured. However, only the intensity of the diffraction field can be recorded by the detector (usually a CCD camera):

$$I(x_i, y_i) = |E_i(x_i, y_i)|^2 \tag{3.7}$$

Since all the phase information is lost, it is not possible to recover the structure of the sample directly using an inverse Fourier transform operator. In 1952, Sayre [112] suggested that the phase information can be recovered if the diffracted intensity is sampled at a sufficient rate. According to the Nyquist sampling theorem, the diffraction data must be sampled at a higher rate than the spatial Nyquist frequency; this is called oversampling. In this case, the number of unknowns (phase) is less than the number of known variables (magnitude). An

oversampling ratio, σ, has been introduced by Miao [23] to determine how many known pixels are enough to recover the phase information:

$$\sigma = \frac{total\ pixel\ number}{unknown\ pixel\ number} \tag{3.8}$$

To satisfy the oversampling requirement, i.e., $\sigma > 2$, the number of known pixels can be increased by padding zero-value pixels surrounding the object, or isolating the object in a big enough empty space. A region in which the object is non-zero is called the support, and clearly the size of the support must be less than half of the total detector size in each dimension. The support is also referred to as *a priori* in the reconstruction algorithm, which is described later in this chapter.

3.4. Phase retrieval algorithm

The first idea of a phase retrieval algorithm was proposed by Gerchberg and Saxton [113] and later improved by Fienup, with an Error Reduction (ER) and Hybrid Input Output (HIO) algorithms [114][22]. The principle of the phase retrieval algorithm is shown in Figure 3.4:

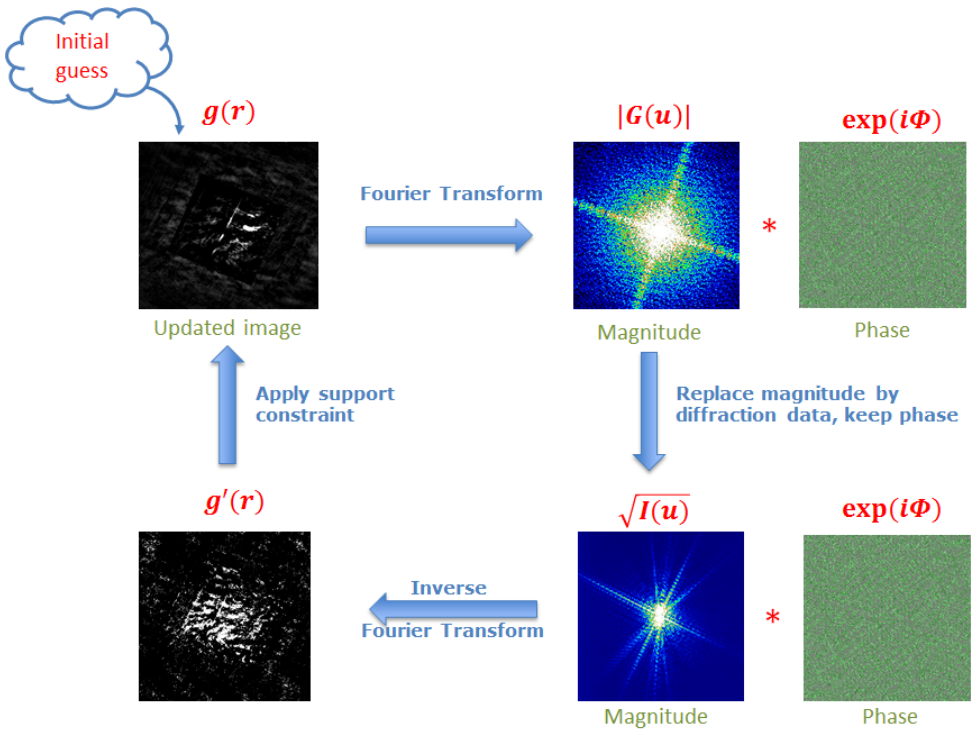

Figure 3.4: The iterative phase retrieval algorithm.

Generally, the phase retrieval algorithm consists of four basic steps:

1) The sample's image is initialized with a random guess, or a support image as *a priori* information: *g(r)*.
2) The magnitude and phase at the detector plane is calculated by taking a Fourier transform of the initialized sample image as described by equation (3.5), which can be performed easily using a FFT operator in the computer:

$$G(u) = \mathcal{F}\{g(r)\} = |G(u)| \exp(i\Phi) \qquad (3.9)$$

3) The magnitude $|G(u)|$ is replaced by the Fourier modulus (square root of the diffraction intensity recorded by the detector $I(u)$). Then the new sample's image in real space is calculated by taking an inverse Fourier transform of the updated $G(u)$:

$$g'(r) = \mathcal{F}^{-1}\left\{\sqrt{I(u)}\exp(i\Phi)\right\} \tag{3.10}$$

4) A support constraint is applied to the image from step 3 to obtain the updated sample's image, including the ER and HIO algorithms.

The ER is the basic algorithm which is based on the assumption that the object is of finite size and isolated in empty space. A support constraint S is chosen to be the approximate size of the object, and in each ER iteration the new image is updated by:

$$g_{k+1}(r) = \begin{cases} g'_k(r) & if\ r \in S \\ 0 & if\ r \notin S \end{cases} \tag{3.11}$$

In short, the ER operation sets all the intensities outside the support to zero while it keeps the intensities which are inside. To achieve a good result and a fast convergence, a tight support is required which is very close to the size of the object. Although ER helps to clean up the noise around the object, the operation may stagnate at a local minimum and prevent further converging.

On the other hand, the HIO operation overcomes the problem of stagnating at a local minimum by introducing feedback of the previous reconstructed image to the current image. This operation can be expressed as:

$$g_{k+1}(r) = \begin{cases} g'_k(r) & if\ r \in S \\ g'_k(r) - \beta g_k(r) & if\ r \notin S \end{cases} \tag{3.12}$$

The feedback parameter β is chosen to be around 0.9, and in a special case when $\beta = 1$ the HIO operation reduces to the ER operation as described. By allowing non-zero amplitudes outside the support, the HIO algorithm helps to escape the local minima when the ER cannot find any solution. Therefore, combining HIO and ER is an effective method in the phase retrieval process, where the HIO

operation ensures finding a solution and the ER helps to clean up the noise around the object afterwards.

The phase retrieval process is repeated again from step 2 for a finite number of iterations until the quality of the updated sample's image satisfies the requirement. During the reconstruction process, an error metric can be estimated by calculating the differences between the measured intensity and the reconstructed intensity of the diffraction:

$$\chi^2 = \frac{\left(\sqrt{I(u)} - \sqrt{|G(u)|}\right)^2}{|G(u)|} \tag{3.13}$$

This error metric is useful since the performance of the reconstruction can be evaluated and the combination of the HIO and ER can be optimized to increase the speed and the quality of the reconstructed image. A standard "recipe" for a normal reconstruction consists of alternate groups of hundreds of ER iterations followed by ~100 HIO iterations and the final image is cleaned up by the ER operation.

Although the combination of the HIO and ER algorithms has proven to effectively reconstruct the sample's image from its diffraction pattern, a knowledge of the support size is required before reconstruction. This size can be retrieved from the speckle of the diffraction pattern, or from the autocorrelation of the diffracted intensities, which is based on the fact that the autocorrelation size is exactly twice the size of the object. However, a tight support helps the reconstruction process to converge faster and a good approximate support can be constructed after a few HIO iterations at the start of the reconstruction, where a rough estimated shape of the object begins to form. Another method, the so-called "shrink-wrap algorithm", has been developed to eliminate the need for prior knowledge of the sample's size and the support is determined and updated during the

reconstruction process [115]. In this method, an initial support is derived from the diffraction pattern's autocorrelation or from an arbitrary shape. After 50 - 100 iterations, a new support is calculated by filtering the reconstructed image with a Gaussian filter and then thresholding the consequent image. The threshold is chosen between 10% - 20% of the maximum intensity and the standard deviation width of the Gaussian filter is deceased throughout the reconstruction as the shrink-wrap algorithm tends to enlarge the object. On the other hand, this method does not work well with smooth edge objects since the support is tighter and thresholding removes the low intensity part of the object.

3.5. Experimental requirements of CDI

In order to achieve a high quality reconstructed image, some crucial requirements of the experiment have to be considered, including the geometric experimental setup (such as the distance between the sample and detector, and the size of the sample and the detector) and the quality of the source (such as the degree of coherence, the brilliance and the source's stability).

3.5.1. The experimental geometry

To satisfy the far-field approximation in equation (3.5), the detector has to be placed at a large distance from the sample, so that the following requirement is met:

$$z \gg \frac{D^2}{\lambda} \tag{3.14}$$

where z is the distance between the sample and detector, D is the sample dimension and λ is the wavelength of the source. For a sample with a maximum dimension of 10 μm illuminated by a 30 nm wavelength source, a reasonable long

distance should be greater than 3 cm (about 10 times D^2/λ). Furthermore, a sufficient oversampling ratio must be satisfied to reconstruct a high resolution image. Recalling equation (3.8), the oversampling requirement also means the sample must be isolated in the middle of a large "black" plane, where there is no transmission of x-rays, to prevent noisy scattering of photons into the detector. Furthermore, the oversampling ratio must satisfy the following relationship:

$$O = \sqrt{\sigma} = \frac{z\lambda}{pD} \geq \sqrt{2} \qquad (3.15)$$

where p is the pixel size of the detector. This requirement can be met by using a detector with a smaller pixel size, or placing the detector further away from the sample.

3.5.2. Requirements of the source

In general, a good CDI experiment requires a high degree of spatial and temporal coherence of the source, since the contrast of the fringes in the diffraction pattern decreases as the degree of coherence degrades. The spatial coherence length (ℓ_s) should be larger than the illuminated size on the sample, as follows:

$$\ell_s \geq O\ D \qquad (3.16)$$

For a temporal coherence length ℓ_t, this requirement is given by [116]:

$$\ell_t = \frac{\lambda^2}{2\Delta\lambda} \geq \frac{OD\lambda}{2r} \qquad (3.17)$$

where $\Delta\lambda$ is the spectral width at the wavelength λ and r is the desired resolution of the reconstructed image. This means that the resolution of the reconstructed image depends strongly on the temporal coherence length of the source and the oversampling ratio of the diffraction pattern. Furthermore, the intensity variation

of the source across the sample should be considered, and the effect of non-uniform illumination can be minimized by using a sufficiently large beam on a small sample. A typical CDI experiment may run for many hours, and hence the stability of the source is crucial to obtain reliable and consistent data; therefore a decrease in the intensity and drift in the beam position should also be monitored and adjusted.

3.5.3. Requirements of the detector

A high resolution image requires sufficient data to be collected at high diffraction angles; however as the intensity drops quickly at higher frequency, the high angle diffraction patterns always suffer background noise and are difficult to capture. To prevent unwanted noise, the CDI detector must be shielded by a completely "black" enclosure to avoid any environment light and a large sample plane is required to prevent scatter of the x-ray beam inside the experiment chamber. Furthermore, the detector should be operated at a low-noise mode (such as deep cooling) to minimize "dark counts" due to thermal noise. A high dynamic range of the detector is also required to sufficiently resolve the patterns at high angle. For a sample in which a larger dynamic range of the diffraction pattern is required, a beam stop can be used to block the high intensity region in the centre of the diffraction pattern and allow the high angle data to be captured. However, special treatment is required to assemble a full diffraction pattern and this method is described in section 5.5.4.

In addition, a detector with a homogenous thermal background is required to produce a smooth diffraction pattern, in which the noise is distributed uniformly across the area of the detector. A sudden change of background level may cause artifacts in the reconstructed image and hence reduce the achieved resolution.

3.6. Resolution

Theoretically, the resolution limit of a CDI experiment is only limited by the wavelength of the illuminating source, which is given by the Rayleigh criterion:

$$r = \frac{0.61\lambda}{NA} = \frac{1.22\ z\ \lambda}{p\ N} \tag{3.18}$$

where p is the pixel size of the detector and N is the dimension of the detector in pixels. However, in practice this resolution limit is dominated by the highest angle diffraction data that can be collected by the detector, which relates to how good is the signal to noise ratio (S/N) of the captured diffraction pattern, how big is the detector size and how large is the dynamic range that can be achieved. A common way to determine the resolution of a reconstructed image is to use the knife-edge method, in which a line profile is recorded across the transition from dark to light at the edge and the resolution is the width of 10% - 90% of maximum intensity. This method works best with a sample which has a sharp edge and the size of the feature is known beforehand; hence this method can be used to quickly estimate the resolution of the experiment using a test object. A more general resolution measurement is to use a phase retrieval transfer function (PRTF), which is defined by [117]:

$$PRTF(q) = \frac{|\mathcal{F}(q)|}{\sqrt{I(q)}} \tag{3.19}$$

where $\mathcal{F}(q)$ is the Fourier transform of the final reconstructed image and $I(q)$ is the measured diffraction intensity. This function is plotted along the spatial coordinate q and the resolution is determined when the PRTF reaches a 1/e (~37%) threshold.

Although synchrotron and free electron laser sources can provide x-ray radiation with sub-nanometre wavelength, the best achieved resolution for a biological sample is still in the sub-10 nanometre range. This limitation is mainly due to damage of the biological molecules under the intense x-ray radiation. By using an ultra-short x-ray pulse (~10 fs), a diffraction pattern can be created before damaging the sample, so called "diffraction before destruction" scheme, which has recently been implemented in CDI experiments using a free electron laser source [102][103].

3.7. Simulation of the effects of experimental aspects on the reconstructed image

To visualize the effects of the different experimental parameters on the image reconstruction process, simple sample images are simulated with different diffraction data size, dynamic range and noise levels. The 'SWIN' sample and spheres sample with their diffraction patterns are shown in Figure 3.5. The images and the data sizes are 1024×1024 pixels, in which the diffraction pattern is displayed on a log scale with a ~10 orders of magnitude dynamic range. The spheres sample consists of a large square of transmission area and some spheres with different diameters, which simulates a real-world CDI experiment with a biological-like object deposited on a transmission membrane.

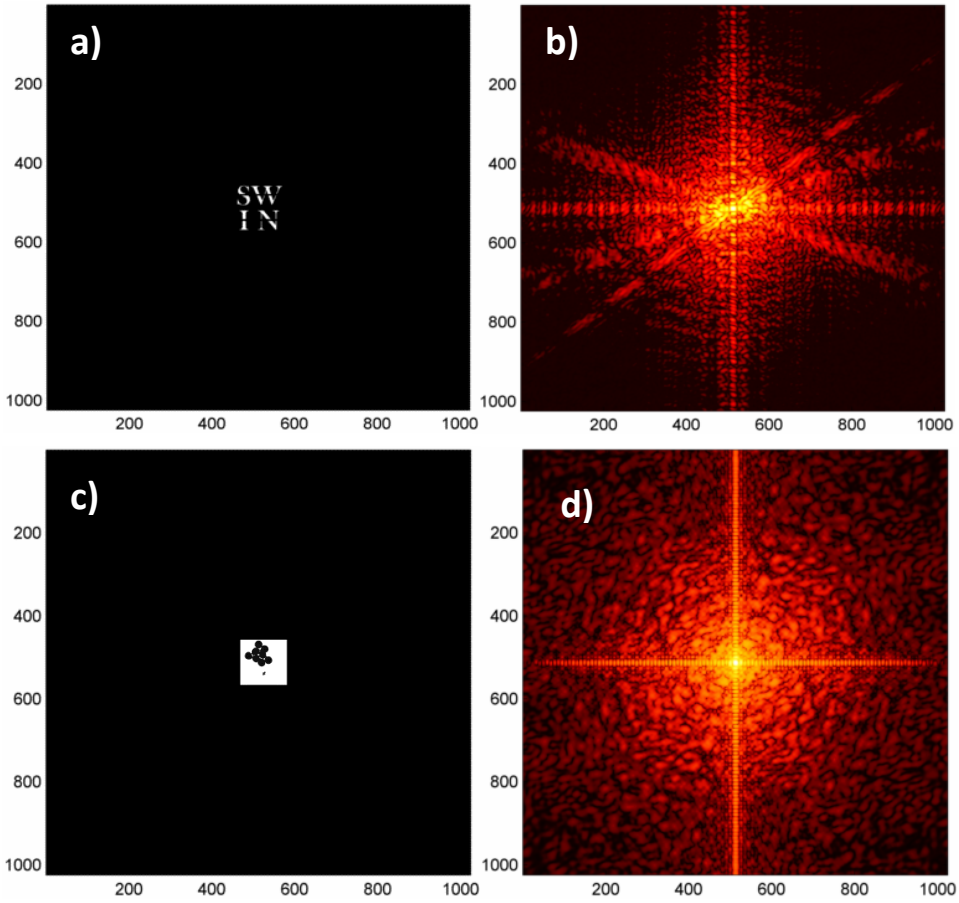

Figure 3.5: SWIN sample (a) and its simulated diffraction pattern (b). Spheres sample (c) and its simulated diffraction pattern (d).

If the diffraction patterns with a 16-bit dynamic range (~4.5 orders of magnitude) are cropped at 50%, i.e., if the high angle data is missing, the effect on the reconstruction is shown in Figure 3.6. The reconstruction is performed for 1500 iterations as described in section 3.4. The reconstructed images are enlarged to reveal the details of the letters in the SWIN sample (3.6 b) and spheres inside the square (3.6 e), where the resolutions (10% - 90% knife edge test) are 4 pixels and 5 pixels. The resolution is reduced as expected.

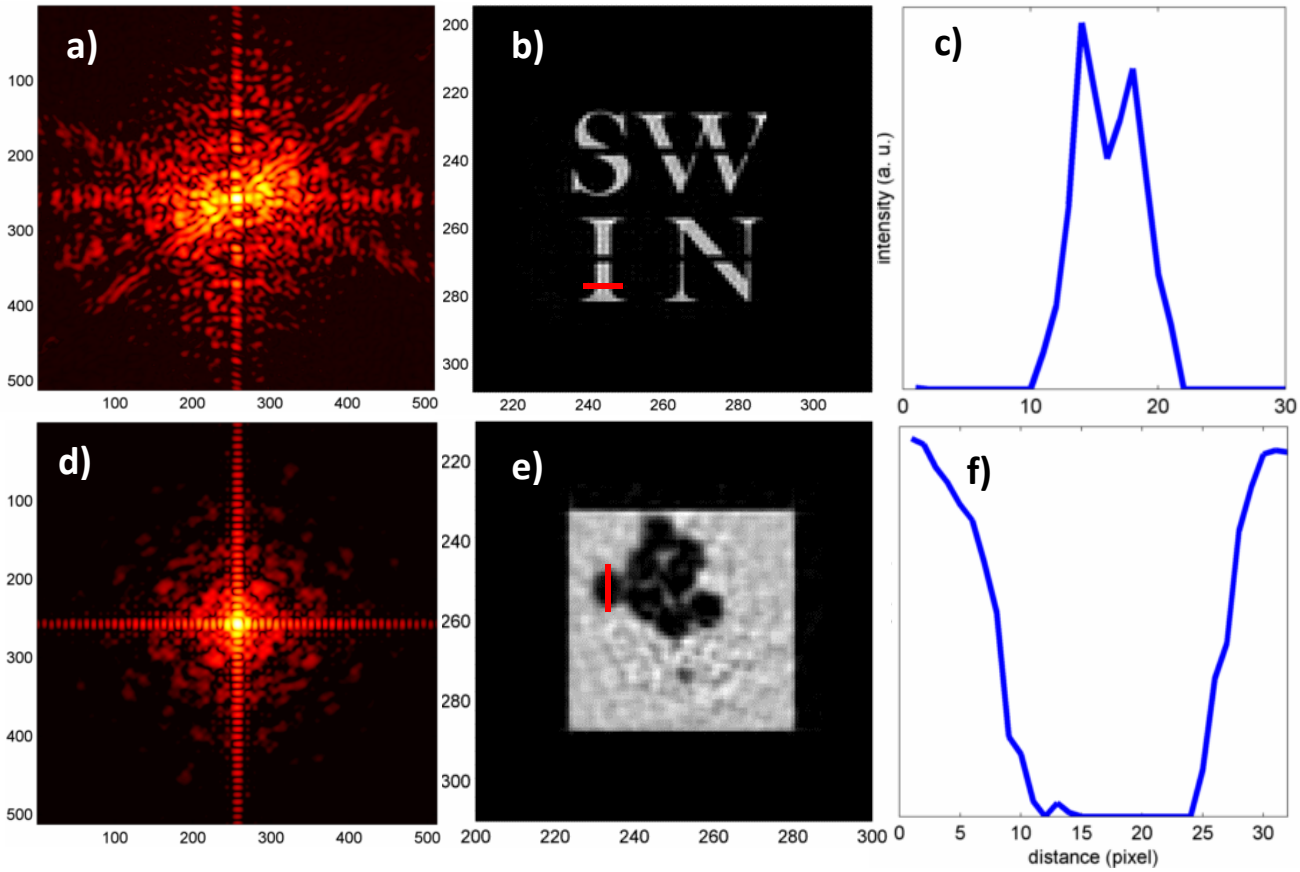

Figure 3.6: Cropped diffraction pattern (a) and its reconstructed image (b) of the SWIN sample, where the cut-out profile of the red line is shown in (c). Similar diffraction pattern, reconstructed image and cut-out profile of the spheres sample are shown in (d), (e) and (f).

The other parameter that affects the reconstruction performance is the dynamic range of the diffraction pattern. By scaling the diffraction pattern and then thresholding to a typical noise level, the missing high angle problem due to the limitation of the detector can be simulated. Figure 3.7 shows the diffraction patterns of the SWIN sample with a 16-bit and 10-bit dynamic range, which corresponds to 4.5 and 3 orders of magnitude, respectively.

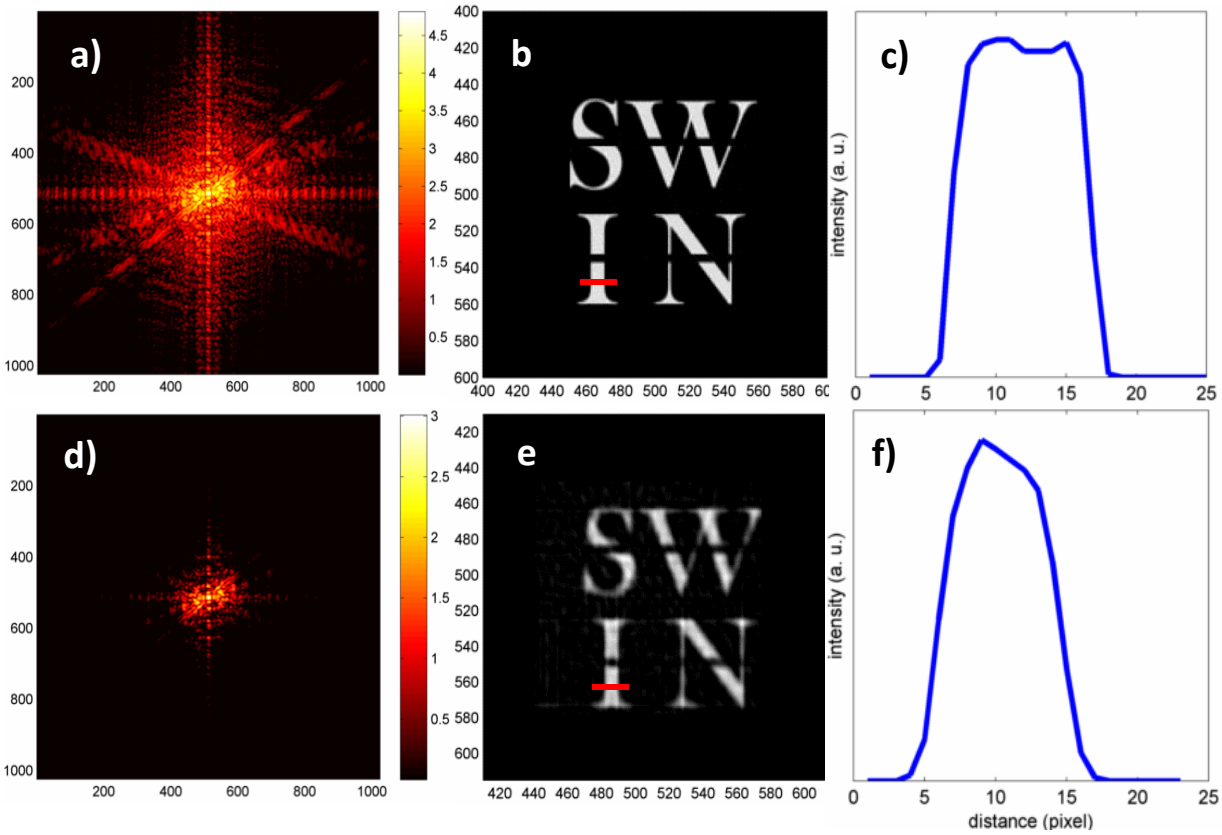

Figure 3.7: SWIN diffraction patterns with 4.5 (a) and 3 (d) orders of magnitude dynamic range with their respective reconstructed images (b) and (e). The knife-edge profiles of the red lines are shown in (c) and (f).

As shown in Figure 3.7 b) the diffraction with 4.5 orders of magnitude (16-bit similar to the CCD dynamic range) is sufficient to reconstruct a good SWIN image with the resolution of 2 pixels. When the high angle data is missing, the reconstructed image is more blurry and hence the resolution is decreased to 4 pixels, as shown in Figure 3.7 e).

On the other hand, it is more difficult to reconstruct a good spheres image from a 16-bit diffraction pattern, as shown in Figure 3.8 b). Since the intensity of the diffraction pattern is dominated by the large transmission square, the diffraction due to the spheres is very limited and hence most of the high angle data is lost.

Therefore, the reconstructed image is very blurry and the spheres are hardly recognized with the resolution is about 14 pixels.

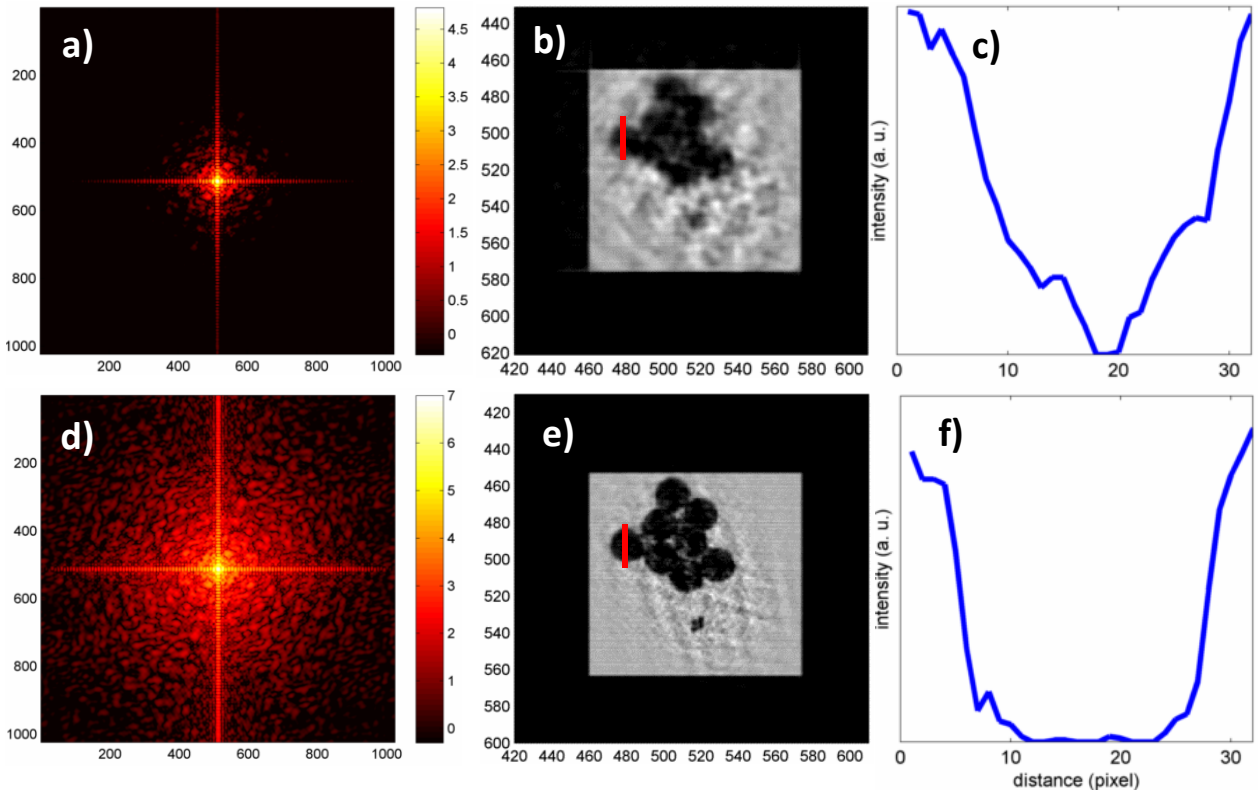

Figure 3.8: Spheres sample diffraction patterns at 4.5 (a) and 7 (d) orders of magnitude dynamic range with their respective reconstructed images (b) and (e). The knife-edge profiles of the red lines are shown in (c) and (f).

When the diffraction pattern is scaled to 7 orders of magnitude (Figure 3.8 d), more high-angle data created by the spheres can be seen and as a result, a better image with finer detail is reconstructed (Figure 3.8 e) and the resolution is now about 5 pixels. In practice, this high dynamic range can only be achieved by using a beam stop to block the centre region, which allows the high-angle data to be collected and then the final diffraction pattern is combined from the low-

angle and high-angle data. Only a single diffraction pattern captured by the CCD is not enough to reconstruct a good image of this kind of sample.

The next simulation is to investigate the effects of noise on the reconstructed images. A random noise is added to the 16-bit (4.5 orders of magnitude) SWIN diffraction pattern before the reconstruction is performed, in which the maximum amplitude is 10 and 30, corresponding to a S/N ratio of 76 dB and 66 dB, respectively. The reconstructed images are shown in Figure 3.9:

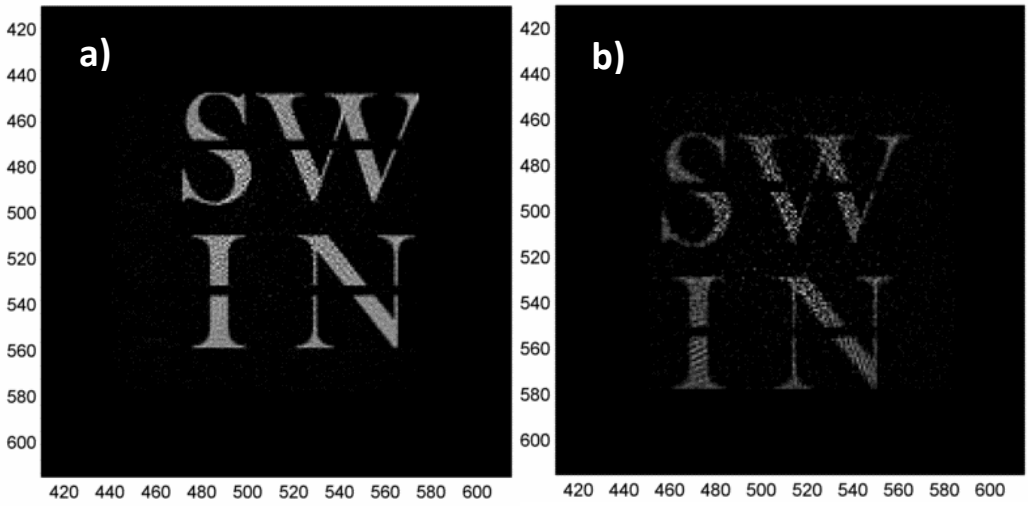

Figure 3.9: Reconstructed images from the SWIN diffraction pattern with a S/N of 76 dB (a) and 66 dB (b).

For the sphere sample, a noise level of 10 and 50 is added to a 7 orders of magnitude diffraction pattern, which yields a S/N of 120 dB and 106 dB, respectively. The reconstructed images are shown in Figure 3.10.

As expected, the diffraction pattern which has a higher signal to noise ratio produces a smoother reconstructed image. A higher S/N ratio is required for the reconstruction of the spheres sample which is at least 120 dB to produce a good image, while the SWIN sample only needs around 76 dB. From these simulations,

the crucial requirement to achieve a high quality image is to ensure not only sufficient high angle data, but also a high value of the signal to noise ratio.

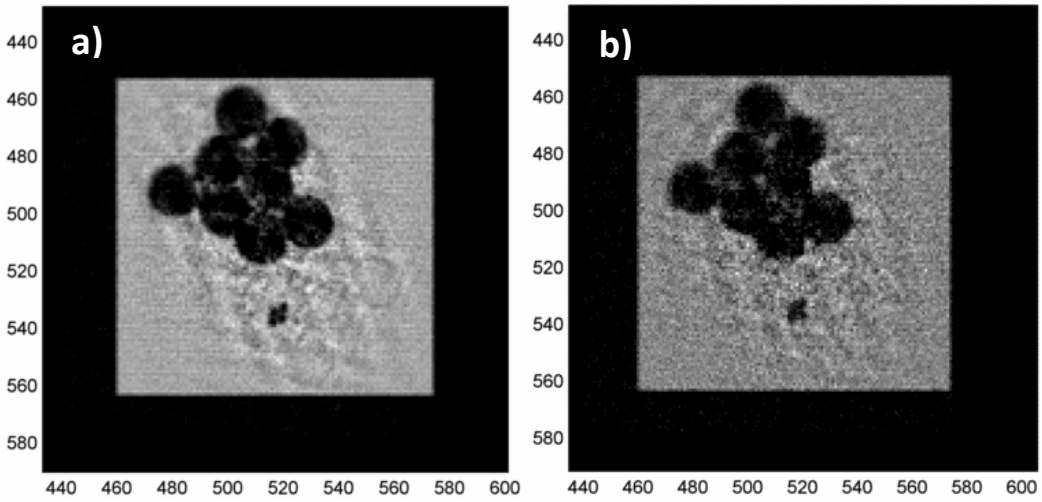

Figure 3.10: Reconstructed images from the spheres diffraction pattern with a S/N of 120 dB (a) and 106 dB (b).

3.8. Conclusions

The history and relevant theory of coherent diffractive imaging have been investigated, including diffraction and sampling theory. By using a Fourier transform operator, the relationship between the diffraction pattern and the "shadow" image of the sample can be described. Since only the magnitude of the Fourier transform can be recorded, an iterative phase retrieval algorithm must be employed to recover the structure of the sample. In order to obtain a high resolution reconstructed image, several experimental requirements need to be satisfied, such as the quality of the source, the geometrical setup and the oversampling ratio. In the following chapter, more details of the CDI experiment using high harmonic generation are presented.

Chapter 4

Coherent Diffractive Imaging with a Transmission Sample

4.1. Overview of the experiment

Compared to CDI using synchrotron and free-electron laser sources, a table-top CDI using a high harmonic generation (HHG) source requires only a small laboratory scale setup, and also provides a high degree of spatial and temporal coherence. Using a 32 nm-wavelength high-harmonic beam for CDI, a single-shot spatial resolution of 78 nm has been achieved [118]. When a source at a wavelength of 13 nm is used a resolution of ~25 nm (~ 2λ) has been achieved with an exposure time of 30 s [40]. A single harmonic can be selected by using optical elements such as narrow-bandwidth multilayer mirrors but a significant loss of total harmonic intensity is incurred. Previous work in our laboratory has shown that it is possible to use a well characterized large bandwidth harmonic source for reduction of exposure time in a CDI experiment with a spatial resolution of ~ 150 nm [25]. Higher resolution using an isolated harmonic source has also been demonstrated. We have recently reported that a resolution of ~100 nm for a periodic sample image can be achieved from a 300 s integration-time diffraction pattern obtained with a few high-harmonic order source around 30 nm and a sample size of ~15 μm [30]. The size of the HHG beam at the sample spot was usually > 1 mm and therefore the effective photon flux for illumination of a micron-scale sample was also low. By using XUV focusing mirrors, a single harmonic beam can be confined to a smaller area that is comparable to the size of the sample. As a result the total photon flux through the sample is increased

by more than an order of magnitude and hence the exposure time needed to capture a full dynamic range diffraction pattern can be significantly reduced.

In this chapter, a spatial resolution of ~ 45 nm for a small size (3.5 μm x 3.5 μm) and a larger size (7 μm x 7 μm) sample image is demonstrated. A short exposure time of ~ 2 s can be achieved by using a focusing mirror with a narrow-bandwidth HHG source around 30 nm. By using two different size samples, the effect of different ratios of beam size to sample size are examined and this needs to be considered in order to obtain a high quality reconstructed image, where the plane-wave field and an additional phase correction need to be used in the reconstruction.

4.2. Experimental setup

A 1 kHz, 800 nm multi-pass, multi-stage, chirped-pulse amplifier laser system, which produces 30 fs pulses with an energy ~ 2 mJ is used in this experiment, as shown in Figure 4.1. The detailed experimental configuration and the optimization of the HHG is described in chapter 2. We have previously verified that the extreme-ultraviolet emission scales quadratically with gas pressure and interaction length, demonstrating that the target is operating in the phase-matched regime. In order to block the fundamental driving laser and also its scattering into the detector the high harmonic beam passes through several pinholes with diameter < 2 mm and a 200 nm-thick aluminium filter which has a 60% transmission in the wavelength range 17 – 60 nm. The effect of the aluminium oxide layers formed on both surfaces is very small and can be neglected. For an estimation, a typical thickness of a passivation layer of aluminium oxide is about 4 nm and its transmission at 30 nm wavelength is 90% [125]. The HHG radiation is reflected by an XUV plane mirror and a 10 cm-radius

focusing mirror in a Z-configuration to obtain a good focusing spot. The astigmatism of the focusing mirror is minimized since the reflection angle (~ 10°) and the HHG beam size (~ 2 mm) are small and the focus length (10 cm) is not too short. A deep-cooled 16-bit resolution CCD camera (Princeton Instruments PIXIS 2048 x 2048) with 13.5 x 13.5 μm pixel size is placed behind the sample to capture its diffraction pattern. The camera is cooled to -40°C to minimize thermal noise when taking diffraction data. The whole CDI apparatus downstream from the gas cell through different pumping stages is placed inside a vacuum chamber, in which the pressure is maintained at 10^{-5} Torr.

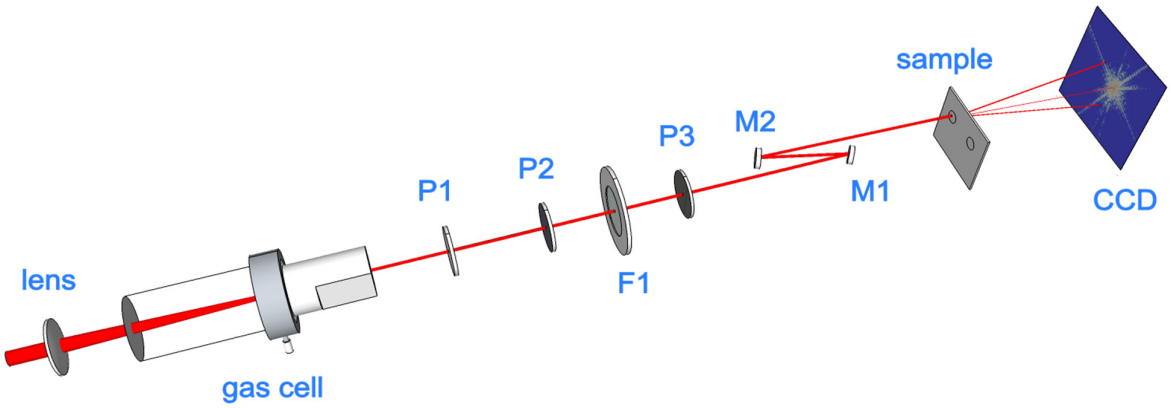

Figure 4.1: The tabletop CDI experiment using a high harmonic generation configuration. A laser beam is focused into an argon gas cell, then the generated harmonic beam is filtered by pinholes P1, P2, P3 and an aluminum filter F1. A single harmonic is selected and focused by XUV mirrors M1 and M2, and the diffraction pattern of the sample is captured by the CCD.

Two samples with dimension 7 μm x 7 μm (large sample) and 3.5 μm x 3.5 μm (small sample) are mounted in a motorized sample holder. The distance from the sample to the detector is optimized to achieve a sufficient oversampling ratio for easy reconstruction but still to produce a high resolution image. In this

experiment, the sample-detector distance z is chosen to be 3.5 cm, which satisfies the far field requirement $\left(z \gg \frac{D^2}{\lambda}\right)$, and leads to an NA of approximately 0.38 and a theoretical resolution of $\delta = 0.61\ \lambda/\mathrm{NA} = 46$ nm (Rayleigh criterion). On the other hand, the oversampling ratios for the large and small sample are:

$$O_L = \frac{z\lambda}{pD_L} = 11 \quad \text{and} \quad O_S = \frac{z\lambda}{pD_S} = 22$$

where the distance between the sample and detector z = 3.5 cm, wavelength λ = 30 nm, pixel size p = 13.5 μm, large sample dimension D_L = 7 μm and small sample dimension D_S = 3.5 μm. These high values of oversampling ratio ensure the reconstruction of the sample images is practical and feasible.

4.3. Enhancement using narrow bandwidth reflective and focusing mirrors

By using narrow bandwidth reflective and focusing mirrors, a single harmonic can be selected and confined to a tiny area which is comparable to the sample size, thus increasing the effective photon flux and reducing the required acquisition time. The mirrors used in the experiment are Optix Fab multilayer Mo/Si mirrors with 2 nm bandwidth and 35% reflectivity at 30 nm. From an incident HHG beam with a diameter of ~ 2 mm, a fine focus spot (~ 5 μm) is obtained by using a 10 cm focal-length focusing mirror. As a result, the effective photon flux is increased by more than an order of magnitude and thus the required acquisition time is significantly reduced.

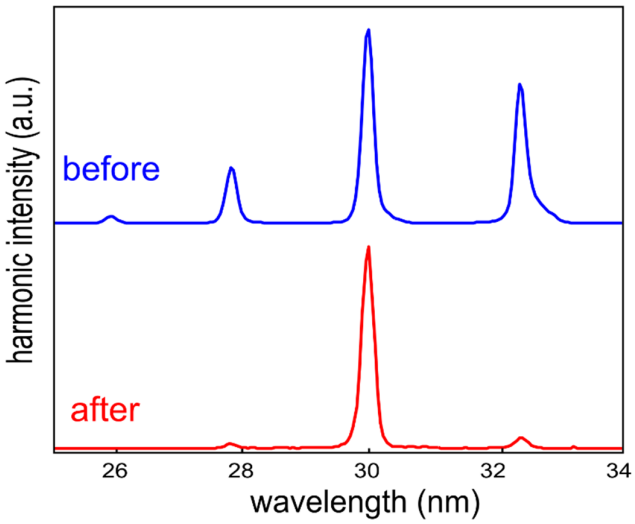

Figure 4.2: Measured spectrum of the HHG source before (blue) and after (red) traversing the mirrors, showing that a single harmonic (H27) at 30 nm is selected to illuminate the sample.

The spectrum of the HHG source is measured by an XUV grazing incidence diffraction spectrometer with a 300 grooves/mm grating, which is placed downstream in the experimental chamber. As shown in Figure 4.2, a single harmonic at around 30 nm (27^{th} harmonic) is isolated while the contributions of the two neighbouring harmonics are negligible, yielding a small bandwidth source ($\lambda/\Delta\lambda > 250$). As a result, the wave field which illuminates the sample can be approximated as a monochromatic source and hence the diffraction pattern can be estimated from the magnitude of a single Fourier transformation of the sample's image.

In order to determine the beam profile around the focus point, a diffraction scanning experiment with two 5 x 200 μm slits in an X-Y configuration is performed. As the slit is scanned across the beam, the intensity profile of the beam is extracted directly from the diffractive intensity which is recorded in the CCD camera.

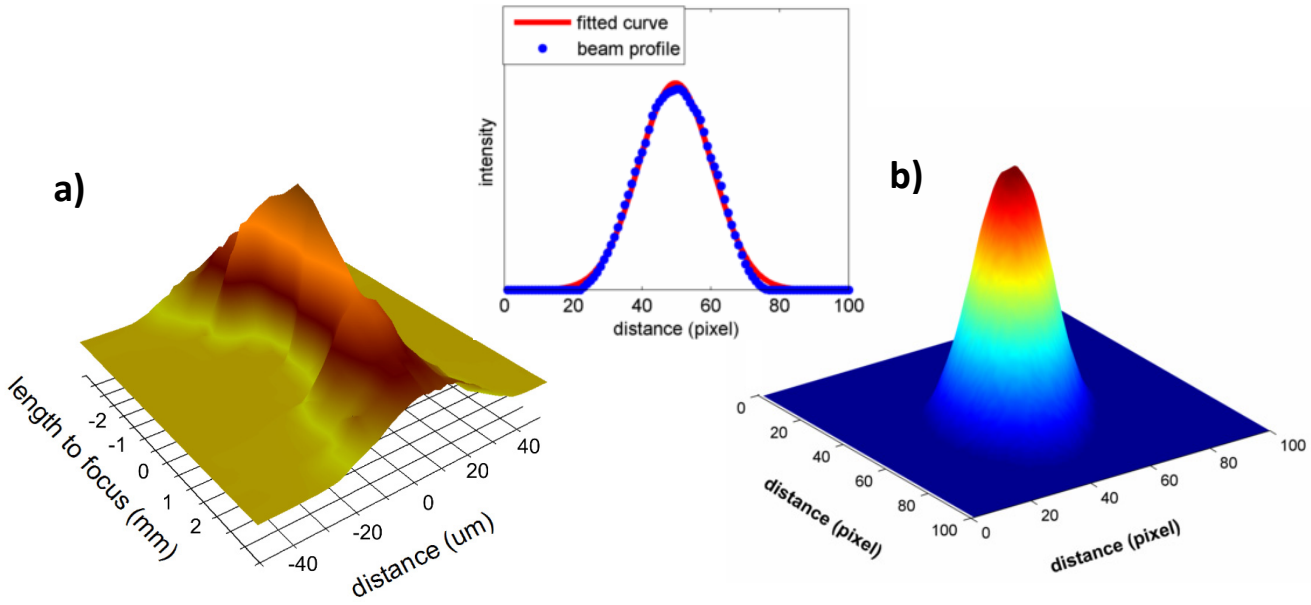

Figure 4.3: (a) The beam profile along the x-direction of the HHG source around the focus point, which is obtained from the scanning slit experiment, and (b) the beam profile recorded in the CCD camera with the fitting in the inset.

The beam profile of the HHG beam along the x-axis around the focus point (± 2.5 mm) is shown in Figure 4.3a, which indicates a focus size of ~7 μm (FWHM). At the distances ± 1.5 mm and ±2.5 mm, the respective beam profiles are 15 and 25 μm. A similar result is obtained with a scanning experiment along the y-axis, indicating a good focusing geometry and an even intensity distribution in the focus beam. The excellent beam profile after focusing is also confirmed by the captured intensity using the CCD camera (shown in Figure 4.3b), for which the intensity profile fits nicely with a Gaussian function (R^2 = 0.997, SSE = 0.04). By placing the sample at a closer distance relative to the focus point, a higher effective photon flux is obtained. However, reducing this distance leads to a reduction in the quality of the diffraction pattern because of the curvature of the wave field and the non-perfect focus spot. This problem is discussed later in this chapter.

4.4. Measuring the HHG spectrum from the diffraction pattern of a multi-pinhole array sample

In order to successfully reconstruct the image in a CDI experiment, a narrow spectrum and a high degree of coherence of the source must be ensured and these measurements require the installation of a spectrometer. However, it is difficult to use a spectrometer to check the spectrum of the source and to capture the sample's diffraction under the same experiment conditions. A novel technique is applied to deal with this challenge, in which the source's spectrum is determined by analysing the diffraction pattern of a predefined sample. In this experiment, a sample consisting of a 6 μm x 6 μm array of pinholes, which are milled on a Si_3N_4 membrane, as shown in Figure 4.4a, is used to determine the source's spectrum from its diffraction pattern. Each pinhole is 180 nm wide in diameter and the distance between two centres is 280 nm.

The array of pinholes in the sample is used as a 2D grating spectrometer, where the diffraction pattern is a product of the diffraction of the pinhole and the diffraction of the grid. Furthermore, the design of the sample makes the diffraction pattern observable only at the reciprocal lattice points. The simulated diffraction by a single wavelength source of this sample is shown in Figure 4.4b.

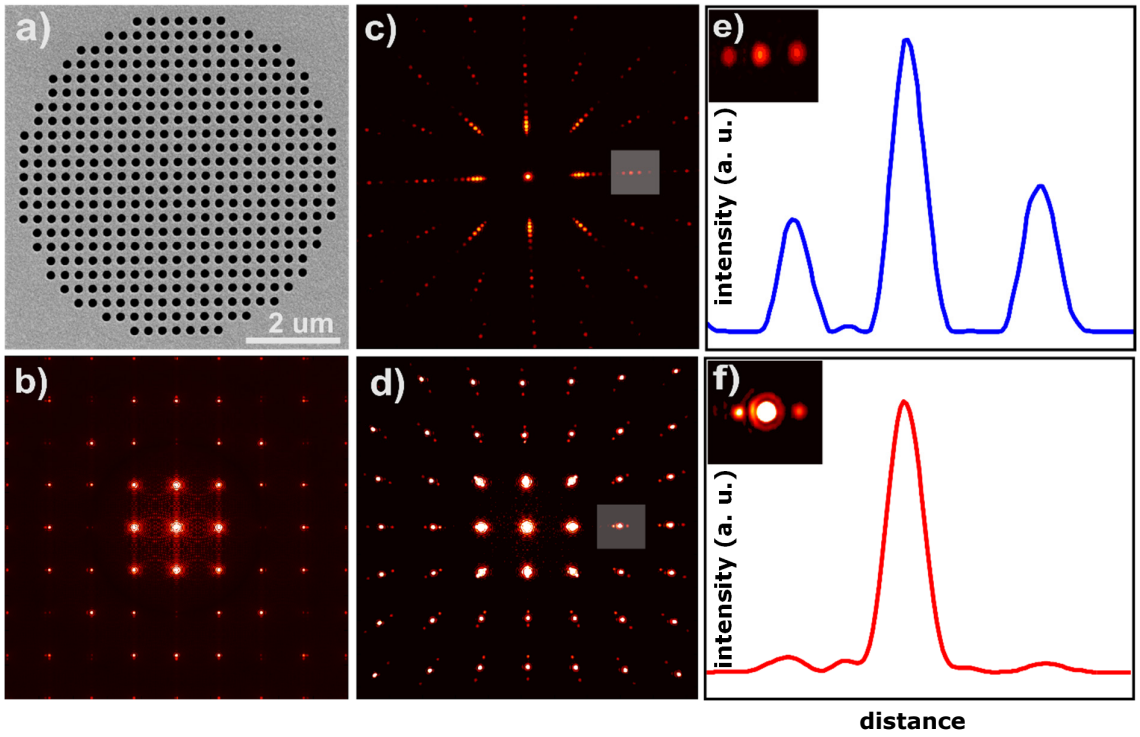

Figure 4.4: a) Scanning electron microscope image of a sample consisting of an array of pinholes used to measure the source's spectrum. b) Simulated diffraction pattern of this sample by a single-wavelength source. c), d) Measured diffraction patterns with the HHG source without and with the XUV mirrors. e), f) Cross sections of the highlighted areas of the diffraction patterns revealing the frequency spectrum of the source without and with the mirrors.

As clearly seen, the diffraction pattern consists of equally spaced Airy disks, with the highest peaks closest to the centre. If the source consists of multiple harmonics, the diffraction pattern is an incoherent superposition of the diffraction by each harmonic incident on the sample [119]. In fact, the diffraction pattern is "rescaled" by different wavelengths, where the shorter wavelength tends to compress and the longer wavelength expands the pattern, which is described by equation (3.6). This observation can be seen in the diffraction pattern of the sample using the HHG beam without the mirrors (Figure 4.4c) and with the mirrors (Figure 4.4d), which are displayed with highly nonlinear colour scales. When using mirrors, the sample is placed at a reasonably large distance from the

focus point to ensure the wave field at the sample plane can be approximated as a plane field. The diffraction image will be distorted when the sample is located close to the focus or the beam size is comparable to the sample size. The respective enlargements of a selected area of the diffraction patterns (highlighted by the grey colour) are shown in Figures 4.4e and 4.4f, where the horizontal cross-section plots reveal the relative contribution of different wavelengths to the diffraction patterns. These plots indicate the respective frequency spectra of the source without and with the XUV mirrors, which are in reasonable agreement with the measured spectrum as shown earlier in Figure 4.2.

4.5. The "SWIN" samples

Two 'SWIN' transmission samples with a similar pattern, whose dimensions are 7 μm x 7 μm (large sample) and 3.5 μm x 3.5 μm (small sample), are used as the test samples in the CDI experiment with a 30 nm wavelength source. The dimension of the small sample is chosen to be half that of the large sample, as shown in Figure 4.5. These samples were fabricated on a 50 nm-thick Si_3N_4 membrane, which was coated with 50 nm and 150 nm gold on each side, using the electron beam lithography facility in the Nanofabrication Laboratory (Centre for Micro-Photonics, Swinburne University of Technology).

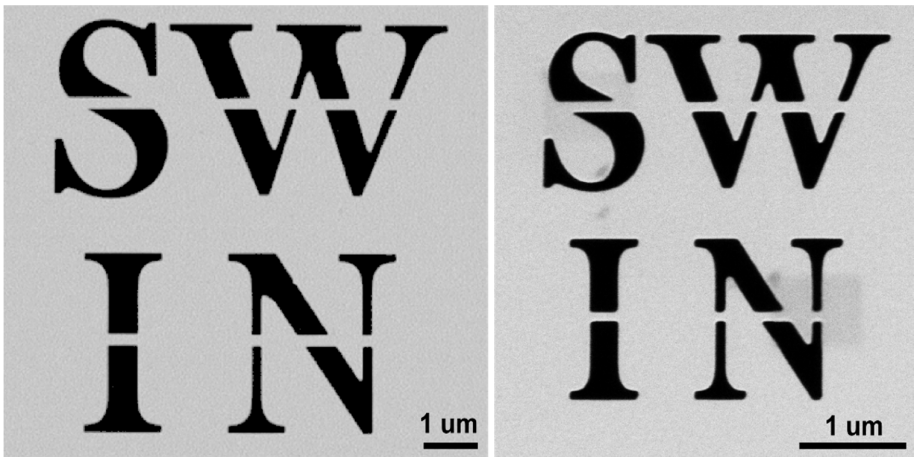

Figure 4.5: Scanning electron microscope image of the SWIN large (left) and small (right) samples. The height of the letters in the large sample is 3 μm, and 1.5 μm in the small sample.

By milling on the gold-coated Si_3N_4 membranes, it ensures that the wave field is 100% transmitted through the letter patterns in the SWIN samples while the background is completely "dark". Thus the sample can be considered as a binary sample and the exit surface wave is the same as the sample's image since the sample thickness is much smaller than its size. These samples are mounted on a sample holder with X-Y-Z positions that can be controlled by a motorized translation stage with a resolution of 100 nm. Thus the sample's position can be precisely adjusted to achieve optimal illumination and diffraction quality.

4.6. Diffraction pattern acquisition and processing

For each of the SWIN samples, diffraction patterns are taken at various distances relative to the focus point, including ±2.5 mm and ±1.5 mm, where positive distances mean behind the focus point. By controlling various experimental parameters, such as gas pressure, driving laser intensity and focus position inside

the gas cell, the high harmonic generation process is optimized with highest illumination around 30 nm. By recording the beam profile directly on the CCD camera, the position and intensity of the XUV source can be precisely adjusted. Then the sample is carefully moved into the beam path and its position is fine-tuned until the sample is placed at the centre of the beam, where the intensity of the centre peak of the diffraction pattern is maximum.

To minimize instrumental and environmental noise that may affect the quality of the diffraction pattern, the whole imaging apparatus is placed in a dark vacuum chamber. Also, the sample holder is made sufficiently large to prevent scattered light inside the chamber from hitting the detector as much as possible. On the other hand, the CCD camera is cooled down to -40°C while capturing data to minimize the thermal noise of the sensor.

At each distance, 20 diffraction patterns and another 20 background images are taken and averaged to increase the signal to noise (S/N) ratio. The background image is taken when the gas cell is completely vented, i.e., when no harmonic can be generated. The final diffraction pattern is obtained after subtraction of the averaged background from the averaged diffraction pattern, where negative intensity is rounded to zero.

At a distance ±2.5 mm, it takes 2 s to capture a full dynamic range (~65000 counts) diffraction pattern of the large sample, while the small sample requires 8 s. When the samples are placed closer to the focus point at ±1.5 mm, the effective photon flux is significantly increased; hence the required exposure times are only 1 s and 4 s for the large and small samples, respectively. The diffraction patterns of the large and small samples at these two distances are shown in Figure 4.6, from which the effect of the curvature of the focused beam can be clearly seen in images b) and d), as the features tend to blur and become broader.

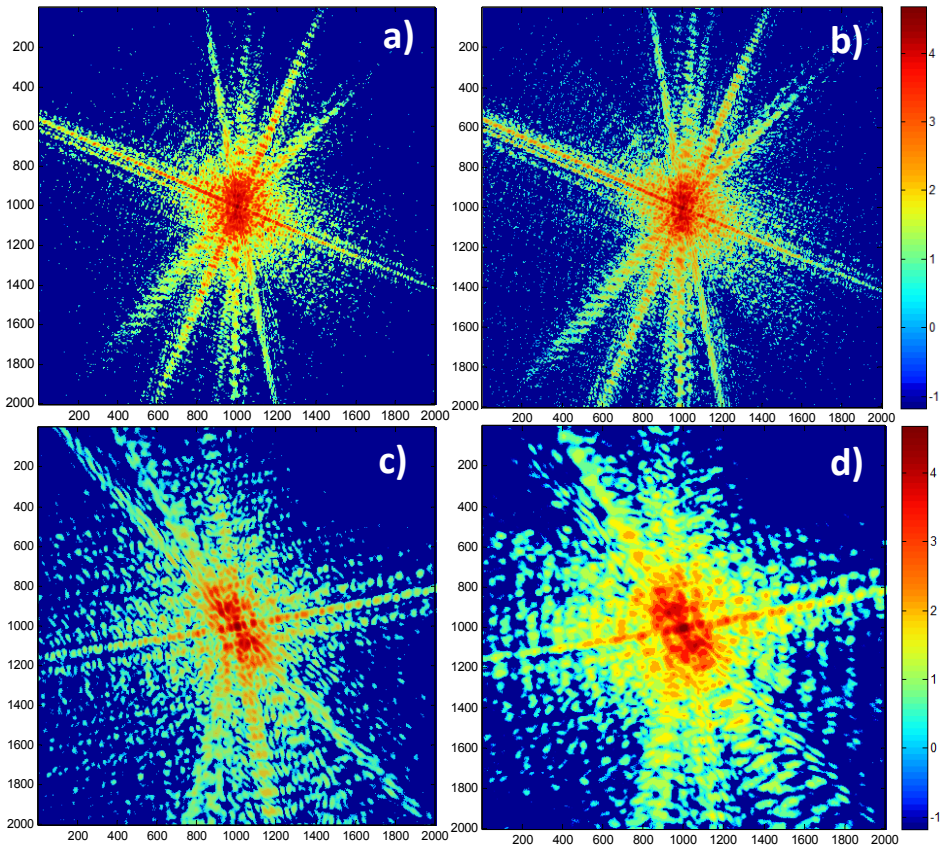

Figure 4.6: a), b) Log-scale diffraction patterns of the large SWIN sample at 2.5 mm and 1.5 mm, c), d) Diffraction patterns of the small SWIN sample at the same distances.

Since the diffraction data must satisfy the symmetry property and the highest intensity peak must lie at the centre of the diffraction pattern, the data is examined to crop and reposition the centre peak exactly in the middle of the pattern. Depending on the S/N quality, the diffraction pattern may be filtered with a median and Gaussian filter to smooth the image and increase the S/N ratio, while replacing any negative intensity with a zero value. After post-processing steps, the diffraction data is ready for the reconstruction process, as described earlier in section 3.4.

4.7. Reconstruction results with a plane-wave field approximation

At a distance of ±2.5 mm, the focused beam's diameter is much larger than the sample size (4 times for the large and 8 times for the small SWIN sample); thus the wave field which illuminates the sample can be considered as a plane wave, and the Fraunhofer approximation can be used in the phase retrieval algorithm to reconstruct the sample "shadow" image.

An iterative image reconstruction is performed based on the far-field approximation of a plane field by considering Fraunhofer diffraction at the detector plane, as discussed in section 3.4. The Error Reduction (ER) and Hybrid Input Output (HIO) algorithms are used to recover the sample's image, with a fixed support constraint. A rectangle whose dimension is sufficiently larger than the sample size is used as a support constraint. The size of this rectangle can be determined from the first few HIO iterations. This size is flexible and only has a minor influence on the resolution of the reconstructed image.

The reconstructed images of the large and small SWIN samples are shown in Figure 4.7, and the respective intensity profiles of the selected lines are extracted.

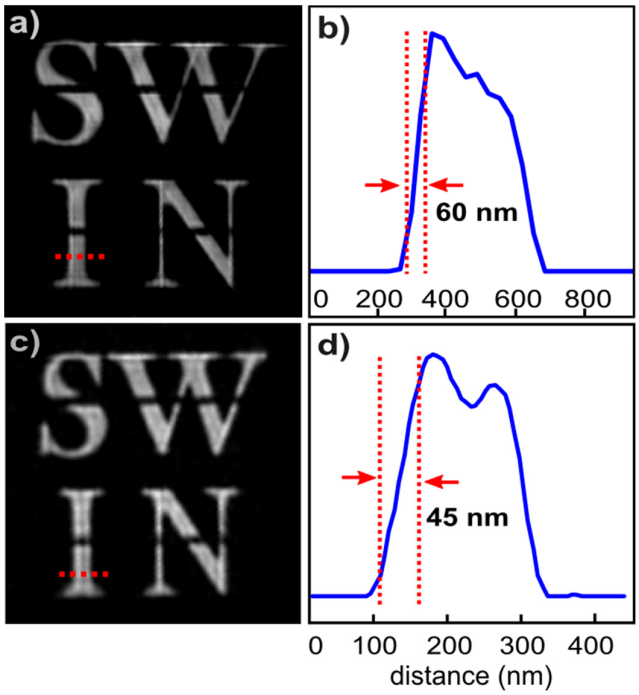

Figure 4.7: Reconstructed image of the large (a) and small (c) SWIN samples with a plane-wave field at a distance 2.5 mm. The intensity profiles of the red lines across the letter "I" are shown for the large (b) and small (d) samples, and reveal a corresponding resolution of 60 nm and 45 nm .

As can be seen, the Fraunhofer approximation is valid and the reconstruction algorithm with a plane-wave field can be used to recover the sample images at a reasonably far distance from the focus point, where the beam size is much larger than the sample size and the curvature of the field due to focusing is negligible. To determine the resolution of the reconstructed images, intensity profiles across the letter "I" are plotted and the distances from 10% to 90% of the transitions from dark to white intensities are determined. For the large sample, a resolution of 60 $\pm$ 5 nm is obtained, while a better resolution of 45 $\pm$ 5 nm for the small sample is achieved. Compared to the theoretical estimate, the resolution based on the Rayleigh criterion is 46 nm, which perfectly matches the calculation of the resolution limit.

At a distance of 1.5 mm from the focus point, the beam's diameter is now only two times larger than the sample's dimension; therefore, the diffraction pattern of the large sample suffers from a strong curvature due to the focused source. However, for the small sample, the beam size is still four times larger than the sample size and the plane-wave field approximation is still valid for the reconstruction. The reconstructed images of the large and small samples at this distance are shown in Figure 4.8.

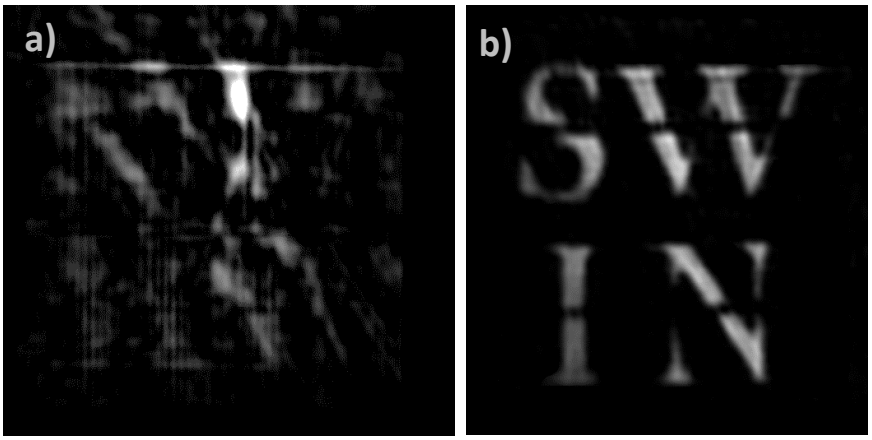

Figure 4.8: Reconstructed image of the large (a) and small (b) SWIN samples with a plane-wave field at a distance 1.5 mm.

As can be seen, due to the strong curvature of the wave field, the Fraunhofer approximation is no longer valid for the large sample; thus the large SWIN image cannot be reconstructed. On the other hand, since the beam size is much larger than the small sample and the plane-wave approximation is still applicable, the image can be reconstructed using a normal phase retrieval algorithm.

4.8. Curvature correction in the phase retrieval algorithm

With the focusing mirror, the effective photon flux at the sample spot can be significantly increased and hence the required exposure time is reduced. However, using a focusing mirror leads to curvature of the wave field and the plane-wave requirement for a CDI experiment may not be satisfied; so the variation of the phase and intensity of the source across the sample needs to be taken into account. As seen in the previous result, when the beam size is comparable to the sample size (two times for the large sample at 1.5 mm), the curvature of the wave field has already invalidated the phase retrieval algorithm. If the object is located near the focus point and the intensity variation is assumed to be not too large, the curvature problem can be corrected by considering a phase variation at the sample plane. As discussed earlier in chapter 3, the diffraction pattern then becomes similar to a Fresnel approximation:

$$E_i(x,y,z) = \frac{\exp(ikz)}{i\lambda z}\exp\left[\frac{ik}{2z}\left(x_i^2+y_i^2\right)\right]\mathcal{F}\left\{E_0\exp\left[\frac{ik}{2d}\left(x_0^2+y_0^2\right)\right]\right\} \qquad (4.1)$$

where d is the distance from the focus point to the sample plane.

To adapt the new phase term in the Fourier transform operator, the phase retrieval algorithm is now modified and the new steps are implemented as follows:

1) The sample's image is initialized with a random guess or a support image as *a priori* information: *g(r).*
2) The magnitude and phase at the detector plane is calculated by taking a Fourier transform of the product of the sample image and the phase term $\left(\exp\left[\frac{ik}{2d}\left(x_0^2+y_0^2\right)\right]\right)$ as described in equation (4.1):

$$G(u) = \mathcal{F}\left\{g(r) * \exp\left[\frac{ik}{2d}\left(x_0^2+y_0^2\right)\right]\right\} = |G(u)| * \exp(i\Phi) \qquad (4.2)$$

3) The magnitude $|G(u)|$ is replaced by the Fourier modulus (square root of the diffraction intensity measured by the detector $I(u)$). The updated image in real space is calculated by taking the inverse Fourier transform of the updated $G(u)$:

$$g'(r) = \mathcal{F}^{-1}\left\{\sqrt{I(u)} * \exp(i\Phi)\right\} \tag{4.3}$$

4) The actual sample's image is then calculated by dividing the updated image by the same phase term that was used in step 2:

$$g(r) = \frac{g'(r)}{\exp\left[\frac{ik}{2d}\left(x_0^2 + y_0^2\right)\right]} \tag{4.4}$$

5) A support constraint is applied to the image from step 4 to obtain an updated sample's image, including ER and HIO algorithms.

The phase retrieval process is repeated again from step 2 for a finite number of iterations until the quality of the updated sample's image satisfies the requirement.

The "phase term" in the reconstruction algorithm is used to simulate the curvature of the wave field in the sample plane, which is analogous to a known "fitting parameter" for reconstruction. Adding this parameter results in faster convergence of the reconstruction process [120], where an incident spherical phase curvature and the use of the subsidiary assumption that the scattering may be regarded as coming from a real object of finite support results in significantly accelerated convergence of the iterative algorithms, compared with the use of plane-wave illumination.

The same diffraction pattern that was unsuccessful in reconstruction of the large SWIN image using a plane-wave field (as shown in Figure 4.8a) will be used for

the modified phase retrieval algorithm, which takes the curvature term into account in the reconstruction.

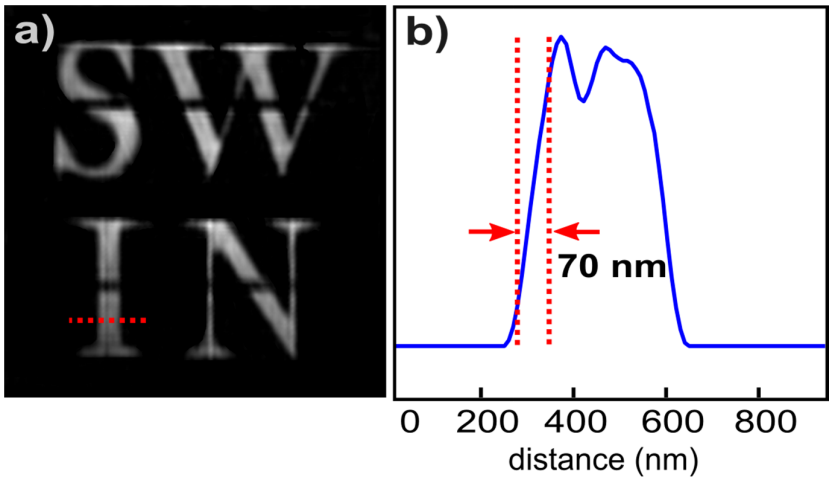

Figure 4.9: Reconstructed image of the large SWIN sample at 1.5 mm with the curvature correction (a). The knife-edge test on the letter "I" indicates a resolution of 70 nm is achieved.

The excellent reconstructed image of the large SWIN sample is shown in Figure 4.9, which clearly demonstrates the accurate approximation of the curvature correction in the reconstruction algorithm. A knife-edge test on the letter "I" indicates a resolution of 70 nm is achieved, which is slightly lower than the plane-wave reconstruction at 2.5 mm.

At distances shorter than 1.5 mm from the focus point, not only the strong curvature of the focused field, but also the intensity variation of the beam affects the quality of the diffraction pattern, since the focused source is not a perfect Gaussian beam. Non-uniform illumination causes non-symmetric patterns in the diffraction data; thus a reconstruction with only the curvature correction is not possible.

4.9. Enhancement of the reconstruction process with the Graphical Processing Unit (GPU)

One of the drawbacks of the coherent diffractive imaging technique is the heavy post-processing stages, including the reconstruction process, which deals with a large amount of data and computation steps. The most time consuming calculation is the fast Fourier transform (FFT) operator with a matrix whose size is up to 2048×2048 elements.

Usually a construction process requires thousands of iterations [40][26][121], in which each iteration consists of one FFT and one inverse FFT operation. Traditionally, a reconstruction program which runs on a single CPU computer is a time consuming process. By implementing the reconstruction algorithm on a graphical processing unit (GPU), the calculation is spread out over a massive number of parallel computational units, and thus the reconstruction time is dramatically reduced.

In our experiment, the reconstruction process is performed on a desktop computer, in which a Tesla K20c GPU is installed. Featuring 2496 computational units (CUDA cores), the GPU is capable of processing 1.17×10^{12} double-precision floating-point operations per second (flops), which is about 10 times better than a typical Intel Core i7 CPU [122]. The reconstruction program is written in MATLAB, which uses a Parallel Computing Toolbox to utilize the GPU functionality. To compare performance, the reconstruction is performed using data sizes of 512×512, 1024×1024 and 2048×2048 elements with the CPU alone and with the GPU, as shown in Figure 4.10.

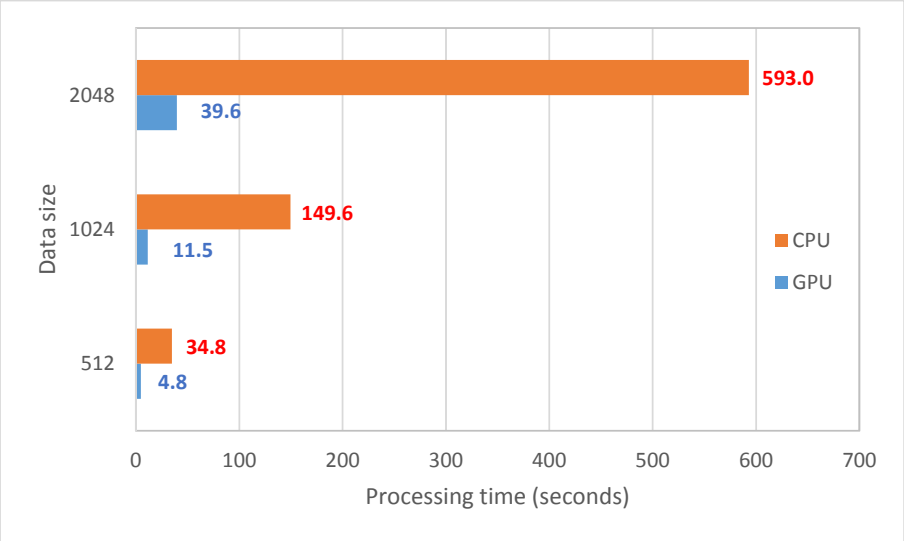

Figure 4.10: Comparison of the reconstruction time using the Intel Core i7 CPU alone (orange) with the Tesla K20 GPU (blue) for three different data sizes.

As clearly seen, the reconstructions with the GPU perform around 15 times faster than with the CPU alone, taking only ~40 seconds for the 2048×2048 data while the CPU needs nearly 10 minutes to reconstruct the same image. The 1024×1024 data is processed 4 times faster than the 2048×2048 data, where in our experiment the 1024×1024 data is processed to produce a coarse image, then the reconstruction parameters are adjusted and a finer high resolution image is reconstructed from the 2048×2048 data. To effectively perform the reconstruction process, a user interface is built from the MATLAB software, as shown in Figure 4.11.

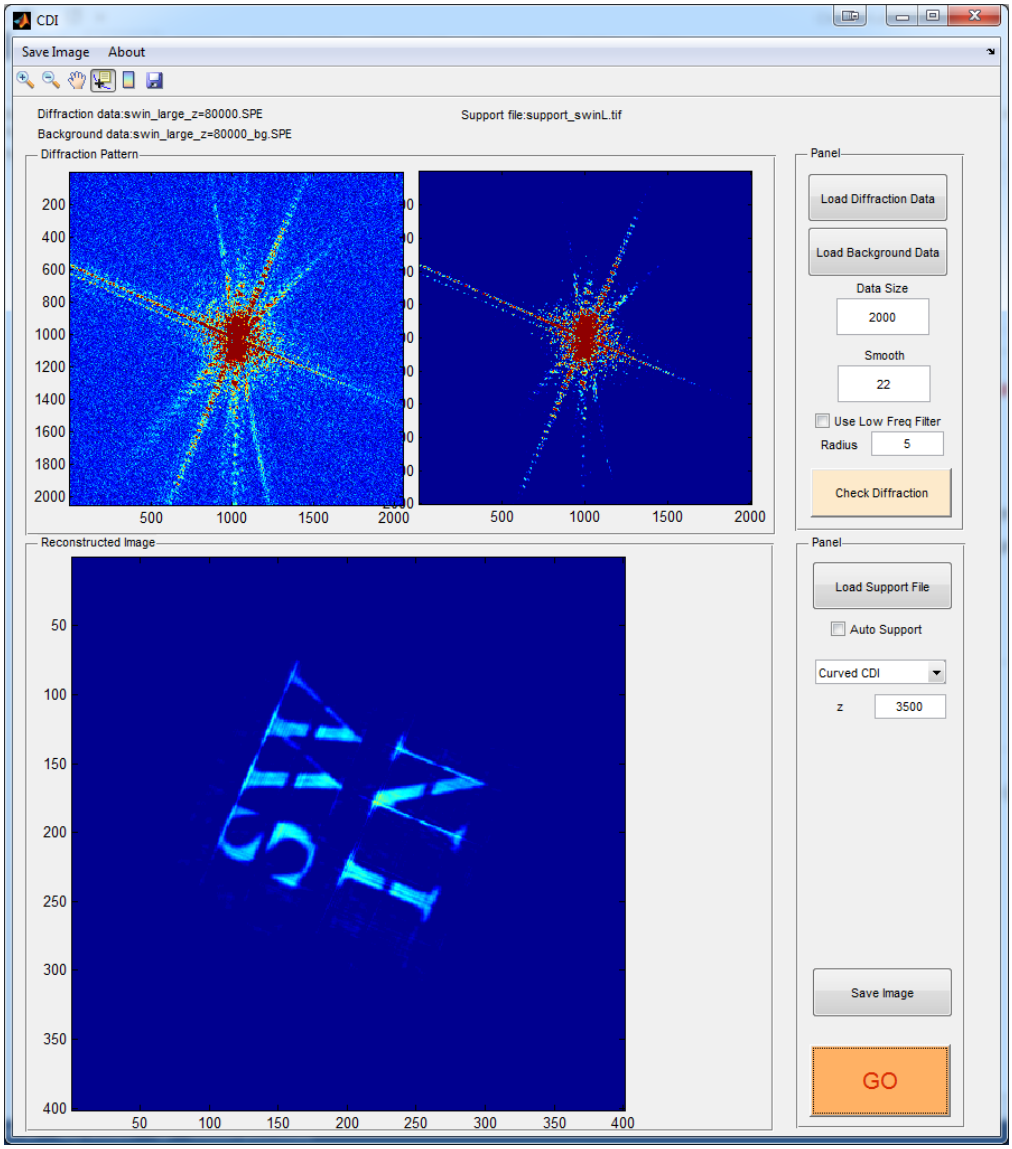

Figure 4.11: The user interface of the reconstruction program.

With the interface, the user can select the data file and background file, adjust the reconstruction parameters and watch the result in just a few seconds. This allows the user to reconstruct the image as soon as the diffraction data is available, which opens the possibility of live imaging. By incorporating the reconstruction program with the acquisition software, the whole experiment can be integrated into a single program, which makes CDI one step closer to live imaging, similar to the optical microscope and the electron microscope.

4.10. Conclusion

We have demonstrated that a high resolution image (45 nm resolution) can be reconstructed from the diffraction pattern generated by a table-top high harmonic source at a wavelength around 30 nm. By using focusing mirrors, a single harmonic can be selected and converged to illuminate the sample. As a result, the quality of the diffraction pattern is improved and the required exposure time is significantly reduced. In order to increase the quality of the reconstructed image, the object needs to be placed at an optimum distance from the focus point to ensure the object is illuminated by an approximate plane wave. By applying a phase correction in the reconstruction process which takes the curvature of the field due to the focusing mirror into account, not only the reconstruction converges faster, but also the sample can be placed at a closer distance to the focus point and hence we can take advantage of the higher photon flux and shorter acquisition time, without compromising resolution.

Chapter 5

Coherent Diffractive Imaging with Absorption Samples

5.1. Overview of the experiment

Transmission samples, such as the 'SWIN' samples, are useful as test objects in coherent diffractive imaging, since the surface exit wave is actually the binary image of the sample. These samples can be used to test a phase retrieval algorithm or to determine the feasibility of the new CDI experiment setup, as the manufacturing process is relatively simple and the sample can be made precisely as designed, using the electron beam lithography technique. Furthermore, the reconstruction is straight-forward, where the sample can be treated as an object with a real intensity distribution. However, in practice these samples are not scientifically similar to real-world samples, such as biological specimens, which are prepared on a thin layer for imaging purposes. Due to the fact that the XUV radiation is strongly absorbed by most materials, the reconstructed image of these samples will be inverted, i.e., the object of interest will be displayed as dark on a bright background, which is opposite to the transmission CDI images. In this chapter, a CDI experiment with three absorption samples, whose characteristics are similar to biological samples, are investigated using a high harmonic source with wavelength around 30 nm. The experimental setup is the same as the one used for the previous experiment with the transmission samples in chapter 4, which includes the narrow band reflective and focusing mirrors and the curvature correction phase retrieval algorithm.

5.2. The samples

Three samples with biological-like characteristics which were selected from a large number of candidates are used to demonstrate the capability of the table-top CDI experiment. These samples were prepared as a result of a collaboration with the Ultrafast and Microspectroscopy Laboratories at The University of Melbourne. All three samples were fabricated on 30 nm-thick silicon nitride films where the dimension of the window space is around 13 x 13 μm, which is located in the middle of a 200 μm-thick, 4.4 x 4.4 mm frame. Unlike the previous CDI experiment with a transmission sample, the strong absorption objects in this experiment are deposited on a semi-transparent silicon nitride membrane, which has a transmission capability up to 30% at the 30 nm wavelength [79]; as a consequence the images of these objects will appear "black" on a "white" background. This characteristic is very similar when imaging biological samples using x-ray sources, in which the contrast of the image is derived from the difference of the atoms' absorption edges between the sample and the membrane or between different materials in the sample itself.

These samples (namely samples A, B and C) are placed in the same sample holder as used in the previous experiment with the 'SWIN' samples; thus the position in the X-Y-Z directions can be precisely controlled.

5.2.1. Sample A

The first sample (called sample A) consists of 2 μm-diameter plain silica (SiO_2) spheres on a silicon nitride membrane, as shown in Figure 5.1. Only the particles inside the window can be seen in the reconstructed image, as the Si_3N_4 membrane is sufficiently thin for transmission of the XUV radiation. The silica spheres have strong x-ray absorption properties for wavelengths longer than 3 nm, and nearly

no transmission at all wavelengths around 30 nm [79]. Among the silica spheres, there are some 400 nm-diameter amino polystyrene ($NH_2C_8H_8$) particles placed in the gaps, which also strongly absorb the x-ray radiation.

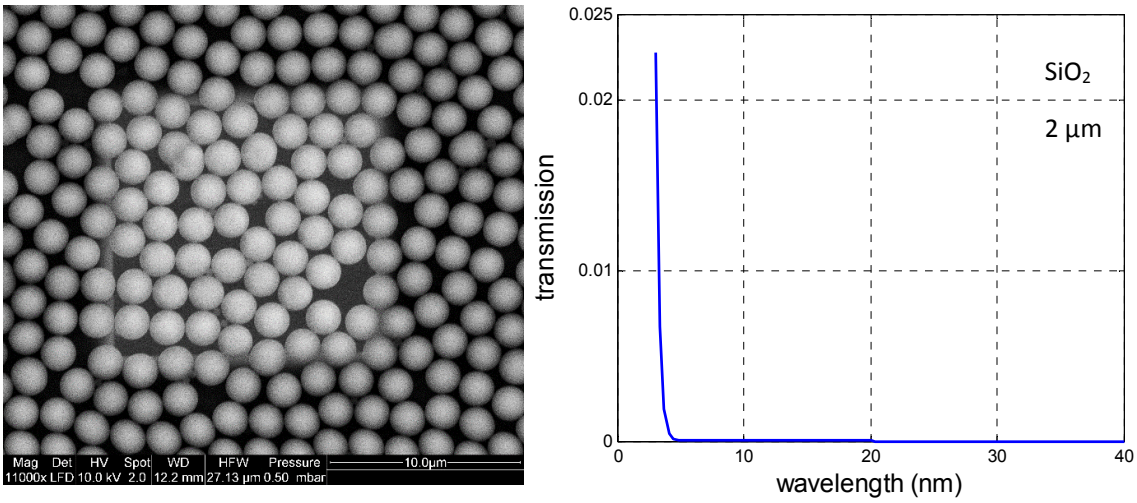

Figure 5.1: Scanning electron microscope image of sample A (left) and transmission characteristics of a silica sphere in the XUV region (right). The diameter of the silica sphere is 2 µm. Source: http://henke.lbl.gov.

5.2.2. Sample B

The second sample consists of similar material to sample A; it has 2 µm-diameter plain silica spheres and 400 nm-diameter amino polystyrene particles. In this sample, the number of plain silica spheres is reduced while more amino polystyrene particles are added to the window, as shown in Figure 5.2. The transmission characteristics of the amino polystyrene particles also indicates strong absorption of this material at wavelengths around 30 nm. As a consequence, the reconstructed image of this sample should consist of completely dark objects on a bright background. Since the transmission area (Si_3N_4 membrane) in the window is relatively large and the XUV beam easily penetrates through the sample, the detector will be quickly saturated by the high harmonic

photons. As a result, this creates a big challenge for the acquisition and processing of the diffraction pattern, in which the intensity is dominated by the zero frequency part and the dynamic range of the captured data is limited. Another challenge is to resolve the small particles in a cluster, as the x-ray radiation could not easily traverse the gaps between the amino polystyrene particles to create a diffraction pattern.

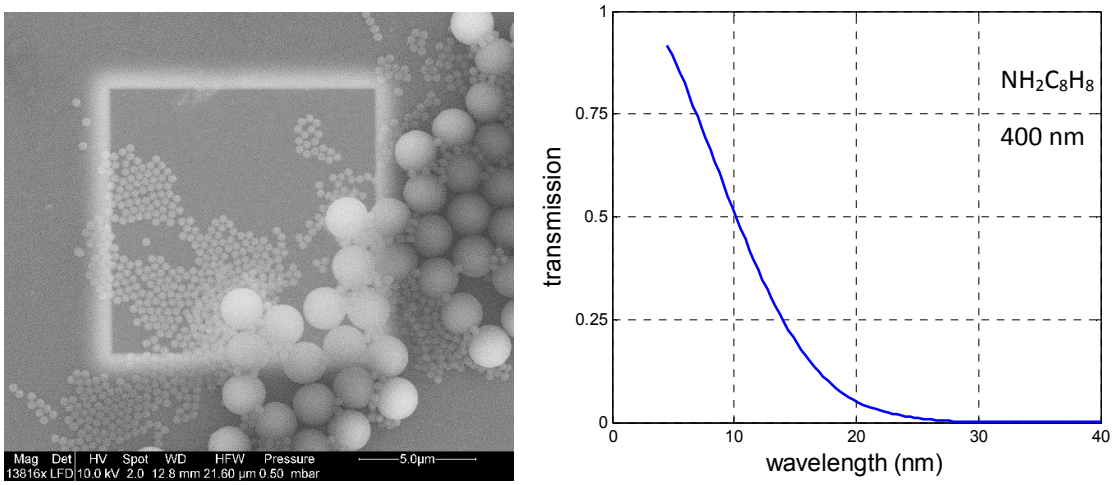

Figure 5.2: Scanning electron microscope image of sample B (left) and transmission characteristics of the amino polystyrene particles in the XUV region (right). The diameter of the amino polystyrene particle is 400 nm. Source: http://henke.lbl.gov.

5.2.3. Sample C

The third sample uses a different material to fabricate the microspheres on the windowed membrane, which is carboxylated polystyrene ($COOHC_8H_8$). In this sample, a total of 8 spheres with a 2 µm diameter are deposited on the membrane, which forms an isolated cluster in the middle of the window. In addition, some 400 nm-diameter amino polystyrene particles are also placed in the gaps between the big spheres and, most interestingly, there are four nanoparticles which form an isolated cluster, as can be seen below the big cluster in Figure 5.3. The

transmission characteristics of the carboxylated polystyrene sphere are also shown, which indicates strong absorption with XUV radiation at wavelengths around 30 nm. As a result, these spheres will appear "black" on a "white" background in the reconstructed image. Similar to sample B, the transmission area in this sample is enormous and the detector will be easily saturated by the high photon flux of the source. In fact, with the larger "bright background" area, this sample creates a greater challenge to reconstruct a sufficiently high resolution image that can resolve the sphere's details, especially the small particles.

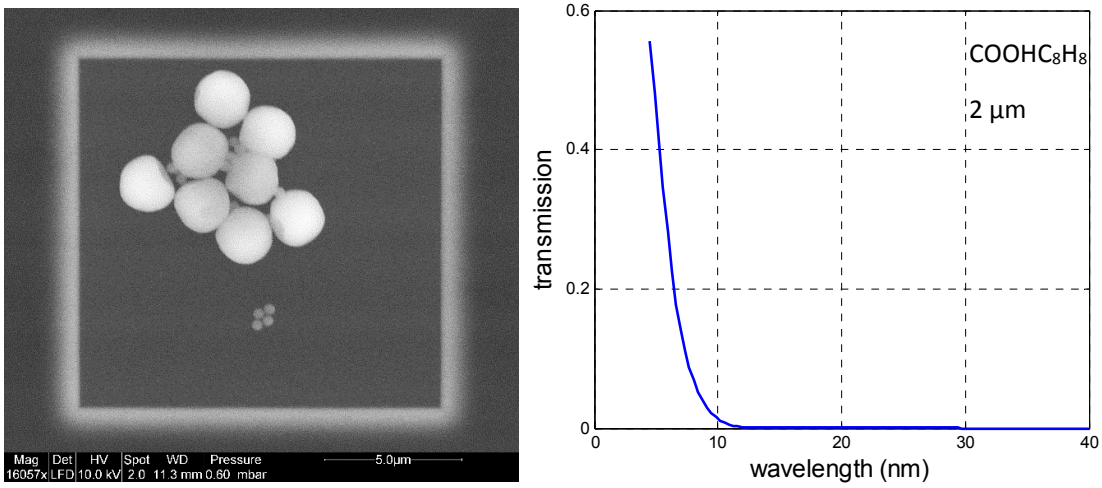

Figure 5.3: Scanning electron microscope image of sample C (left) and transmission characteristics of a carboxylated polystyrene sphere in the XUV region (right). The diameter of the carboxylated polystyrene sphere is 2 µm. Source: http://henke.lbl.gov.

5.3. Diffraction acquisition and processing

All three samples are placed at a distance 2 mm beyond the focus point of the XUV focusing mirror; at this distance, the photon flux from the focused beam is sufficiently high while we are still able to reconstruct the sample's image using a curvature correction-phase retrieval algorithm (as discussed in chapter 4). For

each sample, the high harmonic source is optimized to generate the highest intensity around 30 nm and the sample is precisely positioned at an optimum location to utilize as much photon flux as possible.

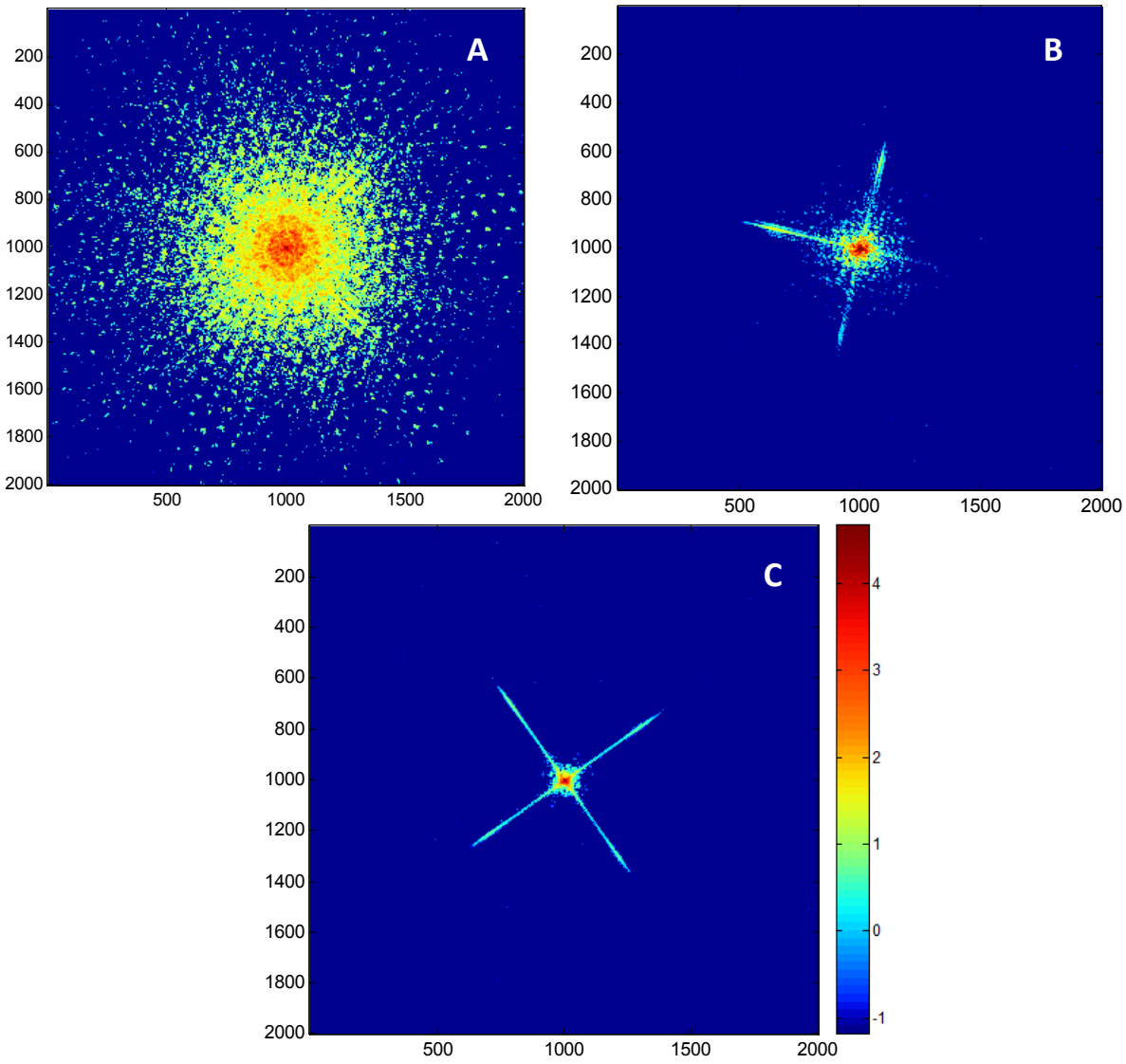

Figure 5.4: Diffraction patterns of samples A, B and C, which are displayed on a log scale with a nonlinear colour map.

The exposure time is adjusted so that the highest intensity nearly reaches the saturation limit (~65000 counts) of the CCD camera. To minimize the noise that may originate from instruments or the environment, the diffraction data are taken when the CCD is cooled down to -40°C and the sample chamber is covered in

complete darkness. Furthermore, at each sample, 80 diffraction patterns and 80 background data with the same exposure time are taken and then averaged to increase the signal to noise ratio. The resultant data is then cropped to reposition the intensity peak to the centre of the diffraction pattern.

The diffraction patterns of the three samples are shown in Figure 5.4, after averaging and repositioning the centre peak. The diffraction patterns are displayed on a log-scale with a highly nonlinear colour map. The required exposure time to capture a full dynamic range diffraction pattern for sample A is 10 seconds, while it takes only 3 seconds and 1.5 seconds for samples B and C, respectively. As can be seen, the diffraction pattern of sample A just reaches the edge of the CCD while the diffraction patterns of samples B and C only occupy around the centre part of the CCD area, due to the large transmission area, and lack of all the high frequency intensities which are further than half-way to the edge of the detector sensor. As a result, the reconstructed images of samples B and C are expected to be blurry and the edges of the spheres may not be resolved. The high intensity "crosses" in diffraction patterns B and C indicate that the main contribution of the diffracted light originates from the square shape of the silicon nitride windows, which can be resolved clearly in the reconstructed images.

5.4. Reconstruction results

At a distance 2 mm from the focus point, the high harmonic beam's diameter is about 20 μm and is only twice the sample dimension. As a result, the samples are illuminated with a strong curvature wave field and thus the diffraction patterns are no longer considered as Fourier transforms of the surface exit wave of the sample. Therefore, a modified phase retrieval algorithm with curvature correction (as described in chapter 4) is needed to recover the samples' images.

To demonstrate the effectiveness of the curvature correction-phase retrieval algorithm, an image of sample A is reconstructed by using both a plane wave and curved wave approximation, since the diffraction pattern of this sample has the higher quality compared to the other samples.

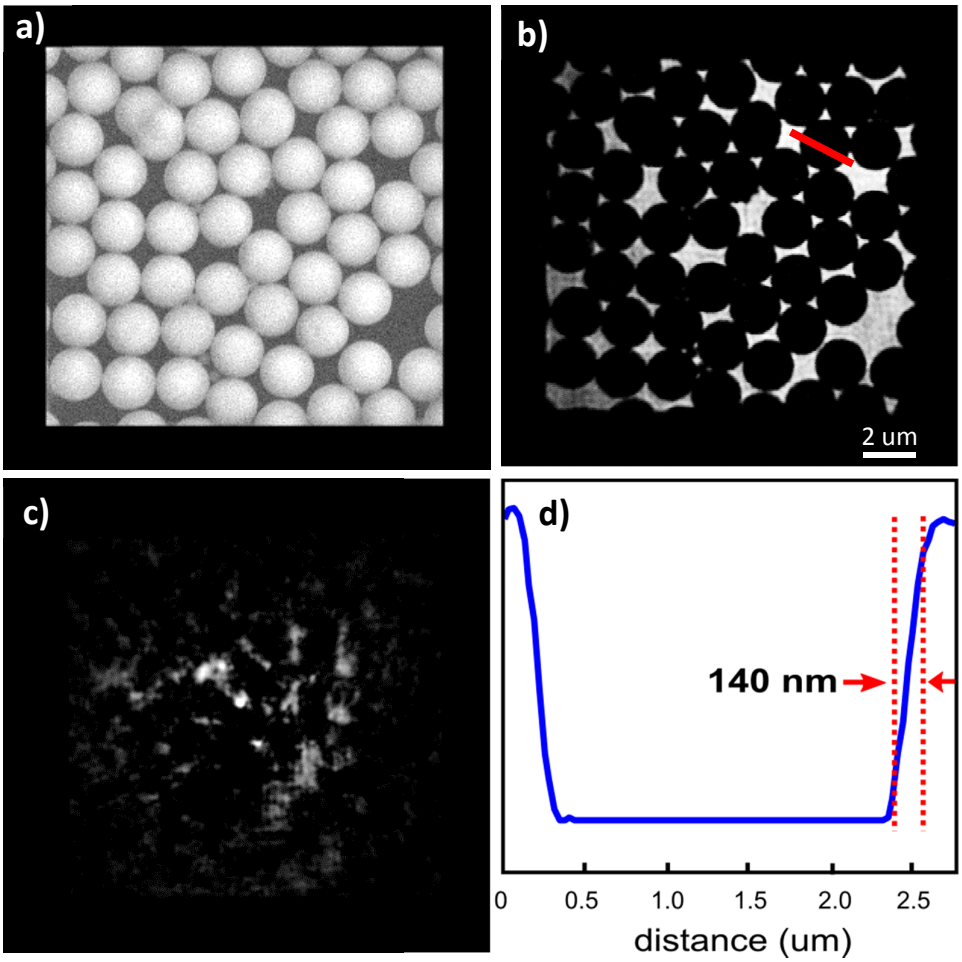

Figure 5.5: a) Scanning electron microscope image of sample A. b) Reconstructed image using a curvature correction phase retrieval algorithm. c) Reconstructed image using only a plane-wave approximation. d) Knife edge test of the reconstructed image along the red dashed line near the top right corner in b) reveals a resolution of 140 nm is achieved.

The reconstructed images of sample A with and without the curvature correction are shown in Figure 5.5 b) and c), which shows that it is impossible to reconstruct the image using the plane wave approximation and a high resolution image can only be recovered by using the curvature correction algorithm. The cropped

version of the scanning electron microscope image of the sample is also displayed in Figure 5.5 a); so the details of the reconstructed image can be easily compared side by side. Apparently, the edges of the 2 μm spheres are clearly resolved in the reconstructed image, and even the small 400 nm particles can also be identified. A knife edge test is also applied to the image to measure the attained resolution, which reveals a resolution of 140 nm (10% - 90% max intensity) is achieved, as shown in Figure 5.5 d).

The same method is applied to reconstruct the images of samples B and C; however, due to lack of high angle diffraction data, the expected resolution of the recovered images is lower than that of the image of sample A and the objects will appear more blurry. The reconstructed images of these two samples are shown in Figure 5.6 b) and d), where the corresponding scanning electron microscope images are shown in a) and c). As can be seen, the images only reveal the shadows of the cluster of objects rather than the circle-shape of each of the particles due to the lack of high frequency data in the diffraction pattern.

In the reconstructed image of sample B, it is barely possible to identify any silica spheres and amino polystyrene particles in this rough image. The whole cluster of small particles appear as a solid object, making it impossible to resolve the individual edges. The reconstructed image also shows a feature at the top edge of the window, which seems to be a dust particle or a defect in the membrane, and which is hardly seen in the SEM image.

A similar resolution is obtained in the reconstructed image of sample C, where the shape of the 2 μm spheres can be barely recognized and the number of spheres can just be counted. However, the 400 nm particles cannot be resolved and the group of 4 nano-spheres below the big cluster appears as a single object in Figure 5.6 d).

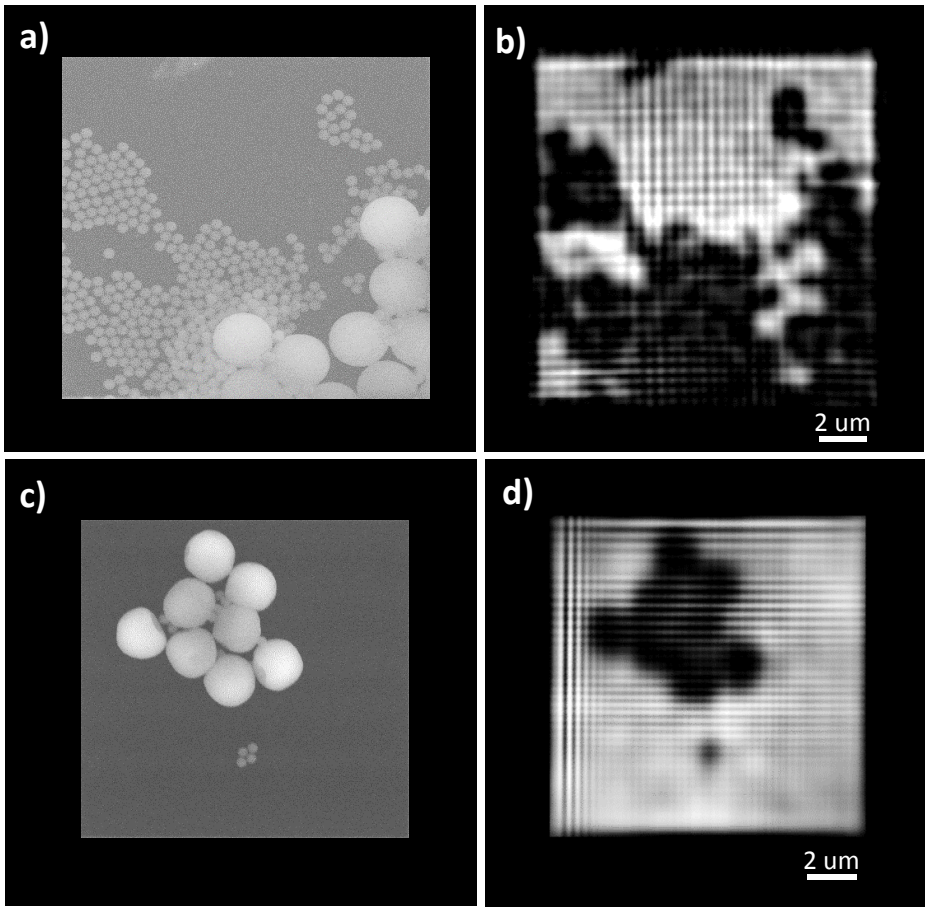

Figure 5.6: a) b) Scanning electron microscope and curvature correction reconstructed images of sample B. c) d) Scanning electron microscope and curvature correction reconstructed images of sample C.

5.5. Enhancing the resolution using a beam stop

5.5.1. Introduction

As discussed in the previous chapters, one fundamental requirement to obtain a high resolution image of the sample is to capture a high dynamic range diffraction pattern which contains sufficient high angle data with a high signal to noise ratio. However, the experimental realization is more complicated than a simulation, since the detector has only a limited dynamic range (~4 orders of magnitude) while a simulated diffraction pattern may have a peak intensity up to 10 orders of magnitude. On the other hand, for a sample with a large transmission area (such as samples B and C), the strong incident beam that propagates through the

sample makes the CCD saturate quickly at the centre peak before capturing any high angle data. Using a beam stop has proven to be an effective solution to this problem, where the high value of the intensities at the centre of the diffraction pattern is removed and this method allows the high angle data to be collected [115][103][102]. However, the beam stop must be small enough so that the missing data is confined within a centro-speckle (inverse of the sample size) of the diffraction pattern, to reliably reconstruct an image of the sample [123]. This requirement may place a limit on the dynamic range of the diffraction pattern if the sample has a low scattering efficiency, i.e., a round-shape rather than a line-shape. Another approach is to combine multiple diffraction patterns at different exposure times, in which the saturated pixels in the longer exposure time diffraction pattern are replaced by the values in the shorter exposure data [25][124]. By using two beam stops in two perpendicular directions, a high dynamic range diffraction pattern can be produced by stitching three diffraction patterns with appropriate scaling factors, which can be used directly for the reconstruction process [30]. However, special care must be taken when combining different diffraction patterns to ensure the stitched regions precisely overlap and the intensity variation between the gaps is as smooth as possible. In this experiment, a beam stop is installed and a new approach in processing diffraction patterns is investigated in an effort to increase the resolution of the reconstructed images of samples B and C.

5.5.2. Installation of the beam stop

Two metal beam stops with diameters 1.5 mm and 3 mm are attached to the micro-screws in the vertical and horizontal direction in the flange immediately in front of the camera, as shown in Figure 5.7. The beam stops are placed at a

distance of 5 mm from the sensor's surface to minimize scattering of photons and reduce the shadow of the beam stop on the sensor. The optimal positions of the beam stops are adjusted by the micro-screws to block the beam exactly at the centre peak, and these beam stops can be retracted to allow an undistorted diffraction pattern to be captured. The beam stop's arms are also considered to minimize the cross section shadows on the CCD; the arm in the smaller beam stop is made of a thin brass sheet and the larger one is made of copper wire.

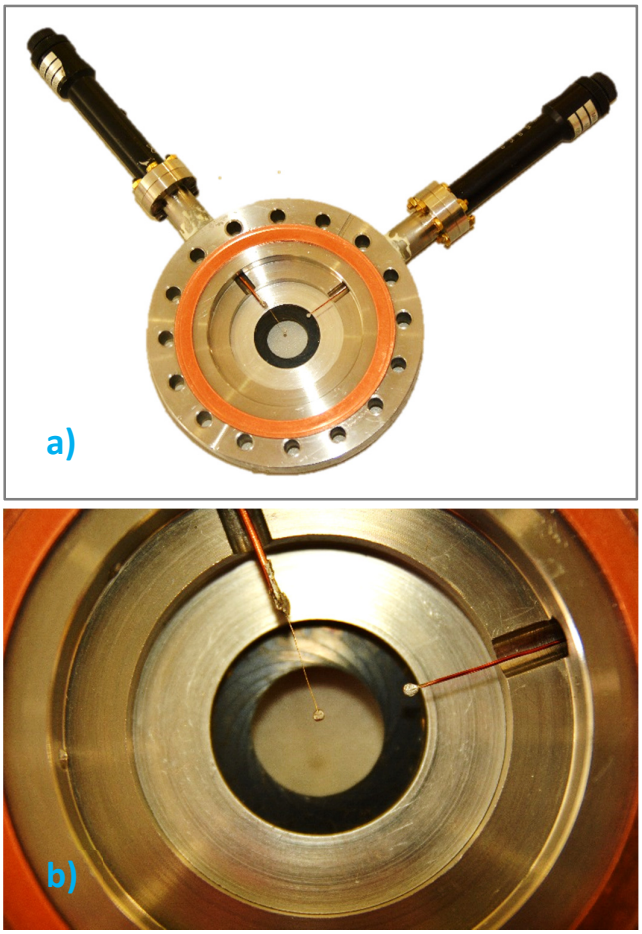

Figure 5.7: a) Two beam stops with diameters 1.5 mm and 3 mm are attached to the micro-crews in the vertical and horizontal directions. b) Close up image of the beam stops, showing the smaller beam stop is extended to the centre while the larger one is retracted.

5.5.3. Enhancement of the dynamic range

For each sample B and C, the diffraction patterns are now taken with a short exposure time without saturation, and with longer exposure time with a saturated region and with a very long exposure time with the beam stop until the highest intensity nearly reaches the maximum value (~65000). The diffraction patterns of these samples without and with a beam stop are shown in Figure 5.8, where a vertical beam stop (1.5 mm diameter) is used.

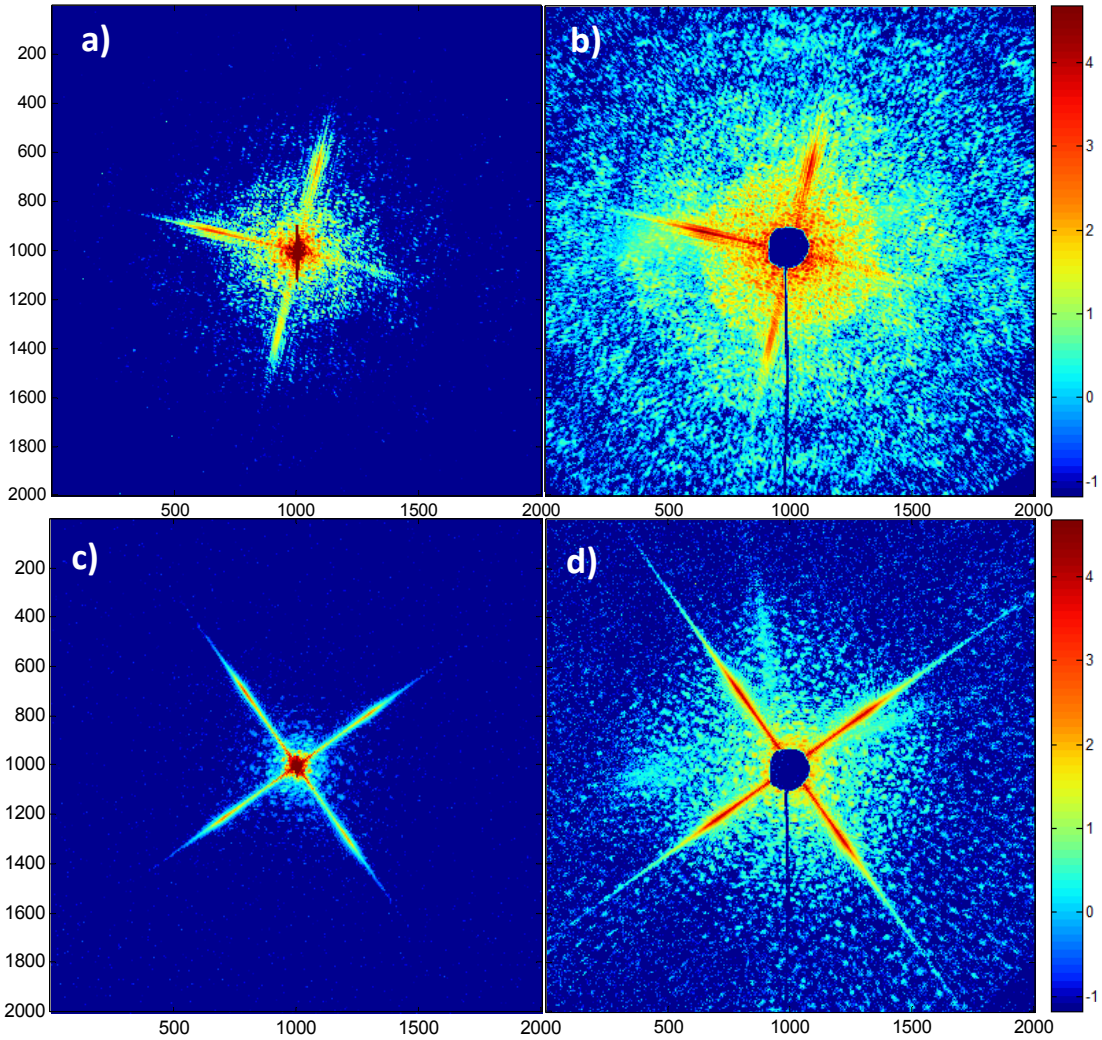

Figure 5.8: Diffraction pattern of sample B without a beam stop for an exposure time of 40 seconds (a) and with a beam stop for an exposure time of 5 minutes (b). Diffraction pattern of sample C without a beam stop for an exposure time of 45 seconds (c) and with a beam stop for an exposure time of 8 minutes (d).

As can be seen, using a longer exposure time, the diffraction patterns have much more detail than the data shown in section 5.3. Saturated regions in the centre of the diffraction pattern can be seen clearly in Figures 5.8 a) and c), where no beam stop is used. With a beam stop and a much longer exposure time, the details are significantly enhanced and the high angle data even exceeds the edge of the detector, as shown in Figure 5.8 b) and d). The increase of the dynamic range can be estimated from the ratio of arbitrary intensity peaks at the same coordinate in the diffraction patterns without and with the beam stop. For example, Figure 5.9 shows a comparison between the intensities of the chosen pattern in the data of sample B with no saturation (a) similar to the data shown in section 5.3 and with a beam stop (b). The ratio between the two chosen peaks is 288, which indicates that if the centre peak of the diffraction pattern a) is replaced by the centre part of the diffraction pattern b), the new peak intensity will become $65000 \times 288 = 1.9 \times 10^7$, so that the dynamic range is extended to seven orders of magnitude.

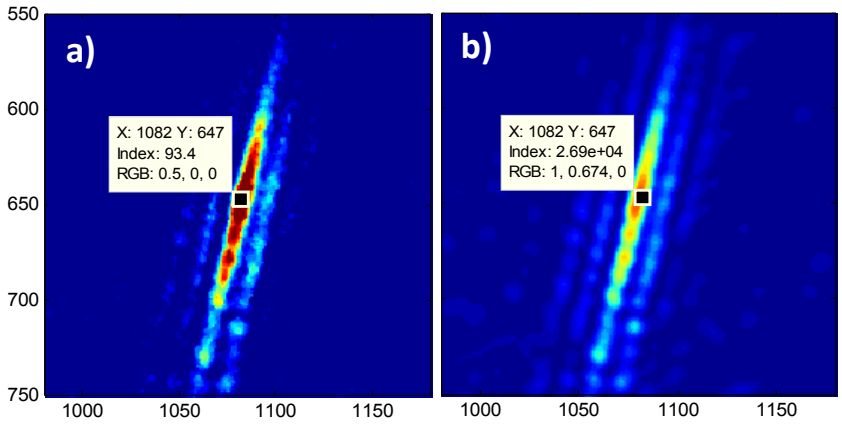

Figure 5.9: a) Cropped diffraction data of sample B with an exposure time of 3 seconds, showing a chosen peak. b) The same peak in the diffraction taken with a beam stop and 5 minutes exposure time indicates an increase of 288 times in the intensity.

The same calculation is applied to the diffraction data of sample C, which is shown in Figure 5.10. The ratio of the two peaks in the diffraction patterns without saturation and with the beam stop is 580 times, which indicates that the highest peak in the combined diffraction pattern will be 3.8×10^7, and the new dynamic range will be seven orders of magnitude.

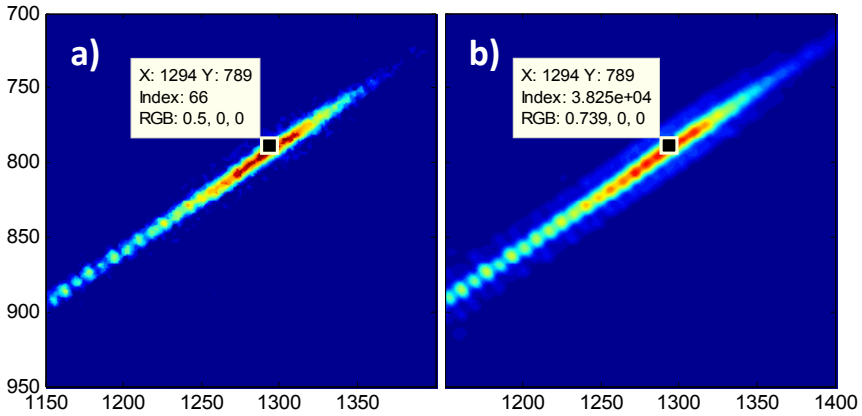

Figure 5.10: a) Cropped diffraction data of sample C with an exposure time of 1.5 seconds, showing a chosen peak. b) The same peak in the diffraction taken with a beam stop and 8 minutes exposure time, indicating an increase of 580 times in the intensity.

5.5.4. Phase retrieval algorithm for multiple diffraction patterns

High dynamic range diffraction patterns taken with a beam stop are very promising to reconstruct high resolution images; however a new challenge is to combine the diffraction patterns together and to modify the phase retrieval algorithm to adapt to the new kind of data. In this modified version of the algorithm, the steps are as follows:

1) A low resolution image of the sample is reconstructed using a diffraction pattern without saturation as described in section 5.4.

2) The centre part of this diffraction pattern is stitched to a diffraction pattern which has a longer exposure time and the centre region is saturated (Figure 5.8 a) and c)). To precisely combine the two sets of data, a masked region is manually selected that contains the saturated pixels. The combined diffraction data is given by:

$$I' = \alpha * I_{low} * \text{mask}_1 + I_{high} * \overline{\text{mask}_1} \qquad (5.1)$$

where I' is the combined diffraction data, I_{low} and I_{high} are the diffraction data with no saturation and with saturation, α is a scaling factor, *mask* is the binary region containing the saturated pixels and $\overline{mask}$ is the inverse of *mask.*

3) The new sample's image is reconstructed by running the phase correction phase retrieval algorithm with the initial guess which is the low resolution image obtained from step 1. The optimal value of the scaling factor α can be obtained by performing scan trials of reconstruction with a range of α until we obtain the best quality image.

4) The diffraction I' is again used to stitch to the beam stop diffraction pattern ($I_{beamstop}$) to produce a complete diffraction pattern I'', for which a new mask_2 for the beam stop is defined and a new scaling factor β is estimated:

$$I'' = \beta * I' * \text{mask}_2 + I_{beamstop} * \overline{\text{mask}_2} \qquad (5.2)$$

5) The final reconstruction is performed using I'' and the image obtained in step 3 is used as an initial guess. The optimal value of β is obtained by repeating the reconstruction process with different values of β until the recovered image is satisfactory.

5.5.5. Improved reconstruction results

The reconstructed images of samples B and C are shown in Figures 5.11 and 5.12, which used the algorithm as described above.

As can be seen in Figure 5.11 b), finer detail can be seen in the reconstructed image of sample B, especially the single 400 nm particles near the left edge can be identified. Since the cluster of the amino polystyrene appears as a solid object, no individual particle can be resolved.

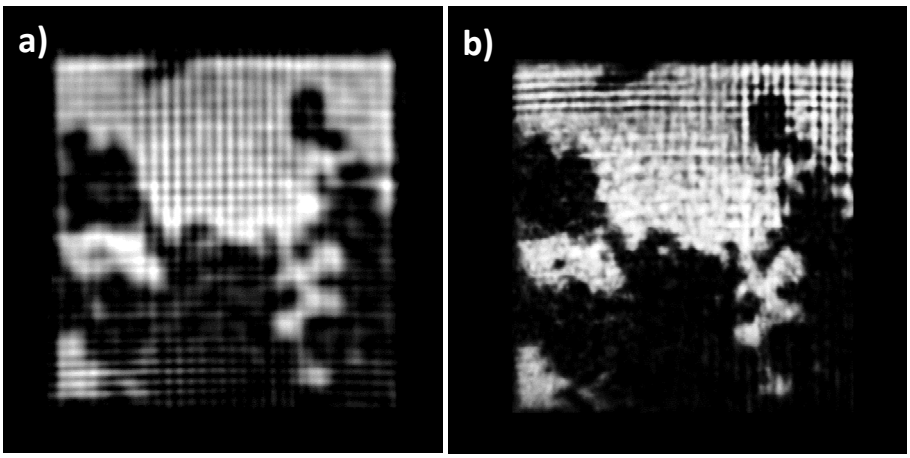

Figure 5.11: a) Low resolution reconstructed image of sample B without saturation and beam stop. b) Higher resolution image obtained by processing the diffraction pattern with the beam stop and saturation region.

In Figure 5.12 b), a higher resolution image is obtained, where the 2 μm spheres are clearly observed and easily identified. However, the 400 nm particles are hardly seen in the gaps between the bigger spheres. A group of four particles at the bottom are much clearer than before, but the individual particles are not distinguishable.

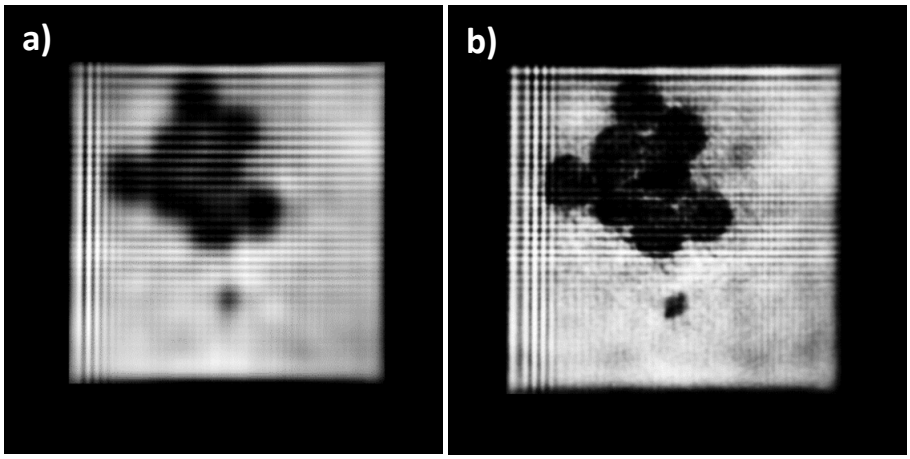

Figure 5.12: a) Low resolution reconstructed image of sample C without saturation and beam stop. b) Higher resolution image obtained by processing the diffraction pattern with the beam stop and saturation region.

5.6. Conclusion

A coherent diffractive imaging experiment with absorption samples has been successfully demonstrated using a high harmonic source with wavelength around 30 nm. Since these samples have similar characteristics to practical biological specimens, the experiment confirms the feasibility of imaging biological samples with a nanometre resolution using an inexpensive table-top high harmonic generation source. Using a beam stop and a new processing algorithm to produce a high dynamic range diffraction pattern, high resolution images can be reconstructed. The experiment also proves the effectiveness of the curvature correction phase retrieval algorithm to reconstruct a high resolution image of a sample which is illuminated by a focused source to utilize the high photon flux near the focus point and reduce the required exposure time.

Chapter 6

Conclusions and future directions

In this dissertation, the theoretical and experimental aspects of high harmonic generation and its applications, including coherent diffractive imaging, were discussed and demonstrated.

As a crucial requirement of coherent diffractive imaging, the generation of a bright, highly coherent, stable and narrow-bandwidth extreme ultraviolet source with wavelengths around 30 nm was reported. By adjusting the experimental parameters in the high harmonic generation in a gas cell, including the gas pressure, the interaction length and the driving laser intensity, the macroscopic phase-matching condition could be optimized to produce a collimated harmonic source with the generated emission confined to a just few harmonic orders. In addition, a high degree of stability and reliability of the experiment was ensured by the development of laser beam pointing and gas cell pressure stabilization systems. With an infrared driving laser, the extension of the cutoff of the harmonic orders and the generation of radiation in the water window region (2.3 – 4.4 nm) was demonstrated, which is highly promising for imaging applications with biological samples. On the other hand, the microscopic aspects of the high harmonic generation process were also examined in order to study the atomic and molecular dynamics. By using two-colour laser fields in the HHG experiment, the visibility of a Cooper minimum in the high harmonic spectrum could be enhanced or minimized, which allows the structure of the atom to be analyzed.

Coherent diffractive imaging, as one of the most important applications of high harmonic generation, was performed with a focused extreme ultraviolet source.

By using XUV band-pass reflective and focusing mirrors, a single harmonic around 30 nm was selected to illuminate micron-size samples; as a result, a higher photon flux and a shorter acquisition time could be achieved and a resolution of 45 nm with a transmission sample was successfully demonstrated. Furthermore, a modified phase retrieval algorithm with phase-curvature correction was presented, which allows a good image of the sample to be still reconstructed if it is placed near the focus point to take advantage of the high photon flux. A CDI experiment was also demonstrated with absorption samples which have similar characteristics to biological specimens. With samples having large transmission areas, a beam stop was introduced to capture high dynamic range diffraction patterns and a new reconstruction algorithm was developed to recover high quality images from multiple diffraction data.

To produce higher resolution images of the samples, reducing the wavelength of the source is one of the possible directions. Using a narrow band-pass source with wavelengths around 13.5 nm generated by helium gas, a low resolution (~200 nm) image of a periodic sample was demonstrated [124]. A problem arises from the low photon flux and the low degree of coherence of the source, which consists of a large number (~10) of harmonic orders after passing the mirrors. By incorporating the contribution of multiple harmonics in the diffraction pattern in the reconstruction process, a so-called "Poly CDI", higher resolution of the images can be achieved. This multiple wavelength reconstruction algorithm is useful for an imaging experiment with a harmonic source with short wavelengths, including the water window region, where selection of individual harmonics is impossible and multiple harmonic orders are required to build up a sufficiently high photon flux. Before performing CDI with water window radiation, the feasibility of multiple wavelength reconstruction can be confirmed by an experiment with a

13.5 nm source with the same set of test samples as used in the experiment with 30 nm.

Better diffraction patterns can produce higher quality reconstructed images, as enhancing the dynamic range and the signal to noise ratio of the diffraction pattern is a crucial step in a CDI experiment. Currently, a high dynamic range diffraction pattern is obtained by stitching multiple diffraction data with and without a beam stop. However, scaling the non-uniform intensity distribution and smoothing different background levels are the main challenge to produce a "clean" diffraction pattern. A suitable algorithm which "blends" diffraction patterns together is desirable to achieve this.

Another aspect to improve the experimental results is to increase the harmonic photon flux, which can be achieved by optimizing the quasi-phase matching process. The enhancement of the high harmonic emission in a dual-gas multi-jet array has been successfully demonstrated [73]. This experimental scheme is also very promising for a bright XUV source for imaging applications. On the other hand, two-colour field HHG experiments have demonstrated the ability of enhancement of a specific region of the harmonic spectrum, which can be useful to optimize the harmonic orders within the bandwidth of the band-pass mirrors.

One of the main drawbacks of coherent diffraction imaging is the post-processing time consumption. However, this can be minimized by implementing a reconstruction process in Graphical Processing Unit to utilize parallel computing technology. A reduction of at least 15 times in the reconstruction time has been reported, which allows the image to be visible in a matter of seconds. By integrating the acquisition process and the reconstruction process in a single program, live coherent diffractive imaging is feasible and will be available in the near future.

References

[1] R. Hooke, *Micrographia: or some physiological descriptions of minute bodies made by magnifying glasses with observations and inquiries thereupon*. Dover Publications, 1665, 246.

[2] E. Francis, *Antony van Leeuwenhoek and his "Little Animals,"* 76. Dover Pubs, 1932, 597–597.

[3] L. Rosenfeld, *Principles of optics. Electromagnetic theory of propagation, interference and diffraction of light*, 7th ed., 15. Cambridge University Press, 1960, 531.

[4] K. I. Willig, S. O. Rizzoli, V. Westphal, R. Jahn, and S. W. Hell, "STED microscopy reveals that synaptotagmin remains clustered after synaptic vesicle exocytosis.," *Nature*, 440, 935–939, 2006.

[5] E. Betzig, G. H. Patterson, R. Sougrat, O. W. Lindwasser, S. Olenych, J. S. Bonifacino, M. W. Davidson, J. Lippincott-Schwartz, and H. F. Hess, "Imaging intracellular fluorescent proteins at nanometer resolution.," *Science*, 313, 1642–1645, 2006.

[6] Nobelprize.org, "Press Release: The 1986 Nobel Prize in Physics," *Nobel Media AB*, 2014. [Online]. Available: http://www.nobelprize.org/nobel_prizes/physics/laureates/1986/press.html.

[7] D. McMullan, "Scanning electron microscopy 1928–1965," *Scanning*, 17, 175–185, 1995.

[8] D. Krinsley, *Advanced Scanning Electron Microscopy and X Ray Microanalysis*, 69. Springer, 1988, 821.

[9] R. Erni, M. D. Rossell, C. Kisielowski, and U. Dahmen, "Atomic-Resolution Imaging with a Sub-50-pm Electron Probe," *Phys. Rev. Lett.*, 102, 096101, 2009.

[10] J. C. H. Spence, *High-resolution Electron Microscopy*. Oxford Univ Pr, 2013.

[11] N. F. Cheville and J. Stasko, "Techniques in electron microscopy of animal tissue.," *Vet. Pathol.*, 51, 28–41, 2014.

[12] A. Sakdinawat and D. Attwood, "Nanoscale X-ray imaging," *Nat. Photonics*, 4, 840–848, 2010.

[13] J. Kirz, C. Jacobsen, and M. Howells, "Soft X-ray microscopes and their biological applications.," *Q. Rev. Biophys.*, 28, 33–130, 1995.

[14] J. Vila-Comamala, K. Jefimovs, J. Raabe, T. Pilvi, R. H. Fink, M. Senoner, A. Maaßdorf, M. Ritala, and C. David, "Advanced thin film technology for ultrahigh resolution X-ray microscopy," *Ultramicroscopy*, 109, 1360–1364, 2009.

[15] "SLAC Linac Coherent Light Source," 2012. [Online]. Available: http://www-ssrl.slac.stanford.edu/lcls/users/schedules.html. [Accessed: 11-Jan-2015].

[16] "SPring-8 operation schedule." [Online]. Available: http://www.spring8.or.jp/en/users/operation_status/schedule/. [Accessed: 11-Jan-2015].

[17] J. Miao, P. Charalambous, J. Kirz, and D. Sayre, "Extending the methodology of X-ray crystallography to allow imaging of micrometre-sized non-crystalline specimens," *Nature*, 400, 342–344, 1999.

[18] G. Williams, H. Quiney, B. Dhal, C. Tran, K. Nugent, A. Peele, D. Paterson, and M. de Jonge, "Fresnel Coherent Diffractive Imaging," *Phys. Rev. Lett.*, 97, 025506, 2006.

[19] a E. Phenomenology, "Lensless imaging of magnetic nanostructures by X-ray," *Nature*, 432, 885–888, 2004.

[20] H. N. Chapman, A. Barty, M. J. Bogan, S. Boutet, M. Frank, S. P. Hau-Riege, S. Marchesini, B. W. Woods, S. Bajt, W. H. Benner, R. A. London, E. Plonjes, M. Kuhlmann, R. Treusch, S. Dusterer, T. Tschentscher, J. R. Schneider, E. Spiller, T. Moller, C. Bostedt, M. Hoener, D. A. Shapiro, K. O. Hodgson, D. van der Spoel, F. Burmeister, M. Bergh, C. Caleman, G. Huldt, M. M. Seibert, F. R. N. C. Maia, R. W. Lee, A. Szoke, N. Timneanu, and J. Hajdu, "Femtosecond Diffractive Imaging with a Soft-X-ray Free-Electron Laser," *Nat. Phys.*, 2, 6, 2006.

[21] B. Abbey, K. A. Nugent, G. J. Williams, J. N. Clark, A. G. Peele, M. A. Pfeifer, M. de Jonge, and I. McNulty, "Keyhole coherent diffractive imaging," *Nat. Phys.*, 4, 394–398, 2008.

[22] J. R. Fienup, "Phase retrieval algorithms: a comparison.," *Appl. Opt.*, 21, 2758–2769, 1982.

[23] J. Miao, D. Sayre, and H. N. Chapman, "Phase retrieval from the magnitude of the Fourier transforms of nonperiodic objects," *J. Opt. Soc. Am. A*, 15, 1662, 1998.

[24] L. W. Whitehead, G. J. Williams, H. M. Quiney, K. A. Nugent, A. G. Peele, D. Paterson, M. D. De Jonge, and I. McNulty, "Fresnel diffractive imaging: Experimental study of coherence and curvature," *Phys. Rev. B - Condens. Matter Mater. Phys.*, 77, 104112, 2008.

[25] B. Chen, R. A. Dilanian, S. Teichmann, B. Abbey, A. G. Peele, G. J. Williams, P. Hannaford, L. Van Dao, H. M. Quiney, and K. A. Nugent, "Multiple wavelength diffractive imaging," *Phys. Rev. A - At. Mol. Opt. Phys.*, 79, 023809, 2009.

[26] B. Abbey, L. W. Whitehead, H. M. Quiney, D. J. Vine, G. A. Cadenazzi, C. A. Henderson, K. A. Nugent, E. Balaur, C. T. Putkunz, A. G. Peele, G. J. Williams, and I. McNulty, "Lensless imaging using broadband X-ray sources," *Nat. Photonics*, 5, 420–424, 2011.

[27] A. McPherson, G. Gibson, H. Jara, U. Johann, T. S. Luk, I. A. McIntyre, K. Boyer, and C. K. Rhodes, "Studies of multiphoton production of vacuum-ultraviolet radiation in the rare gases," *J. Opt. Soc. Am. B*, 4, 595, 1987.

[28] T. Popmintchev, M.-C. Chen, D. Popmintchev, P. Arpin, S. Brown, S. Alisauskas, G. Andriukaitis, T. Balciunas, O. D. Mucke, A. Pugzlys, A. Baltuska, B. Shim, S. E. Schrauth, A. Gaeta, C. Hernandez-Garcia, L. Plaja, A. Becker, A. Jaron-Becker, M. M. Murnane, and H. C. Kapteyn, "Bright Coherent Ultrahigh Harmonics in the keV X-ray Regime from Mid-Infrared Femtosecond Lasers," *Science*, 336, 1287–1291, 2012.

[29] L. Van Dao, S. Teichmann, and P. Hannaford, "Phase-matching for generation of few high order harmonics in a semi-infinite gas cell," *Phys. Lett. Sect. A Gen. At. Solid State Phys.*, 372, 5254–5257, 2008.

[30] S. Teichmann, B. Chen, R. A. Dilanian, P. Hannaford, and L. Van Dao, "Experimental aspects of multiharmonic-order coherent diffractive imaging," *J. Appl. Phys.*, 108, 023106, 2010.

[31] T. Brabec and F. Krausz, "Intense few-cycle laser fields: Frontiers of nonlinear optics," *Rev. Mod. Phys.*, 72, 545–591, 2000.

[32] Z. Chang, A. Rundquist, H. Wang, M. Murnane, and H. Kapteyn, "Generation of Coherent Soft X Rays at 2.7 nm Using High Harmonics," *Phys. Rev. Lett.*, 79, 2967–2970, 1997.

[33] C. Spielmann, "Generation of Coherent X-rays in the Water Window Using 5-Femtosecond Laser Pulses," *Science*, 278, 661–664, 1997.

[34] J. Seres, E. Seres, A. J. Verhoef, G. Tempea, C. Streli, P. Wobrauschek, V. Yakovlev, A. Scrinzi, C. Spielmann, and F. Krausz, "Laser technology: source of coherent kiloelectronvolt X-rays.," *Nature*, 433, 596, 2005.

[35] L. Nugent-Glandorf, M. Scheer, D. A. Samuels, A. M. Mulhisen, E. R. Grant, X. Yang, V. M. Bierbaum, and S. R. Leone, "Ultrafast time-resolved soft x-ray photoelectron spectroscopy of dissociating Br2.," *Phys. Rev. Lett.*, 87, 193002, 2001.

[36] M. Schultze, M. Ulberacker, T. Uphues, A. J. Verhoef, V. Yakovlev, M. F. Kling, J. Rausehenberger, N. M. Kabachnik, H. Schröder, M. Lezius, K. L. Kompa, H. G. Muller, M. J. J. Vrakkinig, S. Hendel, U. Kleineberg, U. Heinzmann, M. Drescher, and F. Krausz, "Attosecond real-time observation of electron tunnelling and multi-electron dynamics in atoms," *Conf. Lasers Electro-Optics Eur. - Tech. Dig.*, 446, 627–32, 2007.

[37] A. L. Cavalieri, N. Müller, T. Uphues, V. S. Yakovlev, A. Baltuska, B. Horvath, B. Schmidt, L. Blümel, R. Holzwarth, S. Hendel, M. Drescher, U. Kleineberg, P. M. Echenique, R. Kienberger, F. Krausz, and U. Heinzmann, "Attosecond spectroscopy in condensed matter.," *Nature*, 449, 1029–1032, 2007.

[38] E. Gagnon, P. Ranitovic, X.-M. Tong, C. L. Cocke, M. M. Murnane, H. C. Kapteyn, and A. S. Sandhu, "Soft X-ray-driven femtosecond molecular dynamics.," *Science*, 317, 1374–1378, 2007.

[39] A. Ravasio, D. Gauthier, F. R. N. C. Maia, M. Billon, J. P. Caumes, D. Garzella, M. Géléoc, O. Gobert, J. F. Hergott, A. M. Pena, H. Perez, B.

Carré, E. Bourhis, J. Gierak, A. Madouri, D. Mailly, B. Schiedt, M. Fajardo, J. Gautier, P. Zeitoun, P. H. Bucksbaum, J. Hajdu, and H. Merdji, "Single-shot diffractive imaging with a table-top femtosecond soft X-ray laser-harmonics source," *Phys. Rev. Lett.*, 103, 028104, 2009.

[40] M. D. Seaberg, D. E. Adams, E. L. Townsend, D. A. Raymondson, W. F. Schlotter, Y. Liu, C. S. Menoni, L. Rong, C.-C. Chen, J. Miao, H. C. Kapteyn, and M. M. Murnane, "Ultrahigh 22 nm resolution coherent diffractive imaging using a desktop 13 nm high harmonic source," *Opt. Express*, 19, 22470, 2011.

[41] A. Rundquist, "Phase-Matched Generation of Coherent Soft X-rays," *Science*, 280, 1412–1415, 1998.

[42] E. Constant, D. Garzella, P. Breger, E. Mével, C. Dorrer, C. Le Blanc, F. Salin, and P. Agostini, "Optimizing High Harmonic Generation in Absorbing Gases: Model and Experiment," *Phys. Rev. Lett.*, 82, 1668–1671, 1999.

[43] P. Salières, A. L'Huillier, and M. Lewenstein, "Coherence Control of High Order Harmonics," *Phys. Rev. Lett.*, 74, 3776–3779, 1995.

[44] H. Lange, A. Chiron, J.-F. Ripoche, A. Mysyrowicz, P. Breger, and P. Agostini, "High-Order Harmonic Generation and Quasiphase Matching in Xenon Using Self-Guided Femtosecond Pulses," *Phys. Rev. Lett.*, 81, 1611–1613, 1998.

[45] A. L'Huillier and P. Balcou, "High-order harmonic generation in rare gases with a 1-ps 1053-nm laser," *Phys. Rev. Lett.*, 70, 774–777, 1993.

[46] S. Kazamias, D. Douillet, F. Weihe, C. Valentin, A. Rousse, S. Sebban, G. Grillon, F. Augé, D. Hulin, and P. Balcou, "Global optimization of high harmonic generation.," *Phys. Rev. Lett.*, 90, 193901, 2003.

[47] P. B. Corkum, "Plasma Perspective on Strong-Field Multiphoton Ionization," *Phys. Rev. Lett.*, 71, 1994–1997, 1993.

[48] M. Lewenstein, P. Balcou, M. Y. Ivanov, A. L'Huillier, and P. B. Corkum, "Theory of high-harmonic generation by low-frequency laser fields," *Phys. Rev. A*, 49, 2117–2132, 1994.

[49] M. V. Ammosov, N. B. Delone, and V. P. Krainov, "Tunnel ionization of complex atoms and of atomic ions in an alternating electromagnetic field," *Sov. Phys. JETP*, 64, 1191–1194, 1986.

[50] J. Krause, K. Schafer, and K. Kulander, "High-order harmonic generation from atoms and ions in the high intensity regime," *Phys. Rev. Lett.*, 68, 3535–3538, 1992.

[51] C. H. Keitel and P. L. Knight, "Monte Carlo classical simulations of ionization and harmonic generation in the relativistic domain," *Phys. Rev. A*, 51, 1420–1430, 1995.

[52] A. Di Piazza, C. Müller, K. Z. Hatsagortsyan, and C. H. Keitel, "Extremely high-intensity laser interactions with fundamental quantum systems," *Rev. Mod. Phys.*, 84, 1177–1228, 2012.

[53] M. Gaarde, F. Salin, E. Constant, P. Balcou, K. Schafer, K. Kulander, and A. L'Huillier, "Spatiotemporal separation of high harmonic radiation into two quantum path components," *Phys. Rev. A*, 59, 1367–1373, 1999.

[54] M. Bellini, C. Lynga, A. Tozzi, M. B. Gaarde, T. W. Hansch, A. L. Huillier, and C.-G. Wahlstrom, "Temporal Coherence of Ultrashort High-Order Harmonic Pulses," *CLEO/Europe Conf. Lasers Electro-Optics*, 81, 297–300, 1998.

[55] S. Hu, D. Milošević, W. Becker, and W. Sandner, "High-efficiency high-order harmonic generation without tunneling," *Phys. Rev. A*, 64, 013410, 2001.

[56] P. Antoine, A. L'Huillier, and M. Lewenstein, "Attosecond Pulse Trains Using High–Order Harmonics," *Phys. Rev. Lett.*, 77, 1234–1237, 1996.

[57] C. Gohle, "A Coherent Frequency Comb in the Extreme Ultraviolet," 2006.

[58] A. Rundquist, "Phase-Matched Generation of Coherent Soft X-rays," *Science*, 280, 1412–1415, 1998.

[59] T. Popmintchev, M.-C. Chen, P. Arpin, M. M. Murnane, and H. C. Kapteyn, "The attosecond nonlinear optics of bright coherent X-ray generation," *Nat. Photonics*, 4, 822–832, 2010.

[60] C. Durfee, A. Rundquist, S. Backus, C. Herne, M. Murnane, and H. Kapteyn, "Phase Matching of High-Order Harmonics in Hollow Waveguides," *Phys. Rev. Lett.*, 83, 2187–2190, 1999.

[61] A. Paul, E. A. Gibson, X. Zhang, A. Lytle, T. Popmintchev, X. Zhou, M. M. Murnane, I. P. Christov, and H. C. Kapteyn, "Phase-matching techniques for coherent soft X-ray generation," *IEEE J. Quantum Electron.*, 42, 14–26, 2006.

[62] A. E. Siegman, *Lasers*. University Science Books, 1986, 1283.

[63] J. Peatross and D. D. Meyerhofer, "Intensity-dependent atomic-phase effects in high-order harmonic generation," *Phys. Rev. A*, 52, 3976–3987, 1995.

[64] T. Auguste, B. Carré, and P. Salières, "Quasi-phase-matching of high-order harmonics using a modulated atomic density," *Phys. Rev. A - At. Mol. Opt. Phys.*, 76, 011802, 2007.

[65] C. Lyngå, M. Gaarde, C. Delfin, M. Bellini, T. Hänsch, A. L' Huillier, and C.-G. Wahlström, "Temporal coherence of high-order harmonics," *Phys. Rev. A*, 60, 4823–4830, 1999.

[66] T. Popmintchev, M. M.-C. Chen, O. Cohen, M. E. Grisham, J. J. Rocca, M. M. Murnane, and H. C. Kapteyn, "Extended phase matching of high harmonics driven by mid-infrared light," *Opt. Lett.*, 33, 2128–2130, 2008.

[67] G. Doumy, J. Wheeler, C. Roedig, R. Chirla, P. Agostini, and L. F. Dimauro, "Attosecond synchronization of high-order harmonics from midinfrared drivers," *Phys. Rev. Lett.*, 102, 093002, 2009.

[68] M. C. Chen, P. Arpin, T. Popmintchev, M. Gerrity, B. Zhang, M. Seaberg, D. Popmintchev, M. M. Murnane, and H. C. Kapteyn, "Bright, coherent, ultrafast soft x-ray harmonics spanning the water window from a tabletop light source," *Phys. Rev. Lett.*, 105, 2–3, 2010.

[69] O. Cohen, X. Zhang, A. Lytle, T. P. H. C. Kapteyn, and M. M. Murnane, "Grating-assisted phase matching in extreme nonlinear optics," *Conf. Lasers Electro-Optics, 2007, CLEO 2007*, 99, 1–4, 2007.

[70] C. Serrat and J. Biegert, "All-regions tunable high harmonic enhancement by a periodic static electric field," *Phys. Rev. Lett.*, 104, 1–4, 2010.

[71] A. Paul, R. A. Bartels, R. Tobey, H. Green, S. Weiman, I. P. Christov, M. M. Murnane, H. C. Kapteyn, and S. Backus, "Quasi-phase-matched generation of coherent extreme-ultraviolet light.," *Nature*, 421, 51–54, 2003.

[72] A. Willner, F. Tavella, M. Yeung, T. Dzelzainis, C. Kamperidis, M. Bakarezos, D. Adams, M. Schulz, R. Riedel, M. C. Hoffmann, W. Hu, J. Rossbach, M. Drescher, N. A. Papadogiannis, M. Tatarakis, B. Dromey, and M. Zepf, "Coherent control of high harmonic generation via dual-gas multijet arrays," *Phys. Rev. Lett.*, 107, 1–5, 2011.

[73] M. G. Pullen, N. S. Gaffney, C. R. Hall, J. A. Davis, A. Dubrouil, H. V Le, R. Buividas, D. Day, H. M. Quiney, and L. V Dao, "High-order harmonic generation from a dual-gas, multi-jet array with individual gas jet control.," *Opt. Lett.*, 38, 4204–7, 2013.

[74] E. A. Gibson, A. Paul, N. Wagner, R. Tobey, D. Gaudiosi, S. Backus, I. P. Christov, A. Aquila, E. M. Gullikson, D. T. Attwood, M. M. Murnane, and H. C. Kapteyn, "Coherent soft x-ray generation in the water window with quasi-phase matching.," *Science*, 302, 95–98, 2003.

[75] "VENTEON Femtosecond Laser Technologies - PULSE : ONE." [Online]. Available: http://www.venteon.com/one_CP.php.

[76] D. J. Jones, "Carrier-Envelope Phase Control of Femtosecond Mode-Locked Lasers and Direct Optical Frequency Synthesis," *Science*, 288, 635–639, 2000.

[77] D. Strickland and G. Mourou, "Compression of amplified chirped optical pulses," *Opt. Commun.*, 55, 447–449, 1985.

[78] H. Hellwig, J. Liebertz, and L. Bohatý, "Exceptional large nonlinear optical coefficients in the monoclinic bismuth borate BiB3O6 (BIBO)," *Solid State Commun.*, 109, 249–251, 1998.

[79] "Filter Transmission 1," 2009. [Online]. Available: http://henke.lbl.gov/optical_constants/filter2.html.

[80] F. Breitling, R. S. Weigel, M. C. Downer, and T. Tajima, "Laser pointing stabilization and control in the submicroradian regime with neural networks," *Rev. Sci. Instrum.*, 72, 1339–1342, 2001.

[81] T. Kanai, A. Suda, S. Bohman, M. Kaku, S. Yamaguchi, and K. Midorikawa, "Pointing stabilization of a high-repetition-rate high-power femtosecond laser for intense few-cycle pulse generation," *Appl. Phys. Lett.*, 92, 061106, 2008.

[82] L. Kral, "Automatic beam alignment system for a pulsed infrared laser," *Rev. Sci. Instrum.*, 80, 013102, 2009.

[83] "Laser Beam Position Sensing Detector." [Online]. Available: http://www.newport.com/Laser-Beam-Position-Sensing-Detector/319793/1033/info.aspx.

[84] A. Stalmashonak, N. Zhavoronkov, I. V. Hertel, S. Vetrov, and K. Schmid, "Spatial control of femtosecond laser system output with submicroradian accuracy.," *Appl. Opt.*, 45, 1271–1274, 2006.

[85] "NI LabVIEW Vision Development Module - National Instruments." [Online]. Available: http://www.ni.com/labview/vision/.

[86] R. Singh, K. Patel, J. Govindarajan, and A. Kumar, "Fuzzy logic based feedback control system for laser beam pointing stabilization," *Appl. Opt.*, 49, 5143–7, 2010.

[87] M. Schnürer, Z. Cheng, M. Hentschel, G. Tempea, P. Kálmán, T. Brabec, and F. Krausz, "Absorption-Limited Generation of Coherent Ultrashort Soft-X-Ray Pulses," *Phys. Rev. Lett.*, 83, 722–725, 1999.

[88] C. Altucci, T. Starczewski, E. Mevel, C.-G. Wahlström, B. Carré, and A. L'Huillier, "Influence of atomic density in high-order harmonic generation," *J. Opt. Soc. Am. B*, 13, 148, 1996.

[89] H. Dachraoui, T. Auguste, A. Helmstedt, P. Bartz, M. Michelswirth, N. Mueller, W. Pfeiffer, P. Salieres, and U. Heinzmann, "Interplay between absorption, dispersion and refraction in high-order harmonic generation," *J. Phys. B At. Mol. Opt. Phys.*, 42, 175402, 2009.

[90] S. Meyer and B. Chichkov, "Phase-matched high-order harmonic generation and parametric amplification," *Phys. Rev. A*, 61, 1–15, 2000.

[91] J. A. R. Samson and W. C. Stolte, "Precision measurements of the total photoionization cross-sections of He, Ne, Ar, Kr, and Xe," *J. Electron Spectros. Relat. Phenomena*, 123, 265–276, 2002.

[92] P. Colosimo, G. Doumy, C. I. Blaga, J. Wheeler, C. Hauri, F. Catoire, J. Tate, R. Chirla, A. M. March, G. G. Paulus, H. G. Muller, P. Agostini, and L. F. DiMauro, "Scaling strong-field interactions towards the classical limit," *Nat. Phys.*, 4, 386–389, 2008.

[93] T. Popmintchev, M. Chen, and O. Cohen, "Extended phase matching of high harmonics driven by mid-infrared light," *Opt. Lett.*, 33, 2128–2130, 2008.

[94] O. Smirnova, Y. Mairesse, S. Patchkovskii, N. Dudovich, D. Villeneuve, P. Corkum, and M. Y. Ivanov, "High harmonic interferometry of multi-electron dynamics in molecules.," *Nature*, 460, 972–7, 2009.

[95] H. J. Wörner, J. B. Bertrand, D. V Kartashov, P. B. Corkum, and D. M. Villeneuve, "Following a chemical reaction using high-harmonic interferometry.," *Nature*, 466, 604–7, 2010.

[96] J. W. Cooper, "Photoionization from outer atomic subshells. A model study," *Phys. Rev.*, 128, 681–693, 1962.

[97] H. Wörner, H. Niikura, J. Bertrand, P. Corkum, and D. Villeneuve, "Observation of Electronic Structure Minima in High-Harmonic Generation," *Phys. Rev. Lett.*, 102, 103901, 2009.

[98] J. Higuet, H. Ruf, N. Thiré, R. Cireasa, E. Constant, E. Cormier, D. Descamps, E. Mével, S. Petit, B. Pons, Y. Mairesse, and B. Fabre, "High-order harmonic spectroscopy of the Cooper minimum in argon: Experimental and theoretical study," *Phys. Rev. A - At. Mol. Opt. Phys.*, 83, 053401, 2011.

[99] A. D. Shiner, B. E. Schmidt, C. Trallero-Herrero, P. B. Corkum, J.-C. Kieffer, F. Légaré, and D. M. Villeneuve, "Observation of Cooper minimum in krypton using high harmonic spectroscopy," *J. Phys. B At. Mol. Opt. Phys.*, 45, 074010, 2012.

[100] J. P. Farrell, L. S. Spector, B. K. McFarland, P. H. Bucksbaum, M. Gühr, M. B. Gaarde, and K. J. Schafer, "Influence of phase matching on the Cooper minimum in Ar high-order harmonic spectra," *Phys. Rev. A - At. Mol. Opt. Phys.*, 83, 023420, 2011.

[101] P. Thibault, M. Dierolf, A. Menzel, O. Bunk, C. David, and F. Pfeiffer, "High-resolution scanning x-ray diffraction microscopy.," *Science*, 321, 379–382, 2008.

[102] T. Kimura, Y. Joti, A. Shibuya, C. Song, S. Kim, K. Tono, M. Yabashi, M. Tamakoshi, T. Moriya, T. Oshima, T. Ishikawa, Y. Bessho, and Y. Nishino, "Imaging live cell in micro-liquid enclosure by X-ray laser diffraction.," *Nat. Commun.*, 5, 3052, 2014.

[103] R. Xu, H. Jiang, C. Song, J. A. Rodriguez, Z. Huang, C.-C. Chen, D. Nam, J. Park, M. Gallagher-Jones, S. S. Kim, A. Suzuki, Y. Takayama, T. Oroguchi, Y. Takahashi, J. Fan, Y. Zou, T. Hatsui, Y. Inubushi, T. Kameshima, K. Yonekura, K. Tono, T. Togashi, T. Sato, M. Yamamoto, M. Nakasako, M. Yabashi, T. Ishikawa, and J. Miao, "Single-shot three-dimensional structure determination of nanocrystals with femtosecond X-ray free-electron laser pulses.," *Nat. Commun.*, 5, 4061, 2014.

[104] R. L. Sandberg, C. Song, P. W. Wachulak, D. A. Raymondson, A. Paul, B. Amirbekian, E. Lee, A. E. Sakdinawat, C. La-O-Vorakiat, M. C. Marconi, C. S. Menoni, M. M. Murnane, J. J. Rocca, H. C. Kapteyn, and J. Miao, "High numerical aperture tabletop soft x-ray diffraction microscopy with 70-nm resolution.," *Proc. Natl. Acad. Sci. U. S. A.*, 105, 24–27, 2008.

[105] K. S. Raines, S. Salha, R. L. Sandberg, H. Jiang, J. A. Rodríguez, B. P. Fahimian, H. C. Kapteyn, J. Du, and J. Miao, "Three-dimensional structure determination from a single view.," *Nature*, 463, 214–217, 2010.

[106] H. C. Kang, H. T. Kim, S. S. Kim, C. Kim, T. J. Yu, S. K. Lee, C. M. Kim, I. J. Kim, J. H. Sung, K. A. Janulewicz, J. Lee, and D. Y. Noh, "Single-pulse coherent diffraction imaging using soft x-ray laser," *Opt. Lett.*, 37, 1688, 2012.

[107] J. Kirz, C. Jacobsen, and M. Howells, "Soft X-ray microscopes and their biological applications," *Q. Rev. Biophys.*, 1995.

[108] F. M. Grimaldi, *Physico-mathesis de lvmine, coloribvs, et iride, aliisque adnexis libri duo: opvs posthvmvm.* Kessinger Publishing, 1665, 570.

[109] C. Huygens, *Treatise on light : in which are explained the causes of that which occurs in reflection, & in refraction and particularly in the strange*

refraction of Iceland crystal. Chicago Ill.: University of Chicago Press, 1945.

[110] H. Crew, C. Huygens, T. Young, A. J. Fresnel, and F. Arago, *The Wave Theory of Light: Memoirs of Huygens, Young and Fresnel*. American Book Company, 1900, 164.

[111] J. W. P. Peatross, *Physics of Light and Optics*. optics.byu.edu, 2008, 1–341.

[112] D. Sayre, "Some implications of a theorem due to Shannon," *Acta Crystallogr.*, 5, 843–843, 1952.

[113] R. W. Gerchberg and W. O. Saxton, "A practical algorithm for the determination of phase from image and diffraction plane pictures," *Optik (Stuttg).*, 35, 237–246, 1972.

[114] J. R. Fienup, "Reconstruction of an object from the modulus of its Fourier transform.," *Opt. Lett.*, 3, 27–29, 1978.

[115] S. Marchesini, H. He, H. N. Chapman, S. P. Hau-Riege, A. Noy, M. R. Howells, U. Weierstall, and J. C. H. Spence, "X-ray image reconstruction from a diffraction pattern alone," *Phys. Rev. B*, 11, 5, 2003.

[116] J. Miao, T. Ishikawa, E. Anderson, and K. Hodgson, "Phase retrieval of diffraction patterns from noncrystalline samples using the oversampling method," *Phys. Rev. B*, 67, 174104, 2003.

[117] H. N. Chapman, A. Barty, S. Marchesini, A. Noy, S. P. Hau-Riege, C. Cui, M. R. Howells, R. Rosen, H. He, J. C. H. Spence, U. Weierstall, T. Beetz, C. Jacobsen, and D. Shapiro, "High-resolution ab initio three-dimensional x-ray diffraction microscopy.," *J. Opt. Soc. Am. A. Opt. Image Sci. Vis.*, 23, 1179–1200, 2006.

[118] X. Ge, W. Boutu, D. Gauthier, F. Wang, A. Borta, B. Barbrel, M. Ducousso, A. I. Gonzalez, B. Carré, D. Guillaumet, M. Perdrix, O. Gobert, J. Gautier, G. Lambert, F. R. N. C. Maia, J. Hajdu, P. Zeitoun, and H. Merdji, "Impact of wave front and coherence optimization in coherent diffractive imaging.," *Opt. Express*, 21, 11441–7, 2013.

[119] H. M. Quiney, "Coherent diffractive imaging using short wavelength light sources," *J. Mod. Opt.*, 57, 1109–1149, 2010.

[120] H. M. Quiney, K. A. Nugent, and A. G. Peele, "Iterative image reconstruction algorithms using wave-front intensity and phase variation.," *Opt. Lett.*, 30, 1638–1640, 2005.

[121] M. Zürch, C. Kern, and C. Spielmann, "XUV coherent diffraction imaging in reflection geometry with low numerical aperture," *Opt. Express*, 21, 21131–21147, 2013.

[122] "Supercomputer Workstations with Tesla K40 and K20 GPUs | NVIDIA." [Online]. Available: http://www.nvidia.com/object/tesla-workstations.html. [Accessed: 15-Jan-2015].

[123] J. Miao, Y. Nishino, Y. Kohmura, B. Johnson, C. Song, S. H. Risbud, and T. Ishikawa, "Quantitative image reconstruction of GaN quantum dots from oversampled diffraction intensities alone," *Phys. Rev. Lett.*, 95, 085503, 2005.

[124] K. Ba Dinh, H. Vu Le, P. Hannaford, and L. Van Dao, "Coherent diffractive imaging with table top high harmonic radiation at 13.5 nm," *J. Mod. Opt.*, 60, 1–7, 2013.

[125] T. Campbell, R. Kalia, A. Nakano, P. Vashishta, S. Ogata, and S. Rodgers, "Dynamics of Oxidation of Aluminum Nanoclusters using Variable Charge Molecular-Dynamics Simulations on Parallel Computers," *Phys. Rev. Lett.*, 82, 4866–4869, 1999.

[126] S. Teichmann, "High Harmonic Generation for Coherent Diffractive Imaging," 2009.

Publications

[1] L. Van Dao, K. B. Dinh, H. V. Le, N. Gaffney and P. Hannaford, "Wave-mixing with high-order harmonics in extreme ultraviolet region," *Appl. Phys. Lett.*, 106, 021118, 2015.

[2] H. Vu Le, K. Ba Dinh, P. Hannaford, and L. Van Dao, "High resolution coherent diffractive imaging with a table-top extreme ultraviolet source," *J. Appl. Phys.*, 116, 173104, 2014.

[3] K. Ba Dinh, H. Vu Le, P. Hannaford, and L. Van Dao, "Two color laser fields for studying the Cooper minimum with phase-matched high-order harmonic generation," *J. Appl. Phys.*, 115, 203103, 2014.

[4] K. Ba Dinh, H. Vu Le, P. Hannaford, and L. Van Dao, "Coherent diffractive imaging with table top high harmonic radiation at 13.5 nm," *J. Mod. Opt.*, 60, 1–7, 2013.

[5] L. V. Dao, C. Hall, H. V. Le, K. B. Dinh, E. Balaur, P. Hannaford, and T. A. Smith, "Phase-matched generation of highly coherent radiation in water window region," *Appl. Opt.*, 51, 4240, 2012.

Conference papers

[1] H. V. Le, K. B. Dinh, P. Hannaford, and L. Van Dao, "Table-Top Coherent Diffractive Imaging Using Extreme Ultraviolet Source," *Computational Optical Sensing and Imaging (COSI) Conference*, Kohala Coast, Hawaii United States, June 2014.

[2] H. V. Le, K. B. Dinh, P. Hannaford, and L. Van Dao, "Coherent Diffractive Imaging with Table-Top High Harmonic Generation," *Australia and New Zealand Conference on Optics and Photonics (ANZCOP),* Fremantle, Western Australia, December 2013.

[3] H. V. Le, C. Hall, K. B. Dinh, P. Hannaford, and L. Van Dao, "Coherent Continuum High Harmonic Generation by Two Colour Laser Fields," *Conference on Optics, Atoms and Laser Applications (KOALA),* Brisbane, Queensland, December 2012.